Mathematical Problems in Engineering

Potential Problems in Emerging Applications of Sparse Arrays 2021

Special Issue Editor in Chief: Xiaofei Zhang
Guest Editors: Wang Zheng and Junpeng Shi

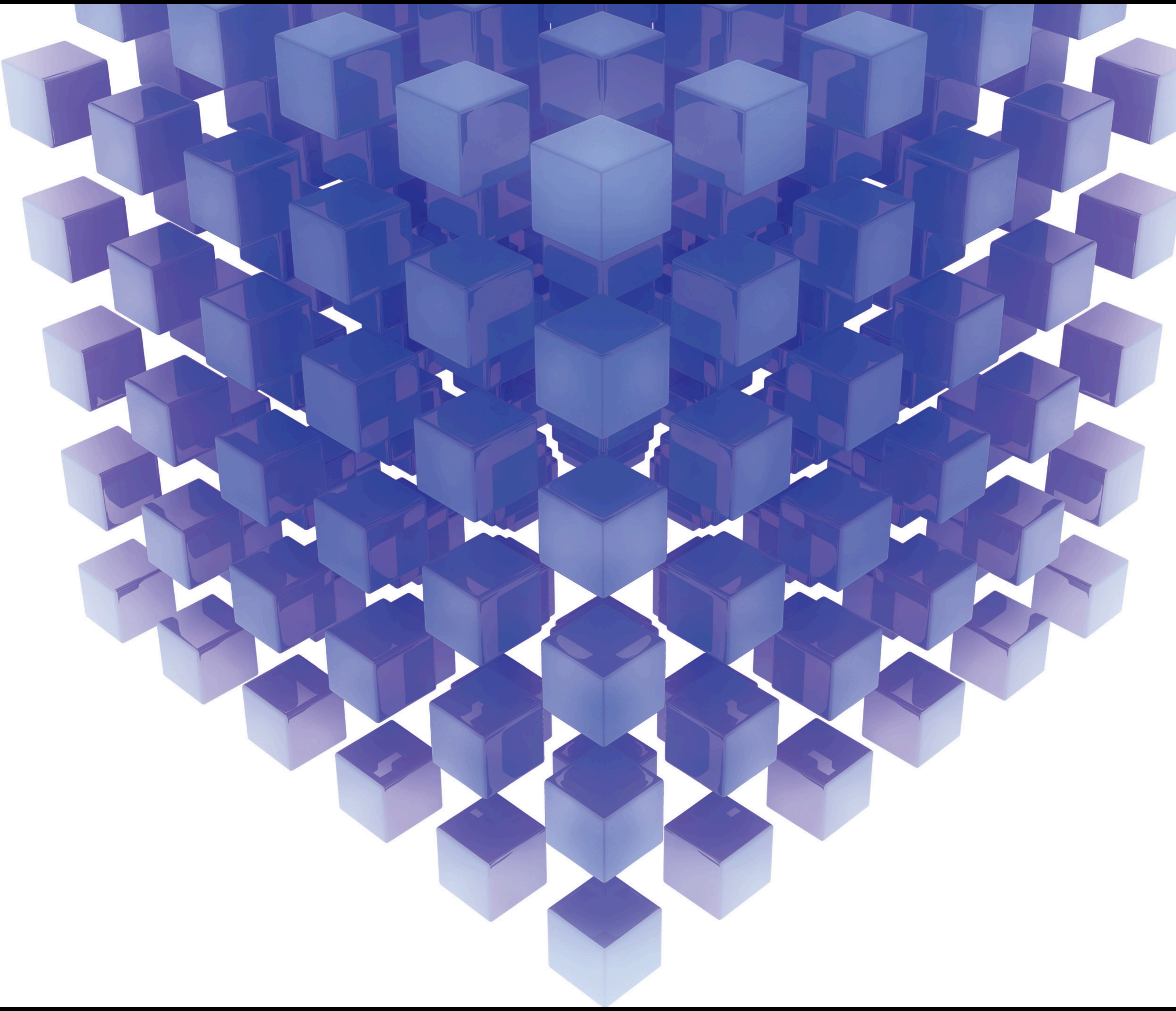

Potential Problems in Emerging Applications of Sparse Arrays 2021

Mathematical Problems in Engineering

Potential Problems in Emerging Applications of Sparse Arrays 2021

Special Issue Editor in Chief: Xiaofei Zhang
Guest Editors: Wang Zheng and Junpeng Shi

Antonio Bilotta, Italy
Sylvio R. Bistafa, Brazil
Bartłomiej Błachowski, Poland
Chiara Boccaletti, Italy
Guido Bolognesi, United Kingdom
Rodolfo Bontempo, Italy
Alberto Borboni, Italy
Marco Bortolini, Italy
Paolo Boscariol, Italy
Daniela Boso, Italy
Guillermo Botella-Juan, Spain
Boulaïd Boulkroune, Belgium
Abdesselem Boulkroune, Algeria
Fabio Bovenga, Italy
Francesco Braghin, Italy
Ricardo Branco, Portugal
Maurizio Brocchini, Italy
Julien Bruchon, France
Matteo Bruggi, Italy
Michele Brun, Italy
Maria Elena Bruni, Italy
Vasilis Burganos, Greece
Maria Angela Butturi, Italy
Raquel Caballero-Águila, Spain
Guillermo Cabrera-Guerrero, Chile
Filippo Cacace, Italy
Pierfrancesco Cacciola, United Kingdom
Salvatore Caddemi, Italy
zuowei cai, China
Roberto Caldelli, Italy
Alberto Campagnolo, Italy
Eric Campos, Mexico
Salvatore Cannella, Italy
Francesco Cannizzaro, Italy
Maosen Cao, China
Javier Cara, Spain
Raffaele Carli, Italy
Ana Carpio, Spain
Rodrigo Carvajal, Chile
Caterina Casavola, Italy
Sara Casciati, Italy
Federica Caselli, Italy
Carmen Castillo, Spain
Inmaculada T. Castro, Spain
Miguel Castro, Portugal
Giuseppe Catalanotti, United Kingdom
Nicola Caterino, Italy
Alberto Cavallo, Italy
Gabriele Cazzulani, Italy
Luis Cea, Spain
Fatih Vehbi Celebi, Turkey
Song Cen, China
Miguel Cerrolaza, Venezuela
M. Chadli, France
Gregory Chagnon, France
Ludovic Chamoin, France
Xiaoheng Chang, China
Qing Chang, USA
Ching-Ter Chang, Taiwan
Kuei-Lun Chang, Taiwan
Dr. Prasenjit Chatterjee, India
Kacem Chehdi, France
Peter N. Cheimets, USA
Chih-Chiang Chen, Taiwan
Shyi-Ming Chen, Taiwan
Xinkai Chen, Japan
Xizhong Chen, Ireland
Xue-Bo Chen, China
Kebing Chen, China
Mengxin Chen, China
Xiao Chen, China
He Chen, China
Chien-Ming Chen, China
Zhiwen Chen, China
Zeyang Cheng, China
Qiang Cheng, USA
Luca Chiapponi, Italy
Ryoichi Chiba, Japan
Francisco Chicano, Spain
Nicholas Chileshe, Australia
Tirivanhu Chinyoka, South Africa
Adrian Chmielewski, Poland
Seongim Choi, USA
Dr Gautam Choubey, India
Ioannis T. Christou, Greece
Hung-Yuan Chung, Taiwan
Yusheng Ci, China
Simone Cinquemani, Italy
Roberto G. Citarella, Italy
Joaquim Ciurana, Spain
John D. Clayton, USA
Francesco Clementi, Italy
Piero Colajanni, Italy
Giuseppina Colicchio, Italy

Vassilios Constantoudis, Greece
Francesco Conte, Italy
Enrico Conte, Italy
Alessandro Contento, USA
Mario Cools, Belgium
Gino Cortellessa, Italy
Juan Carlos Cortés, Spain
Carlo Cosentino, Italy
Paolo Crippa, Italy
Erik Cuevas, Mexico
Guozeng Cui, China
Maria C. Cunha, Portugal
Mehmet Cunkas, Turkey
Peter Dabnichki, Australia
Luca D'Acierno, Italy
Weizhong Dai, USA
Zhifeng Dai, China
Pei Dai, China
Purushothaman Damodaran, USA
Bhabani S. Dandapat, India
Giuseppe D'Aniello, Italy
Sergey Dashkovskiy, Germany
Adiel T. de Almeida-Filho, Brazil
Fabio De Angelis, Italy
Samuele De Bartolo, Italy
Abílio De Jesus, Portugal
Pietro De Lellis, Italy
Alessandro De Luca, Italy
Stefano de Miranda, Italy
Filippo de Monte, Italy
José António Fonseca de Oliveira Correia, Portugal
Jose Renato de Sousa, Brazil
Michael Defoort, France
Alessandro Della Corte, Italy
Laurent Dewasme, Belgium
Sanku Dey, India
Gianpaolo Di Bona, Italy
Angelo Di Egidio, Italy
Roberta Di Pace, Italy
Francesca Di Puccio, Italy
Ramón I. Diego, Spain
Yannis Dimakopoulos, Greece
Rossana Dimitri, Italy
Alexandre B. Dolgui, France
José M. Domínguez, Spain
Georgios Dounias, Greece
Z. Du, China
Bo Du, China
George S. Dulikravich, USA
Emil Dumic, Croatia
Bogdan Dumitrescu, Romania
Saeed Eftekhar Azam, USA
Said El Kafhali, Morocco
Antonio Elipe, Spain
R. Emre Erkmen, Canada
John Escobar, Colombia
Francisco Periago Esparza, Spain
Gilberto Espinosa-Paredes, Mexico
Leandro F. F. Miguel, Brazil
Andrea L. Facci, Italy
Shahla Faisal, Pakistan
Giovanni Falsone, Italy
Hua Fan, China
Jianguang Fang, Australia
Nicholas Fantuzzi, Italy
Muhammad Shahid Farid, Pakistan
Hamed Faroqi, Iran
Mohammad Fattahi, Iran
Yann Favennec, France
Fiorenzo A. Fazzolari, United Kingdom
Roberto Fedele, Italy
Giuseppe Fedele, Italy
Zhongyang Fei, China
Baowei Feng, China
Mohammad Ferdows, Bangladesh
Arturo J. Fernández, Spain
Jesus M. Fernandez Oro, Spain
Massimiliano Ferraioli, Italy
Massimiliano Ferrara, Italy
Francesco Ferrise, Italy
Constantin Fetecau, Romania
Eric Feulvarch, France
Iztok Fister Jr., Slovenia
Thierry Floquet, France
Eric Florentin, France
Gerardo Flores, Mexico
Antonio Forcina, Italy
Alessandro Formisano, Italy
FRANCESCO FOTI, Italy
Francesco Franco, Italy
Elisa Francomano, Italy
Juan Frausto-Solis, Mexico
Shujun Fu, China

Juan C. G. Prada, Spain
Matteo Gaeta, Italy
Mauro Gaggero, Italy
Zoran Gajic, USA
Jaime Gallardo-Alvarado, Mexico
Mosè Gallo, Italy
Akemi Gálvez, Spain
Rita Gamberini, Italy
Maria L. Gandarias, Spain
Zhong-Ke Gao, China
Xingbao Gao, China
Yan Gao, China
Hao Gao, Hong Kong
Shangce Gao, Japan
Zhiwei Gao, United Kingdom
Giovanni Garcea, Italy
José García, Chile
Luis Rodolfo Garcia Carrillo, USA
Jose M. Garcia-Aznar, Spain
Harish Garg, India
Akhil Garg, China
Alessandro Gasparetto, Italy
Gianluca Gatti, Italy
Oleg V. Gendelman, Israel
Stylianos Georgantzinos, Greece
Fotios Georgiades, India
Parviz Ghadimi, Iran
Georgios I. Giannopoulos, Greece
Agathoklis Giaralis, United Kingdom
Pablo Gil, Spain
Anna M. Gil-Lafuente, Spain
Ivan Giorgio, Italy
Gaetano Giunta, Luxembourg
Alessio Gizzi, Italy
Alireza Goli, Iran
Jefferson L.M.A. Gomes, United Kingdom
HECTOR GOMEZ, Chile
José Francisco Gómez Aguilar, Mexico
Emilio Gómez-Déniz, Spain
Antonio M. Gonçalves de Lima, Brazil
Chris Goodrich, USA
Rama S. R. Gorla, USA
Veena Goswami, India
Xunjie Gou, Spain
Jakub Grabski, Poland
Antoine Grall, France
George A. Gravvanis, Greece
Fabrizio Greco, Italy
David Greiner, Spain
Jason Gu, Canada
Federico Guarracino, Italy
Michele Guida, Italy
Muhammet Gul, Turkey
Dong-Sheng Guo, China
Hu Guo, China
Zhaoxia Guo, China
Jian-Ping Guo, China
Quang Phuc Ha, Australia
Li Haitao, China
Petr Hájek, Czech Republic
Mohamed Hamdy, Egypt
Muhammad Hamid, United Kingdom
Shigeyuki Hamori, Japan
Renke Han, United Kingdom
Weimin Han, USA
Zhen-Lai Han, China
Xingsi Han, China
Thomas Hanne, Switzerland
Xinan Hao, China
Mohammad A. Hariri-Ardebili, USA
Khalid Hattaf, Morocco
Xiao-Qiao He, China
Defeng He, China
Fu-Qiang He, China
Yanchao He, China
Yu-Ling He, China
salim HEDDAM, Algeria
Ramdane Hedjar, Saudi Arabia
Jude Hemanth, India
Reza Hemmati, Iran
Nicolae Herisanu, Romania
Alfredo G. Hernández-Diaz, Spain
M.I. Herreros, Spain
Eckhard Hitzer, Japan
Paul Honeine, France
Jaromir Horacek, Czech Republic
S. Hassan Hosseinnia, The Netherlands
Yingkun Hou, China
Xiaorong Hou, China
Lei Hou, China
Jie Hu, China
Yunfeng Hu, China
Can Huang, China
Gordon Huang, Canada

Linsheng Huo, China
Sajid Hussain, Canada
Asier Ibeas, Spain
Wubshet Ibrahim, Ethiopia
Orest V. Iftime, The Netherlands
Przemyslaw Ignaciuk, Poland
Muhammad Imran, Pakistan
Giacomo Innocenti, Italy
Emilio Insfran Pelozo, Spain
Alessio Ishizaka, France
Nazrul Islam, USA
Benoit Iung, France
Benjamin Ivorra, Spain
Breno Jacob, Brazil
Tushar Jain, India
Amin Jajarmi, Iran
Payman Jalali, Finland
Mahdi Jalili, Australia
Prashant Kumar Jamwal, Kazakhstan
Chiranjibe Jana, India
Łukasz Jankowski, Poland
Fahd Jarad, Turkey
Samuel N. Jator, USA
Juan C. Jauregui-Correa, Mexico
Kandasamy Jayakrishna, India
Reza Jazar, Australia
Khalide Jbilou, France
Isabel S. Jesus, Portugal
Chao Ji, China
Linni Jian, China
Bin Jiang, China
Qing-Chao Jiang, China., China
Peng-fei Jiao, China
Ricardo Fabricio Escobar Jiménez, Mexico
Emilio Jiménez Macías, Spain
Xiaoliang Jin, Canada
Zhuo Jin, Australia
Maolin Jin, Republic of Korea
Dylan F. Jones, United Kingdom
Ramash Kumar K, India
Viacheslav Kalashnikov, Mexico
Mathiyalagan Kalidass, India
BHABEN KALITA, USA
Tamas Kalmar-Nagy, Hungary
Zhao Kang, China
Dr.Ramani Kannan, Malaysia
Tomasz Kapitaniak, Poland
Julius Kaplunov, United Kingdom
Konstantinos Karamanos, Belgium
J. Kavikumar, Malaysia
Michal Kawulok, Poland
Irfan Kaymaz, Turkey
Vahid Kayvanfar, Iran
Krzysztof Kecik, Poland
Chaudry M. Khalique, South Africa
Mukhtaj Khan, Pakistan
Abdul Qadeer Khan, Pakistan
Mostafa M. A. Khater, Egypt
MOHAMMAD REZA KHEDMATI, Iran
Nam-Il Kim, Republic of Korea
Kwangki Kim, Republic of Korea
Philipp V. Kiryukhantsev-Korneev, Russia
P.V.V Kishore, India
Jan Koci, Czech Republic
Ioannis Kostavelis, Greece
Sotiris B. Kotsiantis, Greece
Frederic Kratz, France
Vamsi Krishna, India
Kamalanand Krishnamurthy, India
Petr Krysl, USA
Edyta Kucharska, Poland
Krzysztof S. Kulpa, Poland
Kamal Kumar, India
Michal Kunicki, Poland
Cedrick A. K. Kwuimy, USA
Kyandoghere Kyamakya, Austria
Ivan Kyrchei, Ukraine
Davide La Torre, Italy
Márcio J. Lacerda, Brazil
Risto Lahdelma, Finland
Eduardo Lalla, The Netherlands
Giovanni Lancioni, Italy
Jaroslaw Latalski, Poland
Antonino Laudani, Italy
Hervé Laurent, France
Agostino Lauria, Italy
Aimé Lay-Ekuakille, Italy
Nicolas J. Leconte, France
Kun-Chou Lee, Taiwan
Dimitri Lefebvre, France
Eric Lefevre, France
Marek Lefik, Poland
Gang Lei, Saudi Arabia
Yaguo Lei, China

Kauko Leiviskä, Finland
Thibault Lemaire, France
Ervin Lenzi, Brazil
Roman Lewandowski, Poland
Jian Li, USA
Jun Li, China
Yueyang Li, China
Yuxing Li, China
ChenFeng Li, China
Zhen Li, China
Yang Li, China
Yao-Jin Lin, China
Zhiyun Lin, China
Jian Lin, China
Mingwei Lin, China
Qibin Lin, China
En-Qiang Lin, USA
Yuanchang Liu, United Kingdom
Jianxu Liu, Thailand
Bo Liu, China
Heng Liu, China
Lei Liu, China
Wanquan Liu, China
Yu Liu, China
Sixin Liu, China
Bin Liu, China
Bonifacio Llamazares, Spain
Alessandro Lo Schiavo, Italy
Jean Jacques Loiseau, France
Francesco Lolli, Italy
Paolo Lonetti, Italy
Sandro Longo, Italy
António M. Lopes, Portugal
Sebastian López, Spain
Pablo Lopez-Crespo, Spain
Cesar S. Lopez-Monsalvo, Mexico
Luis M. López-Ochoa, Spain
Ezequiel López-Rubio, Spain
Vassilios C. Loukopoulos, Greece
Jose A. Lozano-Galant, Spain
Gabriele Maria Lozito, Italy
Songtao Lu, USA
Rongxing Lu, Canada
Zhiguo Luo, China
Gabriel Luque, Spain
Valentin Lychagin, Norway
Dazhong Ma, China
Junhai Ma, China
Junwei Ma, China
Xuanlong Ma, China
Antonio Madeo, Italy
Alessandro Magnani, Belgium
Toqeer Mahmood, Pakistan
Fazal M. Mahomed, South Africa
Arunava Majumder, India
Sarfraz Nawaz Malik, Pakistan
Paolo Manfredi, Italy
Muazzam Maqsood, Pakistan
Adnan Maqsood, Pakistan
Giuseppe Carlo Marano, Italy
Damijan Markovic, France
Filipe J. Marques, Portugal
Luca Martinelli, Italy
Guiomar Martín-Herrán, Spain
Denizar Cruz Martins, Brazil
Francisco J. Martos, Spain
Elio Masciari, Italy
Franck Massa, France
Paolo Massioni, France
Alessandro Mauro, Italy
Jonathan Mayo-Maldonado, Mexico
Fabio Mazza, Italy
Pier Luigi Mazzeo, Italy
Laura Mazzola, Italy
Driss Mehdi, France
Dr. Zahid Mehmood, Pakistan
YUE MEI, China
Roderick Melnik, Canada
Debiao Meng, China
Xiangyu Meng, USA
Jose Merodio, Spain
Alessio Merola, Italy
Mahmoud Mesbah, Iran
Luciano Mescia, Italy
Laurent Mevel, France
Constantine Michailides, Cyprus
Mariusz Michta, Poland
Prankul Middha, Norway
Aki Mikkola, Finland
Giovanni Minafò, Italy
Hiroyuki Mino, Japan
Dimitrios Mitsotakis, New Zealand
saleh mobayen, Taiwan, R.O.C., Iran
Nikunja Mohan Modak, India

Ardashir Mohammadzadeh, Iran
Sara Montagna, Italy
Roberto Montanini, Italy
Francisco J. Montáns, Spain
Gisele Mophou, France
Rafael Morales, Spain
Marco Morandini, Italy
Javier Moreno-Valenzuela, Mexico
Simone Morganti, Italy
Caroline Mota, Brazil
Aziz Moukrim, France
Shen Mouquan, China
Dimitris Mourtzis, Greece
Emiliano Mucchi, Italy
Taseer Muhammad, Saudi Arabia
Ghulam Muhiuddin, Saudi Arabia
Josefa Mula, Spain
Jose J. Muñoz, Spain
Giuseppe Muscolino, Italy
Dino Musmarra, Italy
Marco Mussetta, Italy
Ghulam Mustafa, Pakistan
Hariharan Muthusamy, India
Hakim Naceur, France
Alessandro Naddeo, Italy
Benedek Nagy, Turkey
Omar Naifar, Tunisia
Mariko Nakano-Miyatake, Mexico
Raj Nandkeolyar, India
Keivan Navaie, United Kingdom
Soumya Nayak, India
Adrian Neagu, USA
Erivelton Geraldo Nepomuceno, Brazil
Luís C. Neves, United Kingdom
AMA Neves, Portugal
Dong Ngoduy, New Zealand
Nhon Nguyen-Thanh, Singapore
Majid Niazkar, Iran
Papakostas Nikolaos, Ireland
Jelena Nikolic, Serbia
Mehrbakhsh Nilashi, Malaysia
Tatsushi Nishi, Japan
Shanzhou Niu, China
Xesús Nogueira, Spain
Ben T. Nohara, Japan
Mohammed Nouari, France
Mustapha Nourelfath, Canada
Kazem Nouri, Iran
Ciro Núñez-Gutiérrez, Mexico
Wlodzimierz Ogryczak, Poland
Roger Ohayon, France
Krzysztof Okarma, Poland
Mitsuhiro Okayasu, Japan
Murat Olgun, Turkey
Diego Oliva, Mexico
Alberto Olivares, Spain
Enrique Onieva, Spain
Calogero Orlando, Italy
Sergio Ortobelli, Italy
Naohisa Otsuka, Japan
Sid Ahmed Ould Ahmed Mahmoud, Saudi Arabia
Taoreed Owolabi, Nigeria
Cenap Özel, Turkey
Pawel Packo, Poland
Arturo Pagano, Italy
Madhumangal Pal, India
Roberto Palma, Spain
Alessandro Palmeri, United Kingdom
Pasquale Palumbo, Italy
Li Pan, China
Weifeng Pan, China
K. M. Pandey, India
Chandan Pandey, India
Rui Pang, United Kingdom
Jürgen Pannek, Germany
Elena Panteley, France
Achille Paolone, Italy
George A. Papakostas, Greece
Xosé M. Pardo, Spain
You-Jin Park, Taiwan
Manuel Pastor, Spain
Petr Páta, Czech Republic
Pubudu N. Pathirana, Australia
Surajit Kumar Paul, India
Sitek Paweł, Poland
Luis Payá, Spain
Alexander Paz, Australia
Igor Pažanin, Croatia
Libor Pekař, Czech Republic
Francesco Pellicano, Italy
Marcello Pellicciari, Italy
Zhi-ke Peng, China
Mingshu Peng, China

Bekir Sahin, Turkey
Laxminarayan Sahoo, India
Michael Sakellariou, Greece
John S. Sakellariou, Greece
Salvatore Salamone, USA
Jose Vicente Salcedo, Spain
Alejandro Salcido, Mexico
Alejandro Salcido, Mexico
Salman saleem, Saudi Arabia
Ahmed Salem, Saudi Arabia
Nunzio Salerno, Italy
Rohit Salgotra, India
Miguel A. Salido, Spain
Zabidin Salleh, Malaysia
Roque J. Saltarén, Spain
Alessandro Salvini, Italy
Abdus Samad, India
Nikolaos Samaras, Greece
Sylwester Samborski, Poland
pijush samui, India
Ramon Sancibrian, Spain
Giuseppe Sanfilippo, Italy
Omar-Jacobo Santos, Mexico
J Santos-Reyes, Mexico
José A. Sanz-Herrera, Spain
Evangelos J. Sapountzakis, Greece
Musavarah Sarwar, Pakistan
Marcelo A. Savi, Brazil
Andrey V. Savkin, Australia
Tadeusz Sawik, Poland
Roberta Sburlati, Italy
Gustavo Scaglia, Argentina
Thomas Schuster, Germany
Mijanur Rahaman Seikh, India
Tapan Senapati, China
Lotfi Senhadji, France
Junwon Seo, USA
Michele Serpilli, Italy
Joan Serra-Sagrista, Spain
Silvestar Šesnić, Croatia
Erhan Set, Turkey
Gerardo Severino, Italy
Ruben Sevilla, United Kingdom
Stefano Sfarra, Italy
Mohamed Shaat, United Arab Emirates
Mostafa S. Shadloo, France
Dr. Ismail Shah, Pakistan
Dr. Zahir Shah, Pakistan
Kamal Shah, Pakistan
Leonid Shaikhet, Israel
Vimal Shanmuganathan, India
Xingling Shao, China
Prayas Sharma, India
Xin Pu Shen, China
Bo Shen, Germany
hang shen, China
Hao Shen, China
Dimitri O. Shepelsky, Ukraine
Weichao SHI, United Kingdom
Jian Shi, China
Suzanne M. Shontz, USA
Babak Shotorban, USA
Zhan Shu, Canada
Angelo Sifaleras, Greece
Nuno Simões, Portugal
Harendra Singh, India
Rajiv Singh, India
Mehakpreet Singh, Ireland
Thanin Sitthiwirattham, Thailand
Seralathan Sivamani, India
S. Sivasankaran, Malaysia
Christos H. Skiadas, Greece
Konstantina Skouri, Greece
Neale R. Smith, Mexico
Bogdan Smolka, Poland
Delfim Soares Jr., Brazil
Alba Sofi, Italy
Francesco Soldovieri, Italy
Raffaele Solimene, Italy
Yang Song, Norway
Bosheng Song, China
Jussi Sopanen, Finland
Marco Spadini, Italy
Bernardo Spagnolo, Italy
Paolo Spagnolo, Italy
Ruben Specogna, Italy
Vasilios Spitas, Greece
Sri Sridharan, USA
Ivanka Stamova, USA
Rafał Stanisławski, Poland
Miladin Stefanović, Serbia
Florin Stoican, Romania
Salvatore Strano, Italy
Yakov Strelniker, Israel

Kumarasamy Sudhakar, Malaysia
Zong-Yao Sun, China
Qiuqin Sun, China
Shuaishuai Sun, Australia
Xiaodong Sun, China
Qiuye Sun, China
Suroso Suroso, Indonesia
Sergey A. Suslov, Australia
Nasser Hassen Sweilam, Egypt
Andrzej Swierniak, Poland
M Syed Ali, India
Andras Szekrenyes, Hungary
Kumar K. Tamma, USA
Yong (Aaron) Tan, United Kingdom
Marco Antonio Taneco-Hernández, Mexico
Hafez Tari, USA
Alessandro Tasora, Italy
Sergio Teggi, Italy
Adriana del Carmen Téllez-Anguiano, Mexico
Ana C. Teodoro, Portugal
Efstathios E. Theotokoglou, Greece
Jing-Feng Tian, China
Alexander Timokha, Norway
Stefania Tomasiello, Italy
Gisella Tomasini, Italy
Isabella Torcicollo, Italy
Francesco Tornabene, Italy
Javier Martinez Torres, Spain
Mariano Torrisi, Italy
Thang nguyen Trung, Vietnam
Sang-Bing Tsai, China
George Tsiatas, Greece
Antonios Tsourdos, United Kingdom
Le Anh Tuan, Vietnam
Federica Tubino, Italy
Nerio Tullini, Italy
Emilio Turco, Italy
Ilhan Tuzcu, USA
Efstratios Tzirtzilakis, Greece
Filippo Ubertini, Italy
Marjan Uddin, Pakistan
Mohammad Uddin, Australia
Serdar Ulubeyli, Turkey
FRANCISCO UREÑA, Spain
Panayiotis Vafeas, Greece
Giuseppe Vairo, Italy
Jesus Valdez-Resendiz, Mexico
Eusebio Valero, Spain
Stefano Valvano, Italy
Marcello Vasta, Italy
Carlos-Renato Vázquez, Mexico
Miguel E. Vázquez-Méndez, Spain
Martin Velasco Villa, Mexico
Kalyana C. Veluvolu, Republic of Korea
Franck J. Vernerey, USA
Georgios Veronis, USA
Vincenzo Vespri, Italy
Renato Vidoni, Italy
Venkatesh Vijayaraghavan, Australia
Anna Vila, Spain
Francisco R. Villatoro, Spain
Francesca Vipiana, Italy
Stanislav Vítek, Czech Republic
Jan Vorel, Czech Republic
Michael Vynnycky, Sweden
Mohammad W. Alomari, Jordan
Fu-Kwun Wang, Taiwan
C. H. Wang, Taiwan
Yung-Chung Wang, Taiwan
Zenghui Wang, South Africa
Zhenbo Wang, USA
Hao Wang, USA
Yongqi Wang, Germany
Yong Wang, China
Weiwei Wang, China
Dagang Wang, China
Bingchang Wang, China
Ji Wang, China
J.G. Wang, China
Guoqiang Wang, China
Zhibo Wang, China
Shuo Wang, China
Qingling Wang, China
Xinyu Wang, China
Hui Wang, China
Kang-Jia Wang, China
Huaiyu Wang, China
Qiang Wang, China
Roman Wan-Wendner, Austria
Fangqing Wen, China
P.H. Wen, United Kingdom
Waldemar T. Wójcik, Poland
Wai Lok Woo, United Kingdom

Qiuhong Wu, China
Xianyi Wu, China
Zhizheng Wu, China
Zhibin Wu, China
Yuqiang Wu, China
Changzhi Wu, China
Michalis Xenos, Greece
hao xiao, China
Xiao Ping Xie, China
Xue-Jun Xie, China
Hang Xu, China
Lei Xu, China
Zeshui Xu, China
Qingzheng Xu, China
Lingwei Xu, China
Qilong Xue, China
Yi Xue, China
Joseph J. Yame, France
Zhiguo Yan, China
Chuanliang Yan, China
Xinggang Yan, United Kingdom
Ray-Yeng Yang, Taiwan
Mijia Yang, USA
Jixiang Yang, China
Zaoli Yang, China
Bo Yang, China
Weilin Yang, China
Zhihong Yao, China
Min Ye, China
Jun Ye, China
Luis J. Yebra, Spain
Peng-Yeng Yin, Taiwan
Muhammad Haroon Yousaf, Pakistan
Yuan Yuan, United Kingdom
Qin Yuming, China
Abdullahi Yusuf, Nigeria
Akbar Zada, Pakistan
Elena Zaitseva, Slovakia
Arkadiusz Zak, Poland
Daniel Zaldivar, Mexico
Ernesto Zambrano-Serrano, Mexico
Francesco Zammori, Italy
Rafal Zdunek, Poland
Ahmad Zeeshan, Pakistan
Ibrahim Zeid, USA
Bo Zeng, China
Nianyin Zeng, China
Junyong Zhai, China
Xiaofei Zhang, China
Yong Zhang, China
Qian Zhang, China
Lingfan Zhang, China
Wenyu Zhang, China
Tongqian Zhang, China
Kai Zhang, China
Hao Zhang, China
Xuping Zhang, Denmark
Jian Zhang, China
Tianwei Zhang, China
Yinyan Zhang, China
Xianming Zhang, Australia
Haopeng Zhang, USA
Mingjie Zhang, Norway
Yifan Zhao, United Kingdom
Yongmin Zhong, Australia
Zebo Zhou, China
Zhe Zhou, China
Jian G. Zhou, United Kingdom
Debao Zhou, USA
Quanxin Zhu, China
Wu-Le Zhu, China
Gaetano Zizzo, Italy
Zhixiang Zou, China
Mingcheng Zuo, China

Contents

Hindawi
Mathematical Problems in Engineering
Volume 2022, Article ID 9859262, 2 pages
https://doi.org/10.1155/2022/9859262

Editorial

Potential Problems in Emerging Applications of Sparse Arrays 2021

Xiaofei Zhang,[1,2] Wang Zheng,[1,2,3] and Junpeng Shi[4]

[1]*College of Electronic and Information Engineering, Nanjing University of Aeronautics and Astronautics, Nanjing, China*
[2]*Key Laboratory of Dynamic Cognitive System of Electromagnetic Spectrum Space, Nanjing University of Aeronautics and Astronautics, Ministry of Industry and Information Technology, Nanjing, China*
[3]*The Purple Mountain Laboratories, Nanjing, China*
[4]*The College of Electronic Countermeasure, National University of Defense Technology, Changsha, China*

Correspondence should be addressed to Xiaofei Zhang; zhangxiaofei@nuaa.edu.cn

Received 25 March 2022; Accepted 25 March 2022; Published 5 May 2022

Sparse arrays, such as coprime array and nested array, can provide enlarged aperture, enhanced spatial resolution, increased degrees of freedom (DOFs), and reduced mutual coupling, which has been considerably attractive to improve active and passive sensing in radar, navigation, underwater acoustics, and wireless communications. However, the emerging applications of sparse array also bring a series of potential problems.

The special issue focuses on recent advances in application to radar and direction position determination, array geometry optimization for high accuracy DOA estimation, off-grid solutions to super-resolution, and multidimensional sparse array signal processing joint estimation. It contains six papers, the contents of which are summarized as follows.

In the study of application to radar and direction position determination, Y. Qian et al. utilize augmented coprime array for increased degree of freedom and extended array aperture and propose optimal weighting subspace data fusion (OW- SDF) algorithm and SNR weighting subspace data fusion (SW- SDF) algorithm to improve the accuracy of direct position determination in "Direct Position Determination for Augmented Coprime Arrays via Weighted Subspace Data Fusion Method."

B. Liu et al. propose a low complexity unitary estimating signal parameter via rotational invariance techniques (ESPRIT) algorithm for angle estimation in bistatic multiple-input-multiple-output (MIMO) radar in "Computationally Efficient Unitary ESPRIT Algorithm in Bistatic MIMO Radar."

In the area of array geometry optimization for high accuracy DOA estimation and off-grid solutions to super-resolution, Y. Zhang et al. propose a novel generalized nested MIMO radar by utilizing extended two-level nested array (ENA) as transmitter and receiver and adjust the interelement spacing of the receiver with an expanding factor in "DOA Estimation of a Novel Generalized Nested MIMO Radar with High Degrees of Freedom and Hole-Free Difference Coarray." B. Zhu et al. present a sparse nested array (SNA) for electromagnetic vector sensor with extended array aperture and reduced mutual coupling effect and obtain joint direction of arrival (DOA) and polarization estimates by an improved off-grid orthogonal matching pursuit method in "Electromagnetic Vector Sparse Nested Array: Array Structure Design, Off-Grid Parameter Estimation Algorithm."

Regarding multi-dimensional sparse array signal processing, S. Chen et al. propose a joint angle and frequency estimation method based on covariance reconstruction and obtain the estimation of signal parameters via rotational invariance techniques (CR-ESPRIT) in "Joint Angle and Frequency Estimation in Linear Arrays Based on Covariance Reconstruction and ESPRIT." L. Gong et al. use two antennas to receive impinging signals and utilize the conjugate symmetry characteristic of the delay matrices to extend the sample points as well as the number of clusters and obtain TOA estimates with low computational complexity by transforming the two-dimensional (2D) spectral search to one-dimensional (1D) searches in "Joint TOA and DOA

Estimation for UWB Systems with Antenna Array via Doubled Frequency Sample Points and Extended Number of Clusters."

The editors would like to thank all the authors for their contributions and acknowledge all the reviewers for their time and effort devoted to assessing the manuscripts. They also thank the Editor-in-Chief and the Editorial Office of the *Mathematical Problems in Engineering*, without which the completion of this project would not have been possible.

Conflicts of Interest

The guest editors declare that they do not have conflicts of interest regarding the publication of the special issue.

Xiaofei Zhang
Wang Zheng
Junpeng Shi

Hindawi
Mathematical Problems in Engineering
Volume 2021, Article ID 2825025, 10 pages
https://doi.org/10.1155/2021/2825025

Research Article

Direct Position Determination for Augmented Coprime Arrays via Weighted Subspace Data Fusion Method

Yang Qian,[1,2] **Zhongtian Yang**,[3] **and Haowei Zeng**[1,2]

[1]*College of Electronic Information Engineering, Nanjing University of Aeronautics and Astronautics, Nanjing 211106, China*
[2]*Key Laboratory of Dynamic Cognitive System of Electromagnetic Spectrum Space (Nanjing University of Aeronautics and Astronautics), Ministry of Industry and Information Technology, Nanjing 211106, China*
[3]*College of Energy and Power Engineering, Nanjing University of Aeronautics and Astronautics, Nanjing 211106, China*

Correspondence should be addressed to Yang Qian; qianyang@nuaa.edu.cn

Received 22 April 2021; Revised 5 June 2021; Accepted 5 July 2021; Published 15 July 2021

Academic Editor: Xiaoheng Chang

Direct position determination (DPD) for augmented coprime arrays is investigated in this paper. Augmented coprime array expands degree of freedom and array aperture and improves positioning accuracy. Because of poor stability and noise sensitivity of the subspace data fusion (SDF) method, we propose two weighted subspace data fusion (W-SDF) algorithms for direct position determination. Simulation results show that two W-SDF algorithms have a prominent promotion in positioning accuracy than SDF, Capon, and propagator method (PM) algorithm for augmented coprime arrays. SDF based on optimal weighting (OW-SDF) is slightly better than SDF based on SNR weighting (SW-SDF) in positioning accuracy. The performance for DPD of the W-SDF method with augmented coprime arrays is better than that of the W-SDF method with uniform arrays.

1. Introduction

Wireless location technology is a prominent research area in present positioning. Two-step positioning is the most commonly used in passive positioning. By utilizing the arrival time, arrival angle, and arrival frequency difference, two-step positioning constructs a mathematical model to realize positioning [1, 2]. However, there are many shortcomings in traditional two-step positioning methods. In the process of positioning, because two-step positioning experienced more intermediate processing steps, the corresponding positioning accuracy is affected [3]. In order to avoid the problem of intermediate processing steps in the two-step positioning method, in recent years, many scholars have proposed new positioning method—direct position determination [4]. Weiss proposed direct position determination in 2004 firstly [5]. Direct position determination (DPD) estimates the target position without any location intermediate parameters [6]. Because of the direct use of the original observation data, DPD makes use of the target information and effectively avoids the steps of the location intermediate parameters [7].

For reducing the computational complexity, Demmissie proposed a subspace data fusion (SDF) with higher computational efficiency in 2008 [8], which extends the ultrahigh resolution multiple signal classification angle estimation algorithm in the field of array signal processing to direct positioning. Multiple arrays receive signals from multiple different positions through fusing the received signals of multiple arrays based on the spatial spectrum estimation theory [9, 10]. Then, the SDF algorithm constructs the loss function and obtains the position estimation of emitter. Although the SDF algorithm also needs grid search, it only needs one 2D or 3D grid search in the effective space to get the position estimation of all emitters [11]. The traditional SDF algorithm based on the direct position determination algorithm does not consider the heteroscedasticity of the observation error [12–15]. So, the proposed weighted SDF method for DPD makes most of the eigenvalues and eigenvectors of the covariance matrix eigenvalue decomposition and combines with the augmented coprime array to obtain the asymptotic accuracy. The optimal position estimation performance is achieved, and the source resolution is improved [16–21].

For the problem of limited degree of freedom of uniform array, there are many research studies in traditional coprime array for direction of arrival (DOA) estimation [3, 17, 22–25]. Compared with traditional coprime arrays, augmented coprime array can use the same number of real array elements to generate more virtual arrays in the same range. And, it has a longer continuous virtual element part. Based on the existing research foundation of array signal processing introduced above, direct position determination extends from uniform array to sparse array. Now, augmented coprime array for DPD is worth studying. Single augmented coprime array or multiple augmented coprime arrays is constructed for the DPD model, and then a continuous virtual array model is constructed by spatially smoothing [14, 26–28]. So, the location loss function is constructed based on subspace data fusion for augmented arrays. This paper mainly studies the weighted subspace data fusion method based on multiple augmented coprime arrays.

We summarize the main contributions as follows:

(1) We propose two weighted subspace data fusion (W-SDF) algorithms for direct position determination to solve poor stability and noise sensitivity of the SDF algorithm. We assign a weight to the projection result at each observation position. We balance the orthogonal projection to obtain small error and high robustness loss function.

(2) We introduce multiple augmented coprime arrays into the direct position determination model and then combine with spatial smoothing subspace data fusion. We use augmented coprime arrays to increase spatial freedom and recognize more sources.

(3) We use the weighted subspace data fusion method for DPD. The proposed algorithm does not need estimation steps of intermediate parameters and avoids second loss of information.

The structure of this paper is as follows. In Section 2, we introduce some basic concepts of augmented coprime array and scene of direct position determination. Section 3 depicts the proposed W-SDF method. Section 4 depicts performance analysis about W-SDF algorithms with augmented coprime array for DPD. In Section 5, we simulate the proposed W-SDF algorithms for multiple coprime arrays and compare it with other algorithms under different arrays and different elements. And, Section 6 summarizes this paper.

Notations. $(\cdot)^*$ represents the conjugate, $(\cdot)^T$ represents the transposition, and $(\cdot)^H$ represents the conjugate transpose. The symbol $\mathrm{vec}(\cdot)$ represents the received covariance matrix virtualization, and symbol $\otimes$ represents the Kronecker product. I_n represents an $n \times n$ identity matrix, and $E(\cdot)$ represents the mathematical expectation.

2. Preliminaries

In this chapter, we introduce some basic concepts of augmented coprime array and scene of direct position determination.

2.1. Array Model. In order to use virtual array for direct position determination, augmented coprime linear array is introduced. Figure 1 shows augmented coprime linear array and the number of elements of two subarrays is $2M$ and N. The augmented coprime array element spacing is $N\ d$ and $M\ d$, M and N are coprime, and $M < N$.

2.2. Multiple Arrays Combination Positioning Model. We use the positioning scene in Figure 2. Assume that there are Q uncorrelated far-field narrow-band sources in the known two-dimensional X-Y plane. There are L observation stations with L augmented coprime arrays placed along the X-axis. The target sources are $\mathbf{p}_q = [x_q, y_q]^T$ $(q = 1, 2, \ldots, Q)$. There are L observation stations expressed as $\mathbf{u}_l = [x_{ul}, y_{ul}]^T$ $(l = 1, 2, \ldots, L)$. There are $D\,(D = 2M + N - 1)$ array elements on every observation station.

Assume that all the Q emitter signals are far-field narrow-band signals with wavelength of λ. In practice, according to the free space propagation loss model, when the signals from the same source are incident on the array at different positions, the received signal strength of the array is often different. Assuming that the power of all emitter signals is W_q and the power of the signal from the qth emitter received at the observation position $\mathbf{u}_l = [x_{ul}, y_{ul}]^T$ $(l = 1, 2, \ldots, L)$ is $W_{l,q}$, the path propagation loss coefficient can be expressed as follows:

$$b_{l,q} = \sqrt{\frac{W_{l,q}}{W_q}}, \tag{1}$$

$s_{l,q}(k)$ is recorded as the qth radiation source, and the array output signal of the lth observation station at the kth $(k = 1, 2, 3, \ldots, K)$ fast beat time is obtained as follows [7]:

$$\mathbf{r}_l(k) = \sum_{q=1}^{Q} b_{l,q}\mathbf{a}_l\left(\mathbf{p}_q\right)s_{l,q}(k) + \mathbf{n}_l(k), \tag{2}$$

where $\mathbf{n}_l(k)$ denotes the noise vector of the lth observation station and $\mathbf{a}_l(\mathbf{p}_q)$ is the direction vector, which is determined by the angle of arrival $\theta_l(\mathbf{p}_q)$ [7] as follows:

$$\theta_l\left(\mathbf{p}_q\right) = \arctan\frac{\mathbf{x}_{ul}(1) - \mathbf{p}_q(1)}{\mathbf{y}_{ul}(2) - \mathbf{p}_q(2)}. \tag{3}$$

Equation (2) can be expressed as

$$\mathbf{r}_l(k) = \mathbf{A}_l(\mathbf{p})\mathbf{s}_l(k) + \mathbf{n}_l(k), \tag{4}$$

where

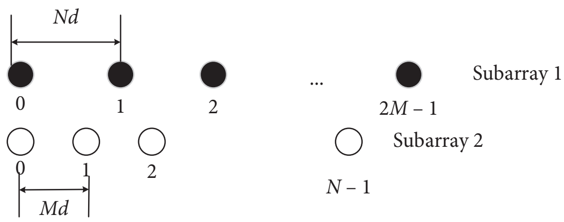

Figure 1: Augmented coprime array model.

$$
\begin{aligned}
\mathbf{A}_l(\mathbf{p}) &= \left[\mathbf{a}_1(\mathbf{p}_1), \mathbf{a}_2(\mathbf{p}_2), \ldots, \mathbf{a}_2(\mathbf{p}_Q)\right]^T,\\
\mathbf{A}_l(\mathbf{p}_q) &= \left[\mathbf{a}_{l,1}^T(\mathbf{p}_q), \mathbf{a}_{l,2}^T(\mathbf{p}_q)\right]^T,\\
\mathbf{a}_{l,1}(\mathbf{p}_q) &= \left[1, e^{-j2\pi N d \sin \theta_l(\mathbf{p}_q)}, \ldots, e^{-j2\pi(2M-1)N d \sin \theta_l(\mathbf{p}_q)}\right]^T,\\
\mathbf{a}_{l,2}(\mathbf{p}_q) &= \left[1, e^{-j2\pi M d \sin \theta_l(\mathbf{p}_q)}, \ldots, e^{-j2\pi(N-1)M d \sin \theta_l(\mathbf{p}_q)}\right]^T,\\
\mathbf{s}_l(k) &= \left[\mathbf{s}_{l,1}(k), \mathbf{s}_{l,2}(k), \ldots, \mathbf{s}_{l,Q}(k)\right]^T,\\
\mathbf{p} &= \left[\mathbf{p}_1^T, \mathbf{p}_2^T, \ldots, \mathbf{p}_Q^T\right]^T,\\
\mathbf{n}_l(k) &= \left[\mathbf{n}_{l,1}(k), \mathbf{n}_{l,2}(k), \ldots, \mathbf{n}_{l,D}(k)\right]^T.
\end{aligned}
\tag{5}
$$

3. The Proposed Algorithm

3.1. SDF Direct Position Determination Algorithm Based on Augmented Coprime Array. We can obtain the covariance matrix of array output signal from equation (4).

$$\mathbf{R}_l = E\left[\mathbf{r}_l(k)\mathbf{r}_l^H(k)\right]. \tag{6}$$

We vectorize $\mathbf{R}_l$ as follows:

$$\tilde{\mathbf{z}} = \mathrm{vec}(\mathbf{R}_l) = \mathbf{H}_l(\mathbf{p})\boldsymbol{\mu} + \sigma_n^2\mathbf{I}_n, \tag{7}$$

where $\mathbf{H}_l(\mathbf{p}) = \mathbf{A}^* \odot \mathbf{A} = [\mathbf{a}(\mathbf{p}_1) \otimes \mathbf{a}(\mathbf{p}_2), \ \mathbf{a}(\mathbf{p}_2) \otimes \mathbf{a}(\mathbf{p}_2), \ldots, \mathbf{a}(\mathbf{p}_2) \otimes \mathbf{a}(\mathbf{p}_q)]$ is the direction matrix of the virtual array, $\boldsymbol{\mu} = [\sigma_1^2, \sigma_2^2, \ldots, \sigma_q^2]^T$ is a single snapshot signal vector, and $\mathbf{I}_n = \mathrm{vec}(\mathbf{I})$, in which $\mathbf{I}$ is the identity matrix. In order to facilitate processing, we need use $\tilde{\mathbf{z}}$ to sort by phase and the remove redundancy and then get the vector $\mathbf{z}$; vector $\mathbf{z}$ is the receiving signal of the augmented matrix virtual array.

Because the spatial smoothing algorithm needs the continuity of the array elements, therefore, the vector $\mathbf{z}_1$ can be obtained by intercepting the continuous virtual elements of $\mathbf{z}$.

The intercepted virtual array is a virtual array in range $[-(MN + M - 1), MN + M - 1]$ and long uniform linear array with element spacing of d. The number of array elements is $2MN + 2M - 1$.

The basic idea of the spatial smoothing algorithm is to divide the equidistant linear array into several overlapping subarrays. If the subarrays have the same structure, their covariance matrices are added to replace the original covariance matrix.

As shown in Figure 3, we divide the intercepted virtual array into $MN + M$ overlapping subarrays. Each subarray contains $MN + M$ elements. The element position of the ith subarray is

$$\{(i + 1 + n)d, \ n = 0, 1, \ldots, MN + M - 1\}. \tag{8}$$

The received signal matrix is from line $MN + M + 1 - i$ to line $2MN + 2M + 1 - i$ of $\mathbf{z}_1$, which is denoted as $\mathbf{z}_{hi}$, and the covariance matrix is constructed [27].

$$\mathbf{R}_i = \mathbf{z}_{hi}\mathbf{z}_{hi}^H. \tag{9}$$

The covariance matrix of all $MN + M$ submatrices is summed, and the mean value is calculated to obtain the spatial smooth covariance matrix:

$$\mathbf{R}_l = \frac{1}{MN + M}\sum_{i=1}^{MN+M}\mathbf{R}_i. \tag{10}$$

Because signal and noise are independent of each other, matrix $\mathbf{R}_l$ eigenvalue decomposition can be divided into signal space and noise subspace as follows:

$$\mathbf{R}_l = [\,\mathbf{U}_l^s \ \ \mathbf{U}_l^n\,]\sum_l[\,\mathbf{U}_l^s \ \ \mathbf{U}_l^n\,]^H. \tag{11}$$

According to the orthogonal property of signal subspace and noise subspace, the projection of steering vector to noise subspace is zero only when the steering vector of array $\mathbf{a}_l(\mathbf{p})$ is composed of real emitter position parameters $\mathbf{p}_q$. Using this property, the noise subspace projection results of the steering vector to the Lth observation positions are added to construct the following loss function:

$$f_{\mathrm{SDF}}(\mathbf{p}) = \sum_{l=1}^{L}\mathbf{a}_l^H(\mathbf{p})\mathbf{U}_l^n(\mathbf{U}_l^n)^H\mathbf{a}_l(\mathbf{p}). \tag{12}$$

Obviously, the loss function processes the projection results at all observation positions equally. When one of the L spectral functions has poor performance, the loss function is vulnerable to interference; that is, the performance of the traditional SDF based on the direct localization algorithm is affected by the heteroscedasticity of orthogonal projection errors from different observation positions.

For another, SDF only uses the noise subspace resulting in vulnerable to the external factor, such as few snapshots and low SNR. Because of these factors, positioning performance is restricted. Aiming at the problem of poor stability and noise sensitivity of the SDF method, this chapter considers to obtain the loss function with small error and high robustness by balancing the orthogonal projection error. The W-SDF method makes most of all the data to improve the positioning accuracy. So, we assign a weight to the projection result at each observation position, and we construct the following loss function:

$$f_{W\text{-}\mathrm{SDF}}(\mathbf{p}) = \sum_{l=1}^{L} w_l\mathbf{a}_l^H(\mathbf{p})\mathbf{U}_l^n(\mathbf{U}_l^n)^H\mathbf{a}_l(\mathbf{p}), \tag{13}$$

where w_l is the weight of the lth observation position.

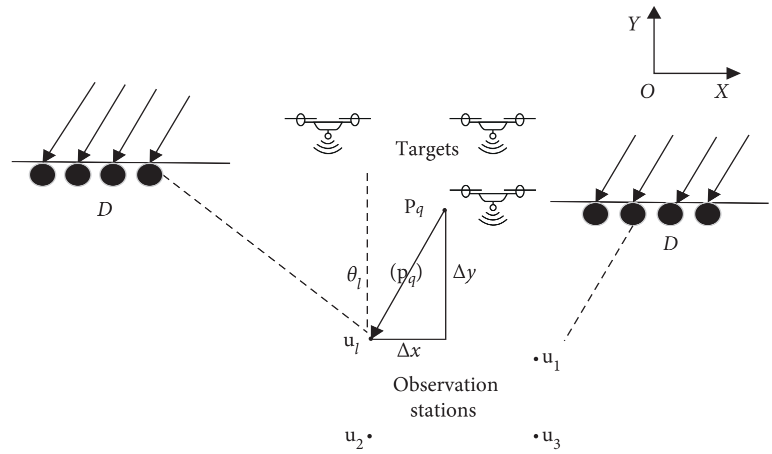

Figure 2: Multiple arrays combination positioning scene.

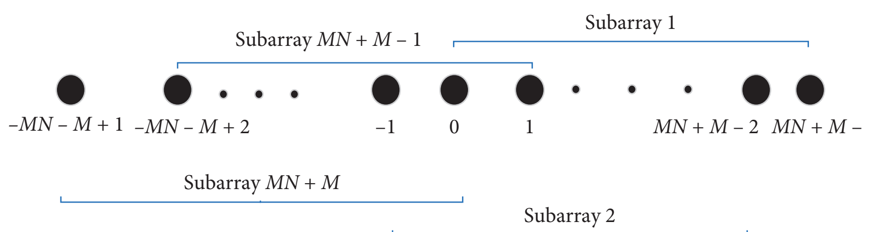

Figure 3: Spatial smoothing diagram.

3.2. Direct Position Determination Based on SNR Weighted SDF. According to the principle of power allocation based on water injection principle, we allocate more power into the channel with good quality and we allocate less power into the channel with poor quality. So, we can obtain the maximum channel capacity. Similarly, in order to reduce the total projection error, we need to design a weight that makes it increase when error decreases. Because high SNR leads to small positioning error and low SNR results in large positioning error. So, in this section, we propose SNR weighted subspace data fusion (SW-SDF) for DPD.

Under the assumption that the noises are uncorrelated and the signals and noises are independent each other, the form of the covariance matrix can be rewritten by substituting equation (4) into (11):

$$\widehat{R}_l = \frac{1}{K}\sum_{k=1}^{K}\left(\sum_{q=1}^{Q} b_{l,q}^2 W_q \mathbf{a}_l(\mathbf{p})\mathbf{a}_l^H(p) + \sigma_n^2 \mathbf{I}_{V\times V}\right), \tag{14}$$

where $\mathbf{I}_{V\times V}$ is identity matrix of $V\times V$, in which $V = MN + M$. The same array receives different power of different radiation sources. And, different arrays receive different power from the same array. These all depend on the signal power W_q and unknown parameters $b_{l,q}$. We assumed that the noise power is constant in the whole observation process, so the SNR of different observation positions is proportional to $b_{l,q}^2 W_q$, that is, $W_{l,q}$; this value is unknown in practical application.

The received signal covariance matrix can be decomposed into two parts:

$$\widehat{R}_l = \mathbf{R}_s + \mathbf{R}_n = \mathbf{A}_l(\mathbf{p})\mathrm{diag}\left(\left[W_{l,1},\ldots,W_{l,Q}\right]\right)\mathbf{A}_l^H(\mathbf{p}) + \sigma_n^2\mathbf{I}_{V\times V}. \tag{15}$$

Under the same assumption, the eigenvalue can be expressed as

$$\lambda_{l,i} = \begin{cases} \sigma_{y_i}^2 + \sigma_n^2, & 1\le i\le Q,\\ \sigma_n^2, & Q+1\le i\le V, \end{cases} \tag{16}$$

is large nonzero eigenvalues of $\mathbf{R}_s$, $\sigma_{y_i}^2$ denotes the power Wl,q of the received signal. It is assumed that the noise power is constant in the observation process, and its specific value is unknown in practice. According to equation (16), the estimated value of noise power can be calculated by $V - Q$ smaller eigenvalue as follows:

$$\widehat{\sigma}_{nl}^2 = \frac{1}{V-Q}\sum_{i=Q+1}^{V}\lambda_{l,i}. \tag{17}$$

Due to the small deviation between the estimated value and the real value, the estimated values of the noise power at different observation positions are approximately equal. According to the estimated value of the noise power, the l th observation station can obtain the power as follows:

$$\widehat{W}_l = \sum_{i=1}^{Q}\left(\lambda_{l,i} - \widehat{\sigma}_{nl}^2\right). \tag{18}$$

According to the previous analysis, the position with large SNR of the received signal will produce smaller error. So, we give larger weight to the position, that is, the SNR of the received signal for this position. Therefore, the loss function of the direct position determination algorithm based on SNR weighting can be constructed as follows:

$$f_{\text{SW-SDF}}(\mathbf{p}) = \sum_{l=1}^{L} \frac{W_l}{\widehat{\sigma}_{nl}^2} \left\| \left(\mathbf{U}_l^n\right)^H \mathbf{a}_l(\mathbf{p}) \right\|^2. \tag{19}$$

By searching the front Q minimum values of equation (19), the high precision emitter position estimation results can be obtained.

3.3. Direct Position Determination Based on Optimal Weighting. In the previous chapter, we introduce the SW-SDF algorithm for DPD that can effectively reduce the total projection error of L observation positions, but the SW-SDF algorithm does not achieve the minimum of the total projection error. So, it is not optimal. In this section, the optimal weighted subspace data fusion (OW-SDF) algorithm for DPD is proposed. The projection error between the steering vector and the noise subspace obtained from the first observation position is defined as

$$\boldsymbol{\xi}_l = \left(\mathbf{U}_l^n\right)^H \mathbf{a}_l(\mathbf{p}). \tag{20}$$

Then, the optimal weighted direct position determination problem can be expressed as finding an optimal weight T^* and emitter position estimation $\widehat{p}$ to minimize the total projection error, that is, the optimal weighted direct position determination problem:

$$\widehat{p}, T^* = \arg\min_{\mathbf{p},\mathbf{W}} \left\| T^{1/2} \boldsymbol{\xi} \right\|^2, \tag{21}$$

where $\xi = [\xi_1^H, \xi_2^H, \ldots, \xi_L^H]^H$ is projection error of all observation positions.

According to reference [15], the projection error vector ξ_l is a variable of zero mean Gaussian distribution, and its covariance matrix has the following form:

$$\begin{aligned} E\left(\boldsymbol{\xi}_i \boldsymbol{\xi}_j^H\right) &= \mathbf{a}_l^H(\mathbf{p}) \boldsymbol{\Lambda}_l \mathbf{a}_l(\mathbf{p}) \boldsymbol{\delta}_{i,j} \mathbf{I}_{(V-Q)\times(V-Q)}, \\ E\left(\boldsymbol{\xi}_i \boldsymbol{\xi}_j^T\right) &= 0_{(V-Q)\times(V-Q)}, \quad \text{for } \forall i, j, \end{aligned} \tag{22}$$

where $\mathbf{I}_{(V-Q)\times(V-Q)}$ and $\mathbf{I}_{(V-Q)\times(V-Q)}$ are $V \times V$ identity matrix and $(V-Q)\times(V-Q)$ zero matrix, $\delta_{i,j}$ is an impulse variable, if and only if $i = j$, $\delta_{i,j} = 1$, the other cases $\delta_{i,j}$ are zero, and the matrix Λ_l has the following form:

$$\boldsymbol{\Lambda}_l = \frac{1}{K} \mathbf{U}_l^s \operatorname{diag}\left(\left[\frac{\lambda_{l,1}}{\sigma_n^2} + \frac{\sigma_n^2}{\lambda_{l,1}} - 2, \ldots, \frac{\lambda_{l,Q}}{\sigma_n^2} + \frac{\sigma_n^2}{\lambda_{l,Q}} - 2 \right] \right) \left(\mathbf{U}_l^s\right)^H. \tag{23}$$

It can be seen from equation (22) that the subvectors ξ_l of the error vector ξ are independent of each other, so we can get that the covariance matrix of the error vector ξ is a $(V-Q)L \times (V-Q)L$ matrix, and each matrix $E(\xi_l \xi_l^H), l = 1, 2, \ldots, L$ is expressed as

$$\operatorname{cov}(\boldsymbol{\xi}) = E\left(\boldsymbol{\xi}\boldsymbol{\xi}^H\right) = \operatorname{diagblk}\left(\left[E\left(\boldsymbol{\xi}_1 \boldsymbol{\xi}_1^H\right), \ldots, E\left(\boldsymbol{\xi}_L \boldsymbol{\xi}_L^H\right) \right] \right). \tag{24}$$

By substituting equations (22) and (23) into equation (24), the solution of the optimal weight can be obtained

$$T^* = \operatorname{diag}\left(\left[t_1^*, \ldots, t_L^* \right] \right) \otimes \mathbf{I}_{(V-Q)\times(V-Q)}, \tag{25}$$

where

$$t_l^*(\mathbf{p}) = \frac{1}{\sum_{q=1}^{Q} g_{l,q} \left\| \left(\mathbf{U}_l^s\right)^H \mathbf{a}_l(\mathbf{p}) \right\|^2}, \tag{26}$$

where $g_{l,q}$ is the weight of the signal from the radiation source Q in the received signal of l th array and $g_{l,q}$ is related to SNR and can be expressed as

$$g_{l,q} = \left(\rho_{l,q} + \frac{1}{\rho_{l,q}} - 2 \right)^{-1}, \tag{27}$$

where $\rho_{l,q} = 1 + \text{SNR}_{l,q} = \lambda_{l,q}/\sigma_n^2$. According to equation (27), the optimal weight not only considers the difference between the received signal SNR but also considers the noise subspace and search grid points.

According to equation (25), the loss function of the direct position determination algorithm based on optimal weight can be constructed as follows:

$$f_{\text{OW-SDF}}(\mathbf{p}) = \sum_{l=1}^{L} \frac{\left\| \left(\mathbf{U}_l^n\right)^H \mathbf{a}_l(\mathbf{p}) \right\|^2}{\left\| \operatorname{diag}\left(\left[g_{l,1}^{1/2}, \ldots, g_{l,Q}^{1/2} \right] \right) \left(\mathbf{U}_l^s\right)^H \mathbf{a}_l(\mathbf{p}) \right\|^2}. \tag{28}$$

By searching the front Q minimum values of equation (28), the high precision emitter position estimation results can be obtained.

3.4. The Procedure of the Proposed Algorithm. We summarize several steps about W-SDF algorithms as follows:

Step 1. Construct the sources model and augmented coprime array positioning model for DPD.

Step 2. Adopt the vector and spatial smoothing method for receiving signals.

Step 3. Calculate the covariance matrix to get noise subspace $\mathbf{U}_l^n$. Assign a weight to the projection result at each observation position.

Step 4. Construct the cost function $f_{W\text{-SDF}}(\mathbf{p})$. The coordinate corresponding to the peak value is the position estimation value $(\widehat{x}_q, \widehat{y}_q)$.

4. Performance Analysis

4.1. Achievable DOFs. In this paper, we use augmented coprime array which increases spatial degree of freedom than uniform linear array. The DOFs of the augmented coprime array are $2MN + 2M - 1$, and the DOFs of the uniform linear array are $2M + N - 1$. It can be obviously seen that the degree of freedom of augmented coprime array is higher than freedom of uniform linear array.

4.2. Computational Complexity. The computational complexity of the proposed two weighted direct position determination algorithms is compared with SDF direct position determination for augmented coprime array, which only considers the number of complex multiplication. The computational complexity of W-SDF and SDF algorithms is related to the following parameters: L denotes the number of observation positions, Q denotes the number of targets, D denotes the number of array elements, and K denotes the number of snapshots; we divide X direction into L_x equal parts in global search and divide Y direction into L_y equal parts.

For the direct position determination algorithm SW-SDF and OW-SDF, the complexity of the algorithm includes the following aspects: the calculation of the covariance matrix of dimension receiving signal $O(KD^2)$, the decomposition of eigenvalue of the covariance matrix of the dimension receiving signal $O(V^3)$, and the calculation of spectral peak value of each searching grid point $O(V^2(V-Q)+V^2+V)$. In addition, the weight calculation in the SW-SDF algorithm does not need to increase the additional computational complexity. The OW-SDF algorithm computational complexity is $O(LKD^2 + LV^3 + LL_xL_y(V^2(V-Q)+2V^2+2V))$. In summary, the computational complexity of the three direct positioning algorithms is shown in Table 1.

Figure 4 shows the comparison of the complexity of several algorithms with the number of search points in X (or Y) direction under specific parameters. The simulation parameters are set as follows: the number of observation positions $L = 5$, the number of radiation sources $Q = 3$, two subarrays are $M = 3$ and $N = 5$, the number of augmented array elements $D = 10$, the number of snapshots $K = 100$, the number of array elements after smoothing is $V = 18$, and the number of search points along X and Y directions, with the range of 100 to 1000. The computational complexity of the PM algorithm is slightly lower than that of SDF and SW-SDF algorithms. The computational complexity of the Capon algorithm is higher than that of other algorithms. Compared with the SDF method, SW-SDF can improve the positioning performance without increasing the complexity. The complexity of the OW-SDF algorithm is slightly higher than that of the SW-SDF algorithm, but the positioning performance is greatly improved. We will explain this in detail in the subsequent simulation analysis.

4.3. Advantage. Based on the above research, we make a list of advantages about W-SDF algorithms for coprime array:

(1) The proposed W-SDF algorithms do not need any parameter estimation step, avoid the secondary loss of information, and effectively improve the positioning accuracy.

(2) The proposed W-SDF algorithms use augmented coprime array characteristics. Compared with the algorithm of uniform array, there is a significant improvement in DOF. The spatial freedom of the array can be expanded, and the number of identified sources is increased.

(3) We assign a weight to the projection result at each observation position and construct the loss function. Aiming at the problem of poor stability and noise sensitivity of the SDF method, this paper considers to obtain the loss function with small error and high robustness by balancing the orthogonal projection error and makes most of the data to improve the positioning accuracy.

5. Simulation Results

5.1. Simulations Results versus Proposed Algorithm. There are 5 augmented coprime arrays located at 5 observation stations. Each station has an augmented coprime array. The locations of observations are $\mathbf{U}_1 = [-1000\,\text{m}, -500\,\text{m}]$, $\mathbf{U}_1 = [-500\,\text{m}, -500\,\text{m}]$, $\mathbf{U}_3 = [0\,\text{m}, -500\,\text{m}]$, $\mathbf{U}_4 = [500\,\text{m}, -500\,\text{m}]$, and $\mathbf{U}_5 = [1000\,\text{m}, -500\,\text{m}]$. Multiple targets are $\mathbf{P}_1 = [100\,\text{m}, 100\,\text{m}]$, $\mathbf{P}_2 = [300\,\text{m}, 300\,\text{m}]$, and $\mathbf{P}_3 = [700\,\text{m}, 700\,\text{m}]$, and Figure 5 denotes direct position determination cost function with the SNR weighting algorithm. Figure 6 denotes the direct position determination scatter diagram with the SNR weighting algorithm. Figure 7 denotes direct position determination with the optimal weighting algorithm. Figure 8 denotes the direct position determination scatter diagram with the optimal weighting algorithm.

In these simulation experiments, the performance of the proposed W-SDF method is analyzed by calculating the root mean square error (RMSE), and it can be expressed as

$$\text{RMSE} = \frac{1}{Q}\sqrt{\frac{1}{\text{MC}}\sum_{mc=1}^{\text{MC}}\sum_{q=1}^{Q}\left\|\mathbf{p}_q - \widehat{\mathbf{p}}_{q,mc}\right\|^2}, \tag{29}$$

where MC is the number of the Monte Carlo (MC) simulation test, Q is the number of target sources, $\widehat{\mathbf{p}}_{q,mc}$ denotes the mc th Monte Carlo estimated value of the location of the qth target, and $\mathbf{p}_q$ is the real value of the qth target.

5.2. RMSE Results versus Comparison of W-SDF Algorithms with Other Algorithms. This paper simulates the comparison of different algorithms with augmented coprime array. The number of augmented coprime array elements is $(M, N) = (3, 5)$, and there are multiple targets $\mathbf{P}_1 = [100\,\text{m}, 100\,\text{m}]$, $\mathbf{P}_2 = [300\,\text{m}, 300\,\text{m}]$, and $\mathbf{P}_3 = [700\,\text{m}, 700\,\text{m}]$. The snapshot number is 100. Each station has an augmented coprime array. Figure 9 shows that the performance for DPD of the W-SDF algorithm is better than that of the SDF and PM algorithm for augmented coprime array. OW-SDF is slightly better than SW-SDF in positioning accuracy. CRB for augmented coprime array is simulated in Figure 9.

Table 1: Computational complexity of different algorithms.

Algorithms	Computational complexity	Running time (s)
SDF	$O(LKD^2 + LV^3 + LL_xL_y(V^2(V-Q) + V^2 + V))$	32.867873
SW-SDF	$O(LKD^2 + LV^3 + LL_xL_y(V^2(V-Q) + V^2 + V))$	32.180425
OW-SDF	$O(LKD^2 + LV^3 + LL_xL_y(V^2(V-Q) + 2V^2 + 2V))$	36.953023
Capon	$O(LKD^2 + LL_xL_y(V^3 + V^2 + V))$	101.878995
PM	$O(LKD^2 + L(2Q^2V + QV(V-Q) + Q^3) + LL_xL_y(V^2(V-Q) + V^2 + V))$	23.165267

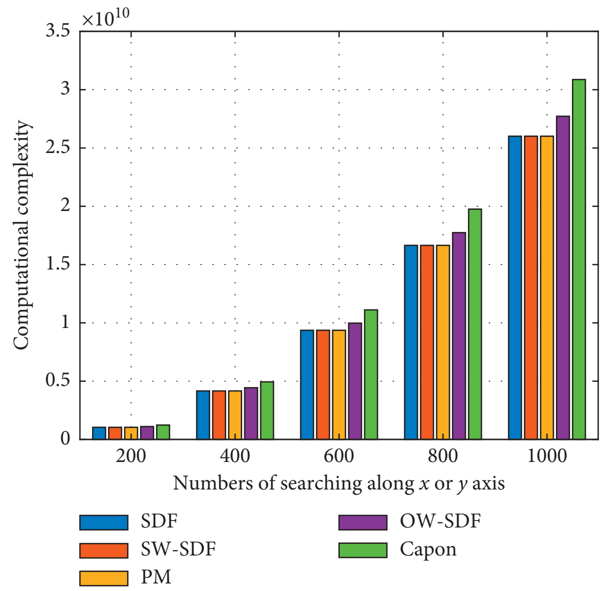

Figure 4: Comparison of different algorithms in computational complexity.

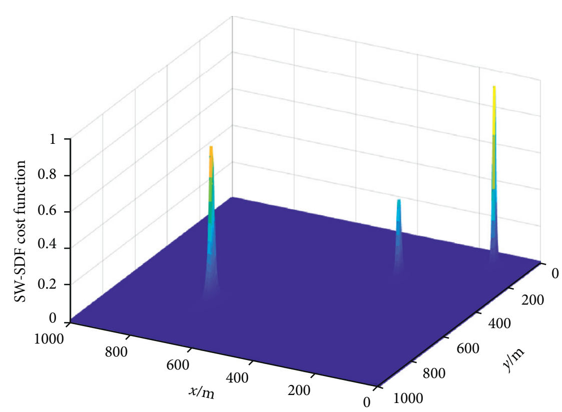

Figure 5: SW-SDF direct position determination.

5.3. RMSE Results versus Comparison of W-SDF Algorithms under Different Snapshot Numbers for Augmented Coprime Array. This paper simulates the comparison of different algorithms with different snapshot numbers for augmented coprime array. The number of augmented coprime array elements is $(M, N) = (3, 5)$, and there are multiple targets $\mathbf{P}_1 = [100\,\mathrm{m}, 100\,\mathrm{m}]$, $\mathbf{P}_2 = [300\,\mathrm{m}, 300\,\mathrm{m}]$, and $\mathbf{P}_3 = [700\,\mathrm{m}, 700\,\mathrm{m}]$. Each station has an augmented coprime array. Figure 10 shows that as the number of snapshots increases, the performance for DPD with augmented coprime array of W-SDF algorithms is better than that of SDF, Capon, and PM algorithms.

5.4. RMSE Results versus Comparison of W-SDF Algorithms under Different Arrays. This paper simulates the comparison of different algorithms with augmented coprime array and uniform array. The number of augmented coprime array elements is $(M, N) = (3, 5)$, and there are multiple targets $\mathbf{P}_1 = [100\,\mathrm{m}, 100\,\mathrm{m}]$, $\mathbf{P}_2 = [300\,\mathrm{m}, 300\,\mathrm{m}]$, and $\mathbf{P}_3 = [700\,\mathrm{m}, 700\,\mathrm{m}]$. Each station has an augmented coprime array. The snapshot number is 100. Figure 11 shows that as SNR increases, the performance of W-SDF algorithms for DPD with augmented coprime array is better than that of W-SDF and SDF algorithms with uniform array.

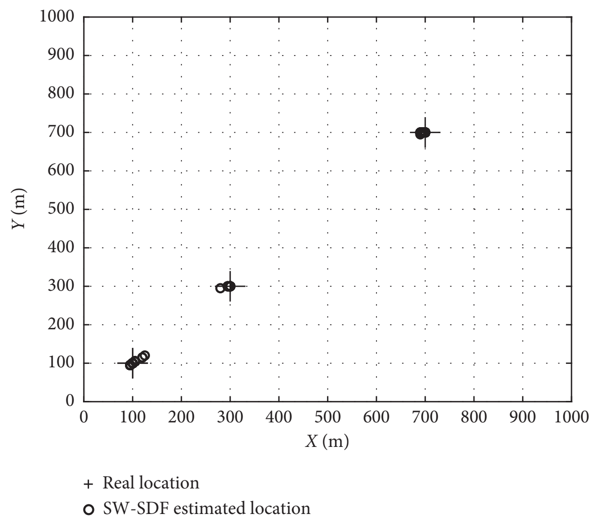

Figure 6: SW-SDF direct position determination scatters.

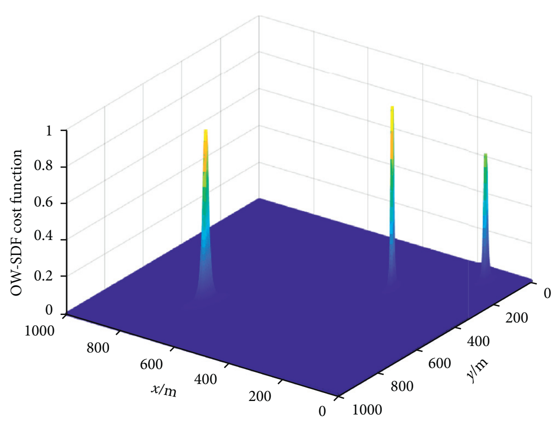

Figure 7: OW-SDF direct position determination.

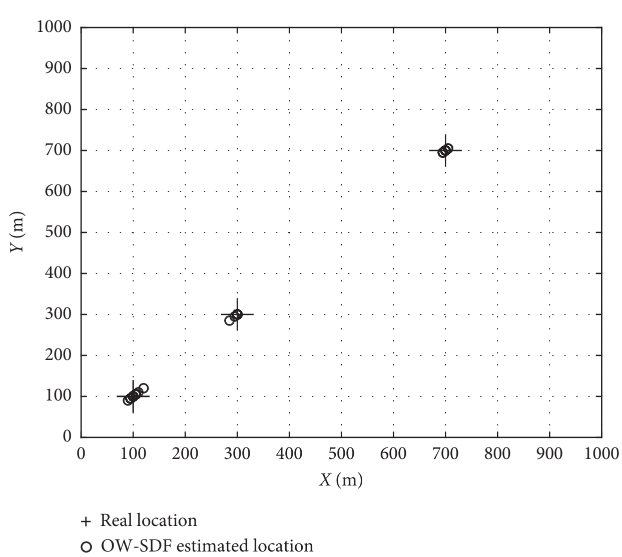

Figure 8: OW-SDF direct position determination scatters.

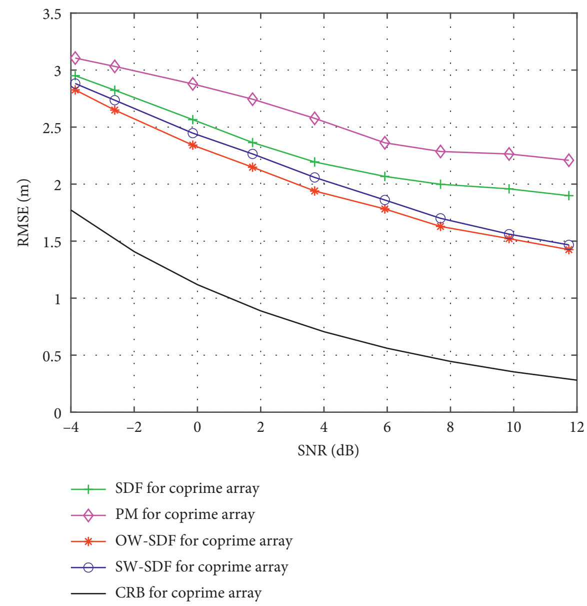

Figure 9: Comparison of different algorithms for coprime array.

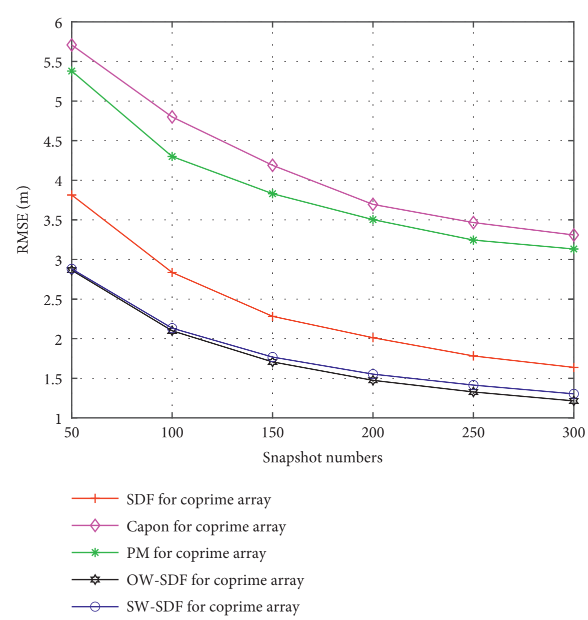

Figure 10: Comparison of different algorithms with snapshot numbers.

5.5. RMSE Results versus Comparison of W-SDF Algorithms under Different Elements. This paper simulates the comparison of different algorithms with different elements. There are multiple targets $\mathbf{P}_1 = [100\,\mathrm{m}, 100\,\mathrm{m}]$, $\mathbf{P}_2 = [300\,\mathrm{m}, 300\,\mathrm{m}]$, and $\mathbf{P}_3 = [700\,\mathrm{m}, 700\,\mathrm{m}]$. Each station has an augmented coprime array. Set the number of elements $(M1, N1) = (3, 5)$, $(M2, N2) = (3, 7)$, and $(M3, N3) = (5, 7)$. The snapshot number is 100. In Figure 12, simulation results show that performance of the proposed W-SDF algorithms is better with increment of elements.

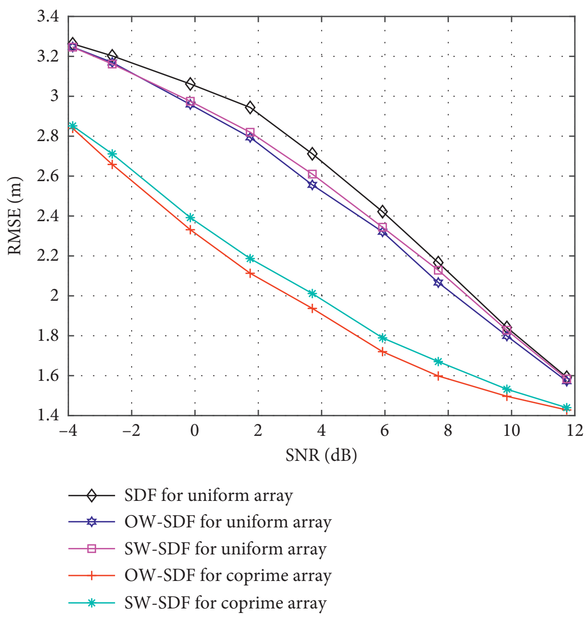

FIGURE 11: Comparison of algorithms with uniform array and coprime array.

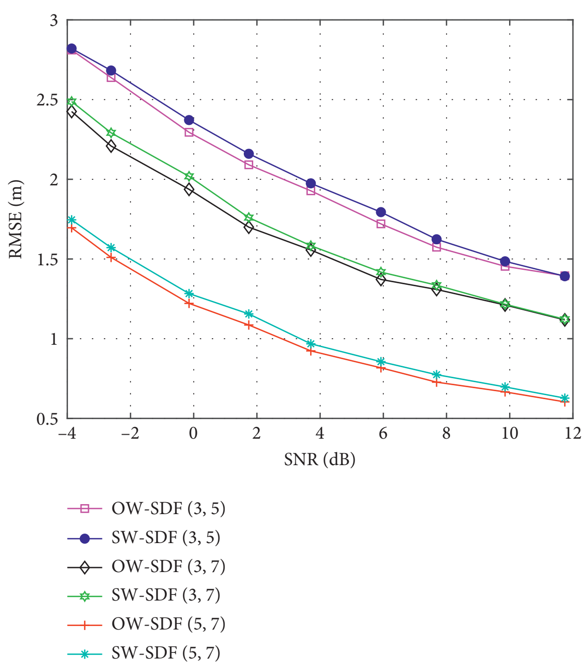

FIGURE 12: Comparison of W-SDF with different elements.

6. Conclusion

We introduce multiple augmented coprime arrays into the direct position determination model, which increases spatial freedom and position accuracy. We assign a weight to the projection result at each observation position to obtain better positioning accuracy. Simulation results show that two W-SDF algorithms have a prominent promotion in positioning accuracy than SDF, Capon, and PM algorithms for augmented coprime arrays. OW-SDF is slightly better than SW-SDF in positioning accuracy. The performance for DPD of the W-SDF method with augmented coprime arrays is better than that of the W-SDF method with uniform arrays.

Data Availability

The data used to support the findings of this study are included within the article.

Conflicts of Interest

The authors declare that they have no conflicts of interest.

Acknowledgments

This work was supported by China NSF (Grants 61971217, 61971218, and 61631020), Jiangsu NSF (Grant BK20200444), the fund of Sonar Technology Key Laboratory (Research on the theory and algorithm of signal processing for two-dimensional underwater acoustics coprime array) and the Fund of Sonar Technology Key Laboratory (Range estimate and location technology of passive target via multiple array combination), and Jiangsu Key Research and Development Project (Grant BE2020101).

References

[1] T. Tirer and A. J. Weiss, "High resolution direct position determination of radio frequency sources," *IEEE Signal Processing Letters*, vol. 23, no. 2, pp. 192–196, 2016.

[2] K. Hao and Q. Wan, "High resolution direct detection and position determination of sources with intermittent emission," *IEEE Access*, vol. 7, pp. 43428–43437, 2019.

[3] C. Zhou, Y. Gu, X. Fan, Z. Shi, G. Mao, and Y. D. Zhang, "Direction-of-arrival estimation for coprime array via virtual array interpolation," *IEEE Transactions on Signal Processing*, vol. 66, no. 22, pp. 5956–5971, 2018.

[4] Y. Zhang, Y. Xu, B. Ba, D. M. Wang, and W. Geng, "Direct position determination of non-circular sources based on a Doppler-extended aperture with a moving coprime array," *IEEE Access*, vol. 6, pp. 61014–61021, 2018.

[5] A. J. Weiss, "Direct position determination of narrowband radio frequency transmitters," *IEEE Signal Processing Letters*, vol. 11, no. 5, pp. 513–516, 2004.

[6] A. Moffet, "Minimum-redundancy linear arrays," *IEEE Transactions on Antennas and Propagation*, vol. 16, no. 2, pp. 172–175, 1968.

[7] J. Yin, D. Wang, and Y. Wu, "An efficient direct position determination method for multiple strictly noncircular sources," *IEEE Sensors Journal*, vol. 18, no. 2, p. 324, 2018.

[8] B. Demissie, M. Oispuu, and E. Ruthotto, "Localization of multiple sources with a moving array using subspace data fusion," in *Proceedings of the 2008 11th International Conference Information Fusion*, pp. 1–7, Cologne, Germany, June 2018.

[9] W. Wang, S. Ren, and Z. Chen, "Unified coprime array with multiperiod subarrays for direction-of-arrival estimation," *Digital Signal Processing*, vol. 74, pp. 30–42, 2018.

[10] P. Pal and P. Vaidyanathan, "Nested arrays: a novel approach to array processing with enhanced degrees of freedom," *IEEE Transactions on Signal Processing*, vol. 58, no. 8, pp. 4167–4181, 2010.

[11] C. Liu and P. Vaidyanathan, "Super nested arrays: linear sparse arrays with reduced mutual coupling-Part I:

fundamentals," *IEEE Transactions on Signal Processing*, vol. 64, no. 15, pp. 3997–4012, 2016.
[12] J. Yin, Y. Wu, and D. Wang, "Direct position determination of multiple noncircular sources with a moving array," *Circuits, Systems, and Signal Process*, vol. 36, no. 10, pp. 405–407, 2017.
[13] Y. Zhang, B. Ba, D. Wang, W. Geng, and H. Xu, "Direct position determination of multiple non-circular sources with a moving coprime array," *IEEE Sensors Journal*, vol. 18, no. 5, pp. 1–17, 2018.
[14] J. Li and X. Zhang, "Direction of arrival estimation of quasi-stationary signals using unfolded coprime array," *IEEE Access*, vol. 5, pp. 6538–6545, 2017.
[15] P. Stoica and N. Arye, "MUSIC, maximum likelihood, and cramer-rao bound," *IEEE Transactions on Acoustics, Speech and Signal Process*, vol. 38, no. 5, pp. 720–741, 1989.
[16] J. Li, L. Yang, F. Guo, and W. Jiang, "Coherent summation of multiple short-time signals for direct positioning of a wide-band source based on delay and Doppler," *Digital Signal Processing*, vol. 48, pp. 58–70, 2016.
[17] S. Qin, Y. Zhang, and M. Amin, "Generalized coprime array configurations for direction-of-arrival estimation," *IEEE Transactions on Signal Processing*, vol. 63, no. 22, pp. 1377–1390, 2015.
[18] Q. Liu, J. Xu, and Z. Ding, "Target localization with jammer removal using frequency diverse array," *IEEE Transactions on Vehicular Technology*, vol. 69, no. 10, pp. 11685–11696, 2020.
[19] X. Zhang, W. Chen, and W. Zheng, "Localization of near-field sources: a reduced-dimension MUSIC algorithm," *IEEE Communications Letters*, vol. 22, no. 7, pp. 1422–1425, 2018.
[20] H. Zhang, W. Liu, Z. Zhang, W. Lu, and J. Xie, "Joint target assignment and power allocation in multiple distributed MIMO radar networks," *IEEE Systems Journal*, vol. 15, no. 1, pp. 694–704, 2021.
[21] H. Zhang, J. Shi, Q. Zhang, B. Zong, and J. Xie, "Antenna selection for target tracking in collocated MIMO radar," *IEEE Transactions on Aerospace and Electronic Systems*, vol. 57, no. 1, pp. 423–436, 2021.
[22] X. Zhang and D. Xu, "Angle estimation in bistatic MIMO radar using improved reduced dimension Capon algorithm," *Journal of Systems Engineering and Electronics*, vol. 24, no. 1, pp. 84–89, 2013.
[23] X. Zhang, L. Xu, L. Xu, and D. Xu, "Direction of departure (DOD) and direction of arrival (DOA) estimation in MIMO radar with reduced-dimension MUSIC," *IEEE Communications Letters*, vol. 14, no. 12, pp. 1161–1163, 2010.
[24] J. Wang, G. Ding, Q. Wu, L. Shen, and F. Song, "Spatial-temporal spectrum hole discovery: a hybrid spectrum sensing and geolocation database framework," *Chinese Science Bulletin*, vol. 59, no. 16, pp. 1896–1902, 2014.
[25] P. Gupta and M. Agrawal, "Design and analysis of the sparse array for DOA estimation of noncircular signals," *IEEE Transactions on Signal Processing*, vol. 67, no. 2, pp. 460–473, 2019.
[26] J. Shi, G. Hu, X. Zhang, F. Sun, and H. Zhou, "Sparsity-based two-dimensional doa estimation for coprime array: from sum-difference co-array viewpoint," *IEEE Transactions on Signal Processing*, vol. 65, no. 21, pp. 5591–5604, 2017.
[27] W. Zheng, X. Zhang, and H. Zhai, "Generalized coprime planar array geometry for 2-d doa estimation," *IEEE Communications Letters*, vol. 21, no. 5, pp. 1075–1078, 2017.
[28] W. Zheng, X. Zhang, P. Gong, and H. Zhai, "DOA estimation for coprime linear arrays: an ambiguity-free method involving full DOFs," *IEEE Communications Letters*, vol. 22, no. 3, pp. 562–565, 2017.

Hindawi
Mathematical Problems in Engineering
Volume 2021, Article ID 5477848, 15 pages
https://doi.org/10.1155/2021/5477848

Research Article

Joint Angle and Frequency Estimation in Linear Arrays Based on Covariance Reconstruction and ESPRIT

Shihong Chen,[1] **Qingchang Tao**,[2] **Zhongtian Yang**,[3] **Xudong Wang**,[1] **Sijia Liu**,[1] **and Wei Xu**[1]

[1]*Key Laboratory of Radar Imaging and Microwave Photonics, College of Electronic and Information Engineering, Nanjing University of Aeronautics and Astronautics, Nanjing 211106, China*
[2]*Department of Precision Instrument, State Key Laboratory of Precision Measurement Technology and Instruments, Tsinghua University, Beijing 100084, China*
[3]*College of Energy and Power Engineering, Nanjing University of Aeronautics and Astronautics, Nanjing 211106, China*

Correspondence should be addressed to Shihong Chen; csh041230104@nuaa.edu.cn

Received 17 April 2021; Revised 13 June 2021; Accepted 29 June 2021; Published 9 July 2021

Academic Editor: Junpeng Shi

Joint angle and frequency estimation, one of the key technologies in wireless communication and radar science, has been extensively studied by scholars. For linear arrays, this paper proposes a joint angle and frequency estimation method based on covariance reconstruction and the estimation of signal parameters via rotational invariance techniques (CR-ESPRIT). We first use the received conjugate signal to reconstruct a covariance matrix. Then, we use the least squares-ESPRIT (LS-ESPRIT) algorithm to estimate the desired frequencies. Finally, we estimate the angles according to the reconstructed matrix. The proposed method can estimate signal parameters via automatic pairing and without an additional parameter pairing process under the condition of a uniform or a nonuniform array. Moreover, this method has high estimation accuracy, excellent and stable anti-noise performance, and strong algorithmic robustness. Through a computer simulation analysis, we can confirm the reliability and validity of the proposed parameter estimation method. A comparison with other methods further proves the performance advantages of the developed method. The method in this paper can be easily applied to many signal processing contexts, such as electronic reconnaissance and wireless communication.

1. Introduction

The joint angle and frequency estimation of received signals submerged in Gaussian white noise has important applications in wireless communication [1], audio and speech signal processing [2], and other fields [3, 4]. For example, in a wireless communication system, accurate and robust joint angle and frequency estimation can help provide better channel information, thereby improving the link quality and anti-interference ability of the system [1]. Especially in electronic reconnaissance [5–8], we often use the operating frequencies and directions of arrival (DOAs) [9–13] of noncooperative radar radiation source signals to describe the main parameters of radar signal characteristics [14–16]. Therefore, to effectively obtain the parameters of noncooperative radar source signals, it is necessary to study a joint DOA and frequency estimation method for such signals submerged in Gaussian white noise.

Regarding the joint DOA and frequency estimation of noisy signals, researchers worldwide have proposed various methods [16–22]. In 1986, Schmidt [17] proposed the multiple signal classification (MUSIC) algorithm for parameter estimation. Although the algorithm has good estimation performance, it has high computational complexity since it needs to search for spectral peaks to obtain the estimated values. Lemma et al. [18] presented a joint angle and frequency estimation method based on the multidimensional estimation of signal parameters via rotational invariance techniques (ESPRIT). Nevertheless, this algorithm has low parameter estimation accuracy under low signal-to-noise ratios (SNRs). To effectively improve the accuracy of estimated DOA and frequency results, in 2010, Wang proposed a joint angle and frequency estimation technique using multiple-delay outputs (MDJAFE) [16] based on the ESPRIT algorithm. However, this method cannot realize automatic parameter pairing when performing the joint estimation of signal parameters. Since the propagator method (PM) shows good performance in parameter estimation, it has attracted the attention of scholars. Sun et al. [19] proposed a joint DOA and frequency estimation based on the improved PM. Although the complexity of the algorithm is low and it can realize the automatic pairing of DOA and frequency parameter estimations, its parameter estimation accuracy is not high. Wang et al. [20] proposed an improved ESPRIT algorithm using the multidelay output of a uniform linear antenna (ULA). Although the algorithm's complexity is greatly reduced, this method is greatly affected by noise, and the estimation accuracy of this method is still very limited when the SNR is low. Based on the extended orthogonal matching pursuit (EOMP) algorithm, Gao et al. [21] proposed an approach to jointly estimate DOAs and frequency, whereas this method has high computational complexity. Xu et al. [22] proposed a joint DOA and narrowband source carrier frequency estimation method based on parallel factor (PARAFAC) analysis. The computational complexity of this method is relatively high, and the hardware cost is also high.

Due to the wide range of possible SNRs, frequency and DOA estimation algorithms have unstable anti-noise performance and limited estimation accuracy. We propose a method for the joint DOA and frequency estimation of signals submerged in Gaussian white noise. The algorithm involves a three-step estimation procedure. First, we preprocess the received signal. Second, we use the least squares-ESPRIT (LS-ESPRIT) algorithm to estimate the frequency parameters of the signal. Finally, according to the unique relationship between the signal angle and its frequency, we estimate the DOAs. Computer simulations and comparisons with other methods prove the excellent performance of the proposed method.

The main contributions of our work can be summarized as follows:

(1) We improve upon the estimation process in [20]. Under the condition of a uniform or a nonuniform array, the method proposed in this paper can estimate the required parameters by performing automatic pairing without an additional parameter pairing process. Moreover, this method has good estimation accuracy, stable anti-noise performance, and robustness. Therefore, the method proposed in this paper is more suitable than other approaches for the parameter estimation of noncooperative radar radiation sources in an external field, which usually contains a complex electromagnetic environment.

(2) This paper proposes a joint angle and frequency estimation method based on covariance reconstruction and ESPRIT (CR-ESPRIT). Within the SNR range from -15 dB to 15 dB (step: 2 dB), its performance is better than that of the PM, the covariance reconstruction and propagator method (CR-PM), the ESPRIT method [16], and the improved ESPRIT method [20].

The remainder of this paper is structured as follows. The materials and methods are presented in Section 2; Section 3 contains the results and a discussion, and Section 4 is the summary of the paper.

Notations. $(\bullet)^H$, $(\bullet)^*$, $(\bullet)^{-1}$, and $(\bullet)^+$ denote the conjugate transpose, complex conjugation, inverse, and Moore–Penrose inverse (pseudoinverse) operations, respectively. Matrices and vectors are represented by boldfaced capital letters and lowercase letters, respectively.

2. Materials and Methods

2.1. Signal Model. Consider an antenna array that consists of M array elements arranged in a straight line at equal distances, where the distance between each pair of array elements is d [23]. We suppose that there exist K $(K < M)$ far-field source narrowband signals (the center frequency is f_k), which are incident on the antenna array. Therefore, we can regard the signals as plane waves when they reach the array. Then, we can express the received signal of the mth antenna as follows [24]:

$$y_m(t) = \sum_{k=1}^{K} \exp\left(-j2\pi(m-1)\mathrm{d}f_k\left(\frac{\sin(\theta_k)}{c}\right)\right)s_k(t) + n_m(t), \quad m = 1, 2, \ldots, M, \tag{1}$$

where $s_k(t)$ is the kth incident far-field source signal, c is the speed of light (m/s), θ_k and f_k are the DOA and frequency of the kth signal, respectively, and $n_m(t)$ is the zero-mean additive white Gaussian noise on the mth antenna. We can express the output signal of the linear array as

$$\mathbf{Y}_0 = \left[y_1(n)y_2(n), \ldots, y_M(n)\right]^T, \quad n = 1, 2, \ldots, N. \tag{2}$$

We assume that the signal is uniformly sampled by a period that conforms to the Nyquist sampling rate and that the number of snapshots is N. Therefore, we can transform the signal model studied in this paper into a joint DOA and frequency estimation model for multiple source signals, where N sampling points are obtained for each source signal.

We assume that the number of signal sources K is known; thus, we can rewrite output state vector (2) in the following matrix form:

$$\mathbf{Y}_0 = \mathbf{AS} + \mathbf{N}_0, \tag{3}$$

where $\mathbf{S} = [\mathbf{s}_1, \mathbf{s}_2, \ldots, \mathbf{s}_K]^T \in C^{K\times N}$, $\mathbf{N}_0 = [\mathbf{n}_1, \mathbf{n}_2, \ldots, \mathbf{n}_M]^T \in C^{M\times N}$, and

$$\mathbf{A} = \begin{bmatrix} 1 & 1 & \ldots & 1 \\ \exp(-j\alpha_1) & \exp(-j\alpha_2) & \ldots & \exp(-j\alpha_K) \\ \ldots & \ldots & \ldots & \ldots \\ \exp(-j(M-1)\alpha_1) & \exp(-j(M-1)\alpha_2) & \ldots & \exp(-j(M-1)\alpha_K) \end{bmatrix}. \tag{4}$$

In equation (4), $\alpha_k = 2\pi \mathrm{d} f_k \sin(\theta_k)/c$, $k = 1, \ldots, K$. To realize the joint DOA and frequency estimation model, we take (P-1) delays [25, 26] for the signal received from the antenna arrays shown in Figure 1. In addition, we set $0 < (P-1)\tau < 1/\max(f_k)$. Therefore, we can obtain the delay signal with the delay value τ as

$$\begin{aligned} y_m(t-\tau) &= \sum_{k=1}^{K} \exp\left(\frac{-j2\pi(m-1)\mathrm{d} f_k \sin(\theta_k)}{c}\right) s_k(t-\tau) + n_m'(t) \\ &= \sum_{k=1}^{K} \exp\left(\frac{-j2\pi(m-1)\mathrm{d} f_k \sin(\theta_k)}{c}\right) s_k(t)\exp(-j2\pi f_k \tau) + n_m'(t). \end{aligned} \tag{5}$$

We can transform equation (5) into the following form:

$$\mathbf{Y}_1 = \mathbf{A}\mathbf{\Phi}\mathbf{S} + \mathbf{N}_1, \tag{6}$$

where $\beta_k = 2\pi f_k \tau$, $(k = 1, 2, \ldots, K)$ and $\mathbf{\Phi} = \mathrm{diag}[\exp(-j\beta_1), \exp(-j\beta_2), \ldots, \exp(-j\beta_K)]$.

When the delay value is $p\tau$, we can express the delay signal as

$$\begin{aligned} y_m(t-p\tau) &= \sum_{k=1}^{K} \exp\left(\frac{-j2\pi(m-1)\mathrm{d} f_k \sin(\theta_k)}{c}\right) s_k(t-p\tau) + n_m'(t) \\ &= \sum_{k=1}^{K} \exp\left(\frac{-j2\pi(m-1)\mathrm{d} f_k \sin(\theta_k)}{c}\right) s_k(t)\exp(-j2\pi f_k \tau p) + n_m'(t). \end{aligned} \tag{7}$$

Then, we can also express equation (7) as

$$\mathbf{Y}_p = \mathbf{A}\mathbf{\Phi}^p\mathbf{S} + \mathbf{N}_p, \quad p = 0, 1, 2, \ldots, P-1. \tag{8}$$

After reorganizing the equations, we can obtain the following expression:

$$\mathbf{Y} = \begin{bmatrix} \mathbf{Y}_0 \\ \mathbf{Y}_1 \\ \ldots \\ \mathbf{Y}_{P-1} \end{bmatrix} = \begin{bmatrix} \mathbf{A} \\ \mathbf{A}\mathbf{\Phi} \\ \ldots \\ \mathbf{A}\mathbf{\Phi}^{P-1} \end{bmatrix} \mathbf{S} + \begin{bmatrix} \mathbf{N}_0 \\ \mathbf{N}_1 \\ \ldots \\ \mathbf{N}_{P-1} \end{bmatrix}. \tag{9}$$

2.2. The Proposed Method. In this paper, inspired by the improved ESPRIT method [20], we propose a joint angle and frequency estimation method based on CR-ESPRIT. In a real space, the improved ESPRIT method is not suitable for complex electromagnetic environments. Due to the noncooperative characteristics of radiation sources, we generally believe that there is no prior information available regarding the parameters. Moreover, in a complex and harsh electromagnetic environment, the detected radiation source signals are very weak. Therefore, in a situation with a low SNR, the developed method not only needs to distinguish useful signals and noise effectively but also needs to have good estimation performance, noise immunity and robustness. Additionally, it also needs to have the ability to automatically pair the relevant parameters without an additional parameter pairing process under the condition of a uniform or a nonuniform array.

We first preprocess the received signal in Section 2.2.1. Second, we use the LS-ESPRIT algorithm to estimate the frequency parameters of the received signal in Section 2.2.2. Third, according to the relationship between the DOA and frequency in the signal model, we reconstruct the received signal, and then we estimate the DOAs in Section 2.2.3. In

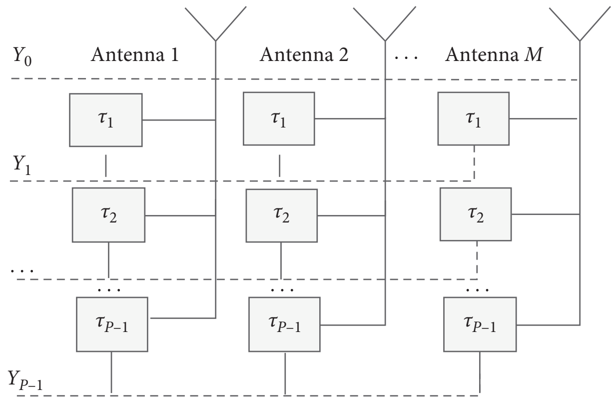

FIGURE 1: Received signals with multilevel delays.

Section 2.2.4, we provide the detailed steps of the proposed method. Finally, we provide the detailed steps of the proposed method under the condition of a nonuniform array in Section 2.2.5.

2.2.1. The Preprocessing Procedure. First, we obtain the covariance matrix $\mathbf{R}_Y = \mathbf{Y}\mathbf{Y}^H$ of the received signal. To make full use of the conjugate information contained in the received signal, we define the permutation matrix $\mathbf{J}$ [27]:

$$\mathbf{J} = \begin{bmatrix} 0 & \dots & 0 & 1 \\ \dots & 0 & 1 & 0 \\ 0 & \dots & \dots & \dots \\ 1 & 0 & \dots & 0 \end{bmatrix}_{PM\times PM}. \tag{10}$$

Therefore, we can construct the following matrix:

$$\mathbf{R}_J = \mathbf{J}(\mathbf{Y}^*)(\mathbf{Y}^*)^H\mathbf{J}^H. \tag{11}$$

We add the covariance matrix $\mathbf{R}_Y$ and $\mathbf{R}_J$ from equation (11), and then we average them. The form of the obtained covariance matrix is shown as follows:

$$\mathbf{R} = \frac{\mathbf{R}_Y + \mathbf{R}_J}{2}. \tag{12}$$

Through analysis, we can obtain that the new total covariance matrix $\mathbf{R}$ is a Hermitian matrix (PM × PM) [28]. Therefore, we can apply eigenvalue decomposition, and then we can reconstruct the signal subspace $\mathbf{E}_{ss}$. In a no-noise situation, $\mathbf{E}_{ss}$ can be approximately expressed as

$$\mathbf{E}_{ss} = \begin{bmatrix} \mathbf{A} \\ \mathbf{A\Phi} \\ \dots \\ \mathbf{A\Phi}^{P-1} \end{bmatrix}\mathbf{F}, \tag{13}$$

where $\mathbf{F}$ is a full-rank matrix with $K \times K$ dimensions.

Remark 1. As mentioned earlier, the new total covariance matrix $\mathbf{R}$ is already a Hermitian matrix. According to Hermitian matrix characteristics, we assume that the diagonal matrix of the eigenvalues of $\mathbf{R}$ is $\mathbf{G}$. Then, there exists a unitary matrix $\mathbf{U}$, which assures $\mathbf{RU} = \mathbf{UG}$. Therefore, we can treat $\mathbf{R}$ as the unitary matrix $\mathbf{U}$ by using this correlation feature to further reduce the complexity of the proposed method and then propose a much lower complexity method.

2.2.2. Frequency Estimation. We define the following parameters:

$$\mathbf{E}_1 = \begin{bmatrix} \mathbf{A} \\ \mathbf{A\Phi} \\ \dots \\ \mathbf{A\Phi}^{P-2} \end{bmatrix}\mathbf{F}, \tag{14}$$

$$\mathbf{E}_2 = \begin{bmatrix} \mathbf{A\Phi} \\ \mathbf{A\Phi}^2 \\ \dots \\ \mathbf{A\Phi}^{P-1} \end{bmatrix}\mathbf{F}. \tag{15}$$

Therefore, equations (14) and (15) have the following relationship:

$$\mathbf{E}_2 = \begin{bmatrix} \mathbf{A\Phi} \\ \mathbf{A\Phi}^2 \\ \dots \\ \mathbf{A\Phi}^{P-1} \end{bmatrix}\mathbf{F} = \begin{bmatrix} \mathbf{A} \\ \mathbf{A\Phi}^1 \\ \dots \\ \mathbf{A\Phi}^{P-2} \end{bmatrix}\mathbf{F}\mathbf{F}^{-1}\mathbf{\Phi}\mathbf{F} = \mathbf{E}_1\mathbf{F}^{-1}\mathbf{\Phi}\mathbf{F}. \tag{16}$$

Let $\mathbf{\Psi} = \mathbf{F}^{-1}\mathbf{\Phi}\mathbf{F}$ and $\mathbf{\Psi} = \mathbf{E}_1^{+}\mathbf{E}_2$. According to the LS-ESPRIT algorithm, we can estimate $\mathbf{\Phi}$ by the eigenvalue decomposition of $\mathbf{\Psi}$, and we can also estimate the matrix $\mathbf{F}^{-1}$ by the eigenvector of $\mathbf{\Phi}$. In a no-noise situation, we define

$$\begin{aligned} \widehat{\mathbf{F}}^{-1} &= \mathbf{F}^{-1}\mathbf{\Theta}, \\ \widehat{\mathbf{\Phi}} &= \mathbf{\Theta}^{-1}\mathbf{\Phi}\mathbf{\Theta}, \end{aligned} \tag{17}$$

where $\mathbf{\Theta}$ is a fuzzy column matrix. Since $\mathbf{\Psi}$ and $\mathbf{\Phi}$ have the same eigenvalues, we can obtain the eigenvalues $\lambda_k\,(k = 1, 2, \dots, K)$ from matrix $\mathbf{\Psi}$. As shown in equation (6) $(\beta_k = 2\pi f_k\tau, k = 1, 2, \dots, K)$, it is obvious that we can estimate the frequency parameter $\widehat{f}_k$, $k = 1, 2, \dots, K$:

$$\widehat{f}_k = \frac{1}{2\pi\tau}\,\mathrm{angle}(\lambda_k). \tag{18}$$

2.2.3. DOA Estimation. $\mathbf{A\Phi}^{P-1}$ has the following expression:

$$\mathbf{A\Phi}^{P-1}=\begin{bmatrix}\exp(-j(P-1)\beta_1) & \exp(-j(P-1)\beta_2) & \cdots & \exp(-j(P-1)\beta_K)\\ \exp(-j\alpha_1)\exp(-j(P-1)\beta_1) & \exp(-j\alpha_2)\exp(-j(P-1)\beta_2) & \cdots & \exp(-j\alpha_K)\exp(-j(P-1)\beta_K)\\ \cdots & \cdots & \cdots & \cdots\\ \exp(-j(M-1)\alpha_1)\exp(-j(P-1)\beta_1) & \exp(-j(M-1)\alpha_2)\exp(-j(P-1)\beta_2) & \cdots & \exp(-j(M-1)\alpha_K)\exp(-j(P-1)\beta_K)\end{bmatrix}. \tag{19}$$

According to the above estimation $\widehat{\mathbf{F}}^{-1}$, we can define the following expression by reconstructing equation (13):

$$\mathbf{E}_Q=\begin{bmatrix}\mathbf{B}\\ \mathbf{B}\mathrm{T}\\ \cdots\\ \mathbf{B}\mathbf{T}^{M-1}\end{bmatrix}\mathbf{\Theta}, \tag{20}$$

where

$$\mathbf{B}=\begin{bmatrix}1 & 1 & \cdots & 1\\ \exp(-j\beta_1) & \exp(-j\beta_2) & \cdots & \exp(-j\beta_K)\\ \cdots & \cdots & \cdots & \cdots\\ \exp(-j(P-1)\beta_1) & \exp(-j(P-1)\beta_2) & \cdots & \exp(-j(P-1)\beta_K)\end{bmatrix},$$

$$\mathrm{T}=\mathrm{diag}\left[\exp(-j\alpha_1),\ \exp(-j\alpha_2),\ldots,\ \exp(-j\alpha_K)\right]\in C^{K\times K},$$

$$\alpha_k=\frac{2\pi \mathrm{d} f_k\sin(\theta_k)}{c},\quad k=1,2,\ldots,K. \tag{21}$$

According to reconstructed equation (20), we can use the method described below to estimate the DOA.

We define the following matrices:

$$\mathbf{E}_{Q1}=\begin{bmatrix}\mathbf{B}\\ \mathbf{B}\mathrm{T}\\ \cdots\\ \mathbf{B}\mathbf{T}^{M-2}\end{bmatrix}\mathbf{\Theta},$$

$$\mathbf{E}_{Q2}=\begin{bmatrix}\mathbf{B}\mathbf{T}\\ \mathbf{B}\mathbf{T}^{2}\\ \cdots\\ \mathbf{B}\mathbf{T}^{M-1}\end{bmatrix}\mathbf{\Theta}. \tag{22}$$

We can also define a matrix $\mathbf{D}$ since $\mathbf{D}=\mathbf{E}_{Q1}^{+}\mathbf{E}_{Q2}$. Then, according to the definitions of $\mathbf{E}_{Q1}$ and $\mathbf{E}_{Q2}$, we can express $\mathbf{D}$ in a no-noise situation:

$$\mathbf{D}=\mathbf{\Theta}^{-1}\mathbf{T}\mathbf{\Theta}. \tag{23}$$

Therefore, we can take the diagonal elements of $\mathbf{D}$, and then, we can obtain $\varpi_k\,(k=1,2,\ldots,K)$, where $\alpha_k=2\pi \mathrm{d} f_k\sin(\theta_k)/c((k=1,2,\ldots,K)$, to obtain the estimation of the DOA:

$$\widehat{\theta}_k=\arcsin\left(\frac{c}{2\pi\widehat{f}_k d}\,\mathrm{angle}(\varpi_k)\right),\quad k=1,2,\ldots,K. \tag{24}$$

2.2.4. The Steps of the Proposed Method. Thus far, we have given the complete process for automatically pairing DOA and frequency estimations in a linear array. The main steps required to implement the method proposed in this paper are as follows:

(i) Step 1: according to permutation matrix $\mathbf{J}$ and equation (12), we reconstruct the covariance matrix $\mathbf{R}$.

(ii) Step 2: we apply eigenvalue decomposition to $\mathbf{R}$, and then we reconstruct the signal subspace $\mathbf{E}_{ss}$. According to equations (14) and (15), we construct matrices $\mathbf{E}_1$ and $\mathbf{E}_2$, respectively.

(iii) Step 3: we use equation ($\mathbf{\Psi}=\mathbf{E}_1^{+}\mathbf{E}_2$) for eigenvalue decomposition to obtain $\mathbf{F}^{-1}$ and $\widehat{\mathbf{\Phi}}$. Finally, we estimate the frequency parameter $\widehat{f}_k$ according to equation (18).

(iv) Step 4: we can obtain matrix $\mathbf{E}_Q$ according to the reconstruction of $\mathbf{E}_{ss}$ in equation (13). Then, we can also construct matrices $\mathbf{E}_{Q1}$ and $\mathbf{E}_{Q2}$.

(v) Step 5: we calculate $\mathbf{D} = \mathbf{E}_{Q1}^{+}\mathbf{E}_{Q2}$ to obtain matrix **D.** Finally, we estimate the DOA parameter $\widehat{\theta}_k$ according to equation (24).

2.2.5. The Condition of a Nonuniform Array. In this section, we first present the method proposed in this paper when the distances between the array elements are not equal. Then, we present the main steps for implementing the method in the case of a nonuniform array.

We assume that the first element $d_1 = 0$ and that the distance between the mth element and the first element is d_m. Then, we can transform equation (4) into the following form:

$$\mathbf{A}_1 = \begin{bmatrix} 1 & 1 & \cdots & 1 \\ \exp(-jd_2\eta_1) & \exp(-jd_2\eta_2) & \cdots & \exp(-jd_2\eta_K) \\ \cdots & \cdots & \cdots & \cdots \\ \exp(-jd_M\eta_1) & \exp(-jd_M\eta_2) & \cdots & \exp(-jd_M\eta_K) \end{bmatrix}, \tag{25}$$

where $\eta_k = 2\pi f_k \sin(\theta_k)/c\,(k = 1, 2, \ldots, K)$. At the same time, equation (19) undergoes the following transformation:

$$\mathbf{A}_1\mathbf{\Phi}^{P-1} = \begin{bmatrix} \exp(-j(P-1)\beta_1) & \exp(-j(P-1)\beta_2) & \cdots & \exp(-j(P-1)\beta_K) \\ \exp(-jd_2\eta_1)\exp(-j(P-1)\beta_1) & \exp(-jd_2\eta_2)\exp(-j(P-1)\beta_2) & \cdots & \exp(-jd_2\eta_K)\exp(-j(P-1)\beta_K) \\ \cdots & \cdots & \cdots & \cdots \\ \exp(-jd_M\eta_1)\exp(-j(P-1)\beta_1) & \exp(-jd_M\eta_2)\exp(-j(P-1)\beta_2) & \cdots & \exp(-jd_M\eta_K)\exp(-j(P-1)\beta_K) \end{bmatrix}. \tag{26}$$

Similarly, we can reconstruct equation (13) and define the following expression:

$$\mathbf{E}_{QQ} = \begin{bmatrix} \mathbf{BJ}_1 \\ \mathbf{BJ}_2 \\ \cdots \\ \mathbf{BJ}_M \end{bmatrix}\mathbf{\Theta}, \tag{27}$$

where $\mathbf{J}_m = \mathrm{diag}[\exp(-jd_m\eta_1), \exp(-jd_m\eta_2), \ldots, \exp(-jd_m\eta_K)] \in C^{K\times K}$, $m = 1, 2, \ldots, M$.

We define the following matrix:

$$\begin{aligned} \mathbf{E}_{QQ1} &= \begin{bmatrix} \mathbf{BJ}_1 \\ \mathbf{BJ}_2 \\ \cdots \\ \mathbf{BJ}_{M-1} \end{bmatrix}\mathbf{\Theta} = \begin{bmatrix} \mathbf{E}_{QQ11} \\ \mathbf{E}_{QQ12} \\ \cdots \\ \mathbf{E}_{QQ1(M-1)} \end{bmatrix}, \\ \mathbf{E}_{QQ2} &= \begin{bmatrix} \mathbf{BJ}_2 \\ \mathbf{BJ}_3 \\ \cdots \\ \mathbf{BJ}_M \end{bmatrix}\mathbf{\Theta} = \begin{bmatrix} \mathbf{E}_{QQ22} \\ \mathbf{E}_{QQ23} \\ \cdots \\ \mathbf{E}_{QQ2M} \end{bmatrix}. \end{aligned} \tag{28}$$

We also define the matrix $\mathbf{Q}_m$, where $\mathbf{Q}_m = (\mathbf{E}_{QQ1(m-1)})^{+}(\mathbf{E}_{QQ2m})$, $m = 2, \ldots, M$. Therefore, we can take the diagonal elements of $\mathbf{Q}_m$ and then obtain

$$\mathbf{v}_m = \mathrm{diag}[\exp(-j(d_m - d_{m-1})\eta_1), \exp(-j(d_m - d_{m-1})\eta_2), \ldots, \exp(-j(d_m - d_{m-1})\eta_K)] \in C^{K\times K}, \quad m = 2, \ldots, M. \tag{29}$$

We sort the diagonal elements and then define the following matrix:

$$\mathbf{V} = \begin{bmatrix} 1 & 1 & \cdots & 1 \\ \exp(-j(d_2 - d_1)\eta_1) & \exp(-j(d_2 - d_1)\eta_2) & \cdots & \exp(-j(d_2 - d_1)\eta_K) \\ \cdots & \cdots & \cdots & \cdots \\ \exp(-j(d_m - d_{m-1})\eta_1) & \exp(-j(d_m - d_{m-1})\eta_2) & \cdots & \exp(-j(d_m - d_{m-1})\eta_K) \end{bmatrix}. \tag{30}$$

According to equation (30), we can obtain the estimation of the DOA:

$$\widehat{\theta}_k = \frac{1}{M-1}\sum_{m=2}^{M}\arcsin\left(\frac{c}{2\pi\widehat{f}_k(d_m-d_{m-1})}\text{angle}(\mathbf{V}_{mk})\right),\quad (k=1,2,\ldots,K). \tag{31}$$

The main steps for implementing the method in this paper under the condition of a nonuniform array are as follows:

(i) Step 1: according to equations (10), (12), and (25), we reconstruct the new covariance matrix.

(ii) Step 2: we apply eigenvalue decomposition to the new covariance matrix, and then we reconstruct the signal subspace $\mathbf{E}_{ss}$. According to equations (14) and (15), we construct matrices $\mathbf{E}_1$ and $\mathbf{E}_2$, respectively.

(iii) Step 3: we use equation ($\mathbf{\Psi} = \mathbf{E}_1^{+}\mathbf{E}_2$) to perform eigenvalue decomposition and obtain $\mathbf{F}^{-1}$ and $\widehat{\mathbf{\Phi}}$. Finally, we estimate the frequency parameter $\widehat{f}_k$ according to equation (18).

(iv) Step 4: we can obtain the matrix $\mathbf{E}_{QQ}$ according to equation (27). Then, we can also construct matrices $\mathbf{E}_{QQ1}$ and $\mathbf{E}_{QQ2}$.

(v) Step 5: we can obtain matrix $\mathbf{V}$ according to equation (30). Finally, we estimate the DOA parameter $\widehat{\theta}_k$ according to equation (31).

3. Results and Discussion

3.1. Performance Analysis of the Proposed Method

3.1.1. Method Complexity. In this section, we focus on the performance analysis with respect to complexity. Complexity is mainly measured by the number of complex multiplications and the running time required by a given method. For the ESPRIT method in [16], the complexity is $O(M^2P^2N + M^3P^3 + 2K^2M(P-1) + 8K^3 + 2K^2(M-1))$. For the improved ESPRIT method in [20], the complexity required to calculate the covariance matrix $\mathbf{R}_Y$ is $O(M^2P^2N)$. The complexity required for eigenvalue decomposition is $O(M^3P^3)$. The complexity of calculating $\mathbf{\Psi} = \mathbf{E}_1^{+}\mathbf{E}_2$ is $O(2K^2M(P-1) + 2K^3)$. Then, the eigenvalue decomposition complexity of $\mathbf{\Psi} = \mathbf{E}_1^{+}\mathbf{E}_2$ is $O(K^3)$. When estimating the DOA, the complexity is $O(2K^3 + 2K^2(M-1)P)$. Therefore, the complexity of the improved ESPRIT method is $O(M^2P^2N + M^3P^3 + 2K^2M(P-1) + 5K^3 + 2K^2(M-1)P)$.

For the proposed method, the preprocessing complexity is $O(M^2P^2N + M^3P^3)$. The complexity of frequency estimation is $O(2K^2M(P-1) + 3K^3)$. In addition, the complexity of DOA estimation is $O(2K^3 + 2K^2(M-1)P)$. Therefore, the complexity of the proposed method is $O(M^2P^2N + M^3P^3 + 2K^2M(P-1)$ $+5K^3 + 2K^2(M-1)P + 1)$. It should be noted that in the preprocessing of this paper, we only need to calculate the covariance matrix $\mathbf{R}_Y$ and the eigenvalue decomposition, which means that we do not require additional calculations to construct the matrix $\mathbf{R}_J$.

The reason is that, according to equation (11), $\mathbf{R}_J$ has the following expression:

$$\begin{aligned}
\mathbf{R}_J = \mathbf{J}\mathbf{Y}^*\mathbf{Y}^{*H}\mathbf{J}^H &= \begin{bmatrix} 0 & \cdots & 0 & 1\\ \cdots & 0 & 1 & 0\\ 0 & \cdots & \cdots & \cdots\\ 1 & 0 & \cdots & 0\end{bmatrix}\begin{bmatrix}\mathbf{Y}_0\\ \mathbf{Y}_1\\ \cdots\\ \mathbf{Y}_{P-1}\end{bmatrix}^*\begin{bmatrix}\mathbf{Y}_0\\ \mathbf{Y}_1\\ \cdots\\ \mathbf{Y}_{P-1}\end{bmatrix}^{*H}\begin{bmatrix} 0 & \cdots & 0 & 1\\ \cdots & 0 & 1 & 0\\ 0 & \cdots & \cdots & \cdots\\ 1 & 0 & \cdots & 0\end{bmatrix} = \begin{bmatrix}\mathbf{Y}_{P-1}^*\\ \cdots\\ \mathbf{Y}_1^*\\ \mathbf{Y}_0^*\end{bmatrix}\begin{bmatrix}\mathbf{Y}_0 & \mathbf{Y}_1 & \cdots & \mathbf{Y}_{P-1}\end{bmatrix}\begin{bmatrix} 0 & \cdots & 0 & 1\\ \cdots & 0 & 1 & 0\\ 0 & \cdots & \cdots & \cdots\\ 1 & 0 & \cdots & 0\end{bmatrix},\\
&= \begin{bmatrix}\mathbf{Y}_{P-1}^*\mathbf{Y}_0 & \mathbf{Y}_{P-1}^*\mathbf{Y}_1 & \cdots & \mathbf{Y}_{P-1}^*\mathbf{Y}_{P-1}\\ \cdots & \cdots & \cdots & \cdots\\ \mathbf{Y}_1^*\mathbf{Y}_0 & \mathbf{Y}_1^*\mathbf{Y}_1 & \cdots & \mathbf{Y}_1^*\mathbf{Y}_{P-1}\\ \mathbf{Y}_0^*\mathbf{Y}_0 & \mathbf{Y}_0^*\mathbf{Y}_1 & \cdots\cdots & \mathbf{Y}_0^*\mathbf{Y}_{P-1}\end{bmatrix}\begin{bmatrix} 0 & \cdots & 0 & 1\\ \cdots & 0 & 1 & 0\\ 0 & \cdots & \cdots & \cdots\\ 1 & 0 & \cdots & 0\end{bmatrix} = \begin{bmatrix}\mathbf{Y}_{P-1}^*\mathbf{Y}_{P-1} & \cdots & \mathbf{Y}_{P-1}^*\mathbf{Y}_1 & \mathbf{Y}_{P-1}^*\mathbf{Y}_0\\ \cdots & \cdots & \cdots & \cdots\\ \mathbf{Y}_1^*\mathbf{Y}_{P-1} & \cdots & \mathbf{Y}_1^*\mathbf{Y}_1 & \mathbf{Y}_1^*\mathbf{Y}_0\\ \mathbf{Y}_0^*\mathbf{Y}_{P-1} & \cdots & \mathbf{Y}_0^*\mathbf{Y}_1 & \mathbf{Y}_0^*\mathbf{Y}_0\end{bmatrix},
\end{aligned} \tag{32}$$

while the covariance matrix $\mathbf{R}_Y$

$$\mathbf{R}_Y = \mathbf{Y}\mathbf{Y}^H = \begin{bmatrix}\mathbf{Y}_0\\ \mathbf{Y}_1\\ \cdots\\ \mathbf{Y}_{P-1}\end{bmatrix}\begin{bmatrix}\mathbf{Y}_0\\ \mathbf{Y}_1\\ \cdots\\ \mathbf{Y}_{P-1}\end{bmatrix}^H = \begin{bmatrix}\mathbf{Y}_0\\ \mathbf{Y}_1\\ \cdots\\ \mathbf{Y}_{P-1}\end{bmatrix}\begin{bmatrix}\mathbf{Y}_0^* & \mathbf{Y}_1^* & \cdots & \mathbf{Y}_{P-1}^*\end{bmatrix} = \begin{bmatrix}\mathbf{Y}_0\mathbf{Y}_0^* & \mathbf{Y}_0\mathbf{Y}_1^* & \cdots & \mathbf{Y}_0\mathbf{Y}_{P-1}^*\\ \mathbf{Y}_1\mathbf{Y}_0^* & \mathbf{Y}_1\mathbf{Y}_1^* & \cdots & \mathbf{Y}_1\mathbf{Y}_{P-1}^*\\ & \cdots & \cdots & \cdots\\ \mathbf{Y}_{P-1}\mathbf{Y}_0^* & \mathbf{Y}_{P-1}\mathbf{Y}_1^* & \cdots & \mathbf{Y}_{P-1}\mathbf{Y}_{P-1}^*\end{bmatrix}. \tag{33}$$

By observing equations (32) and (33), we find that through simple moment transformation, we can transform the matrix $\mathbf{R}_Y$ into the matrix $\mathbf{R}_J$. Therefore, when preprocessing, we do not need additional complex multiplications to reconstruct the matrix $\mathbf{R}_J$.

For the PM, the complexity of frequency estimation is $O(M^2P^2N + 4K^3 + M^2P^2K + PMK^2 + 2K^2(M-K))$. In addition, the complexity of DOA estimation is $O(K^2(M-K) + 2K^3 + 2K^2(M-1))$. Therefore, the complexity of the PM is $O(M^2P^2N + 6K^3 + M^2P^2K + PMK^2 + 3K^2(M-K) + 2K^2(M-1))$. The CR method is also applicable to the PM. Therefore, the complexity of the CR-PM is $O(M^2P^2N + 6K^3 + M^2P^2K + PMK^2 + 3K^2(M-K) + 2K^2(M-1))$.

Figures 2 and 3 present the complexity comparison of these algorithms versus the number of signal sources K and the number of snapshots N with $M = 12$ and $P = 3$, respectively. Table 1 compares the running time of these algorithms under the condition of an i7-8550U CPU with $K = 3$, $N = 200$, and 2000 Monte Carlo simulations. Figures 2 and 3 show that the complexity of the method proposed in this paper is almost the same as that of the ESPRIT method in [16] and that of the improved ESPRIT method in [20] and is much higher than that of the PM and that of the CR-PM. In addition, the running time of the proposed method does not increase much. Moreover, through subsequent analysis, within the SNR range from −15 dB to −1 dB, the advantages of the proposed method are more obvious. In particular, when SNR = −15 dB, compared with the improved ESPRIT method, the frequency estimation accuracy of the method proposed in this paper is an approximately 25.50% improvement; the DOA estimation accuracy of the method proposed in this paper is an approximately 31.95% improvement. Therefore, we can confirm that by increasing the utilization of the originally received data, we can improve the parameter estimation accuracy and the noise robustness of the proposed method.

3.1.2. *The Advantages of the Proposed Method.*

In this section, we summarize the advantages of the proposed method in this paper as follows:

(1) Under the condition of a uniform or a nonuniform array, the method can effectively estimate the DOAs and frequencies of source signals. It can also realize automatic pairing without an additional parameter pairing process since the method has the same fuzzy column matrix for both parameters.

(2) For incoherent signal sources whose angles are close together, this method can perform effective identification and parameter estimation.

(3) Compared with those of the PM, the CR-PM, the ESPRIT method [16], and the improved ESPRIT method [20], the frequency and DOA estimation accuracies of the proposed method are greatly improved, and this method has superior estimation performance. Moreover, the proposed method has better anti-noise performance and stronger robustness.

3.2. *Numerical Simulation.*

In the simulation, we assume that the array receives signals emitted by K incoherent far-field sources. We also use the root mean square error (RMSE) metric to evaluate the DOA and frequency estimation performances of the proposed method; we define the RMSEs as

$$
\begin{aligned}
\mathrm{RMSE}_{\mathrm{DOA}} &= \frac{1}{K}\sum_{k=1}^{K}\sqrt{\frac{1}{L}\sum_{l}^{L}\left(\widehat{\theta}_{k,l}-\theta_k\right)^2},\\
\mathrm{RMSE}_{\mathrm{frequency}} &= \frac{1}{K}\sum_{k=1}^{K}\sqrt{\frac{1}{L}\sum_{l}^{L}\left(\widehat{f}_{k,l}-f_k\right)^2},
\end{aligned}
\tag{34}
$$

where $\widehat{\theta}_{k,l}$ and $\widehat{f}_{k,l}$ are the estimated values of θ_k and f_k, respectively, in the lth Monte Carlo simulation and L is the number of Monte Carlo simulations. In this paper, we set $L = 2000$.

3.2.1. *Performance Analysis of the Proposed Method in a Uniform Array.*

In this section, we assume that the array receives signals emitted by three incoherent far-field sources. The DOAs and operating frequencies of the signals are $(\theta_1, f_1) = (15°, 1\,\mathrm{MHz})$, $(\theta_2, f_2) = (40°, 2.1\,\mathrm{MHz})$, and $(\theta_3, f_3) = (50°, 3.1\,\mathrm{MHz})$. SNR = 0 dB, $M = 12$ is the number of array elements, $P = 3$ is the number of delay values, $d = 50$ denotes the distances between the array elements, and $N = 400$ and $K = 3$ are the numbers of snapshots and signal sources, respectively. The scatter diagram of the joint frequency and DOA estimation of the proposed method in this paper is shown in Figure 4. Figure 4 shows that the proposed method is efficient in estimating the frequency and DOA results for a uniform array.

3.2.2. *Performance Analysis under Different Numbers of Array Elements M.*

We set $d = 50$ m, $K = 3$, $P = 3$, and $N = 400$. We also set different numbers of array elements ($M = 8$, 12, and 16). The SNR range is from −15 dB to 15 dB (step: 2 dB), and the RMSEs of the frequency and DOA estimates of the method proposed in this paper are shown in Figures 5 and 6, respectively.

We can see from Figures 5 and 6 that the method proposed in this paper can achieve high estimation performance within the SNR range of −15 dB to 15 dB (step: 2 dB) under different numbers of array elements. The estimation performance is stable under the condition of a low SNR. Moreover, we can see that the SNR has a great impact on the estimation accuracies of the frequency and DOA. The higher the SNR is, the higher the parameter estimation accuracies of the method for these two parameters. With the increase in the number of array elements, the DOA and frequency estimation accuracies of the method proposed in this paper improve. Furthermore, the RMSEs of the proposed method are greatly reduced. This is because as the number of array elements increases, the space diversity gain increases [29].

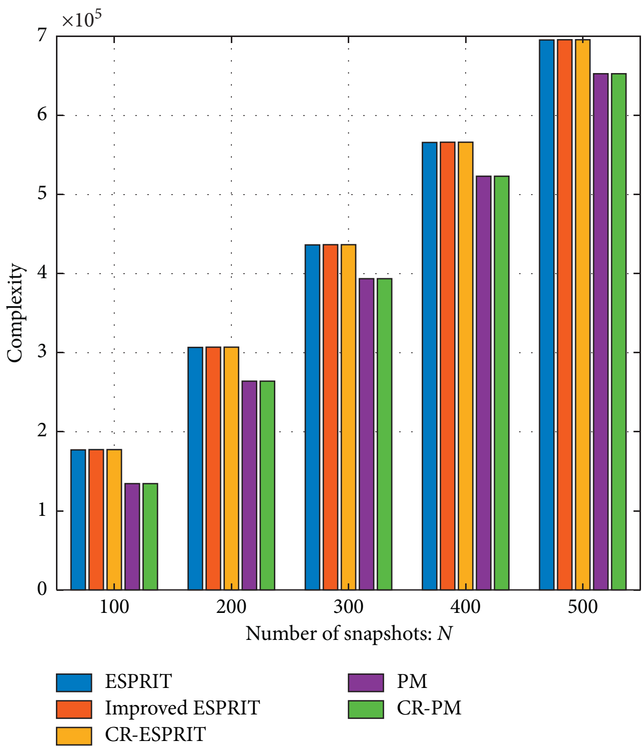

Figure 2: Comparison of algorithm complexity under different snapshots N.

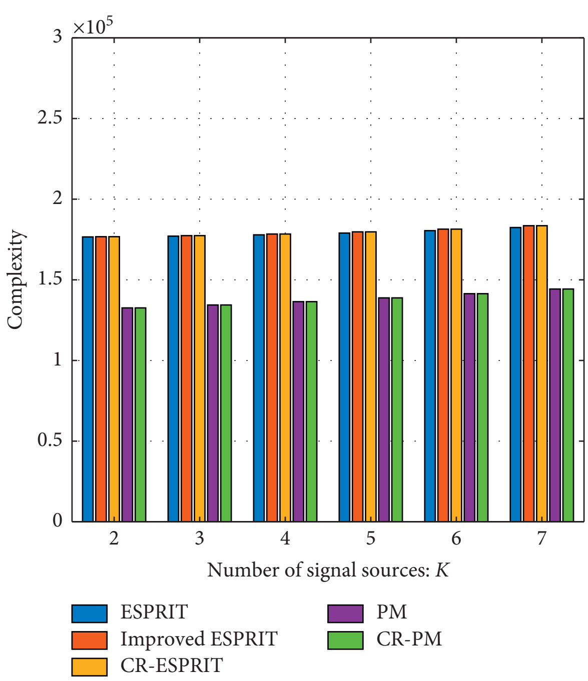

Figure 3: Comparison of algorithm complexity under different signal sources K.

Table 1: Running time of these methods.

Methods	Running time (s)
PM	2.3291
CR-PM	2.6634
ESPRIT	2.8223
Improved ESPRIT	2.8454
CR-ESPRIT	3.1177

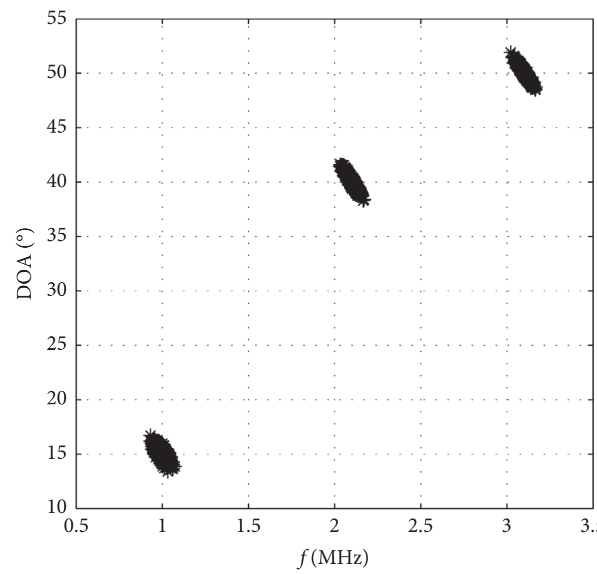

Figure 4: Parameter estimation for a uniform array.

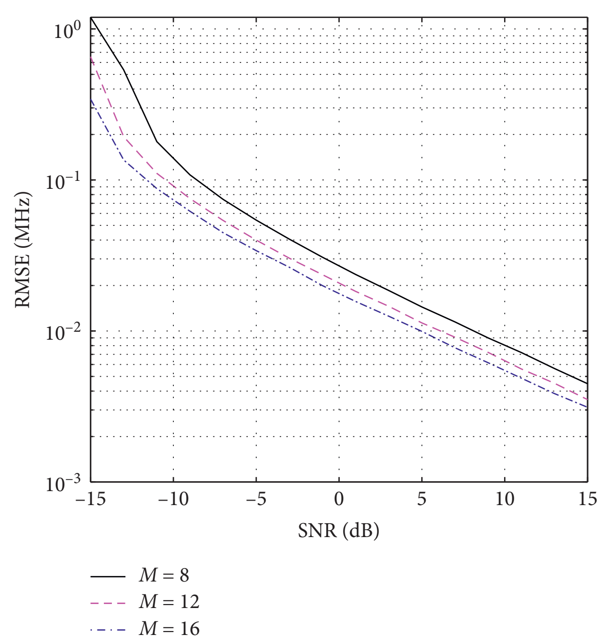

Figure 5: RMSEs of f_k under different numbers of array elements.

3.2.3. Performance Analysis under Different Numbers of Snapshots N. We set $d = 50$ m, $K = 3$, $P = 3$, and $M = 12$. We also set different numbers of snapshots ($N = 100$, 400, and 800). The SNR range is from −15 dB to 15 dB (step: 2 dB), and the RMSEs of the frequency and DOA estimations of the method proposed in this paper are shown in Figure 7 and 8, respectively. We can see from Figure 7 and 8 that when the SNR is within the range of −15 dB to 15 dB (with steps of

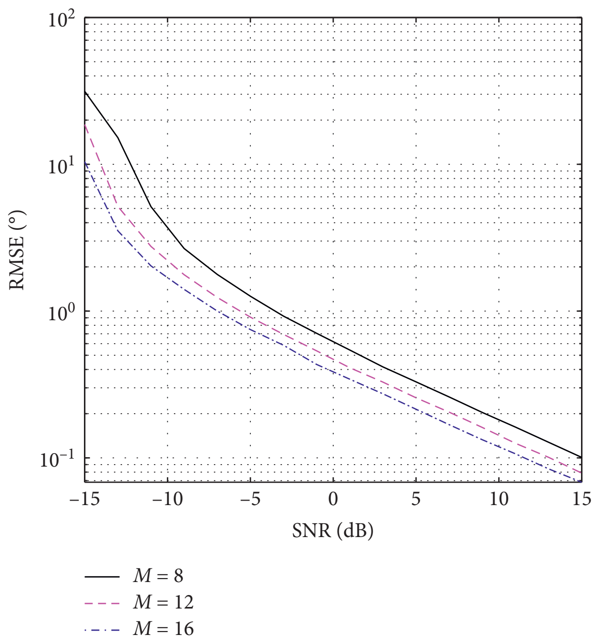

Figure 6: RMSEs of the DOA under different array elements.

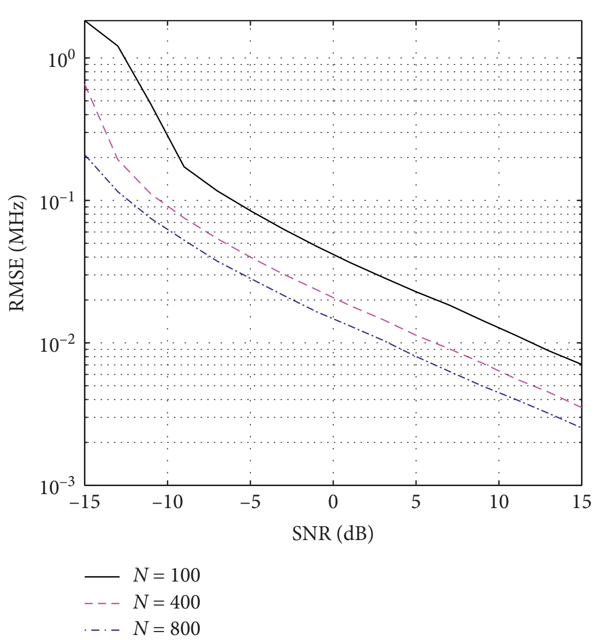

Figure 7: RMSEs of f_k under different numbers of snapshots.

2 dB), the RMSEs of the proposed method demonstrate that with different snapshots, the algorithm can still maintain high estimation performance. Even in a situation with a low SNR, the estimation performance is still stable. As the number of snapshots increases, the estimation accuracy of the method proposed in this paper is enhanced, the performance is more precise, and the RMSEs of the frequency and DOA estimations of the proposed method decrease.

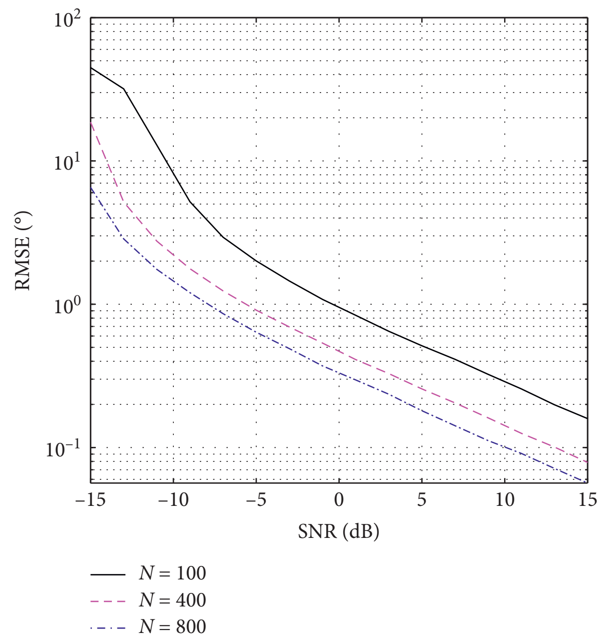

Figure 8: RMSEs of the DOA under different numbers of snapshots.

3.2.4. Performance Analysis under Different Delay Values P. We set $d = 50$ m, $K = 3$, $N = 400$, and $M = 12$. We also set different delay values ($P = 2$, 3, and 4). The range of the SNR is from −15 dB to 15 dB (step: 2 dB), and the RMSEs of the frequency and DOA estimations of the method proposed in this paper are shown in Figures 9 and 10, respectively. In Figures 9 and 10, under different delay values, the proposed method maintains high DOA and frequency estimation performance when the SNR ranges from −15 dB to 15 dB. The estimation performance is stable even in a situation with a low SNR. As the delay value increases, the estimation accuracy of the method proposed in this paper is enhanced, the performance is more precise, and the RMSEs of the DOA and frequency estimations of the method decrease.

3.2.5. Performance Analysis under Different Numbers of Signal Sources K. We set $d = 50$ m, $P = 3$, $N = 400$, and $M = 12$. We also set different numbers of signal sources ($K = 2$, 3, and 4). The range of the SNR is from −15 dB to 15 dB (step: 2 dB), and the RMSEs of the frequency and DOA estimations of the method proposed in this paper are shown in Figures 11 and 12, respectively. In Figures 11 and 12, under different numbers of signal sources, the proposed method maintains high DOA and frequency estimation performance when the SNR ranges from −15 dB to 15 dB. The estimation performance is stable even in a situation with a low SNR. As the number of signal sources increases, the estimation accuracy of the method proposed in this paper makes the performance more imprecise, and the RMSEs of the DOA and frequency estimations of the proposed method increase. As the number of signal sources increases, the

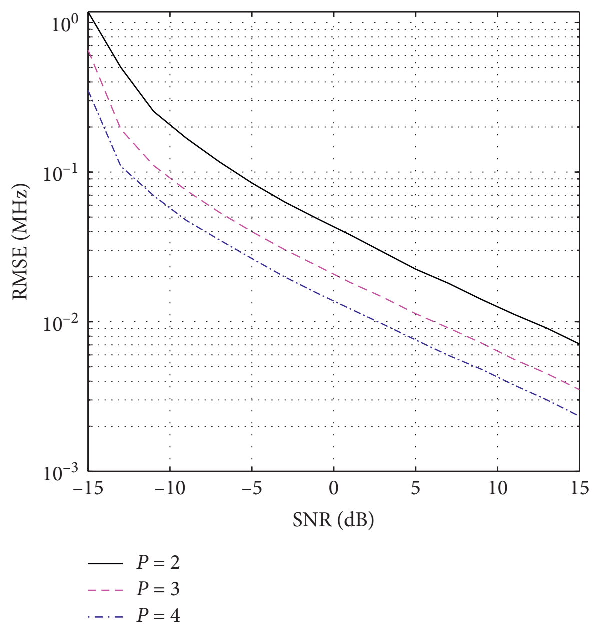

Figure 9: RMSEs of f_k under different delay values.

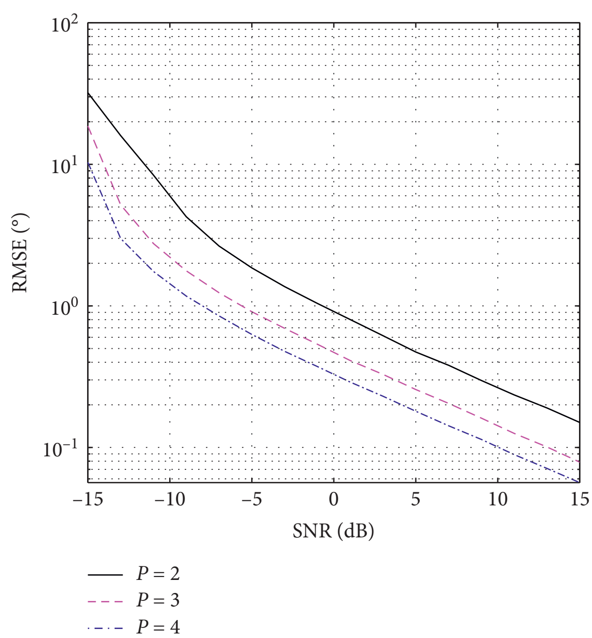

Figure 10: RMSEs of the DOA under different delay values.

interference between sources increases, and the frequency and DOA estimation performances deteriorate [30].

3.2.6. Identification Performance Analysis for Signal Sources with Close Angles. We set $d = 50$ m, $K = 2$, $P = 4$, $N = 200$, and $M = 12$. In this section, we focus on exploring the recognition and identification abilities of the proposed method when the signal sources are at relatively close angles. The DOAs and operating frequencies of the signals are $(\theta_1, f_1) = (15^\circ, 1\,\text{MHz})$ and $(\theta_2, f_2) = (17^\circ, 2.1\,\text{MHz})$. We also set

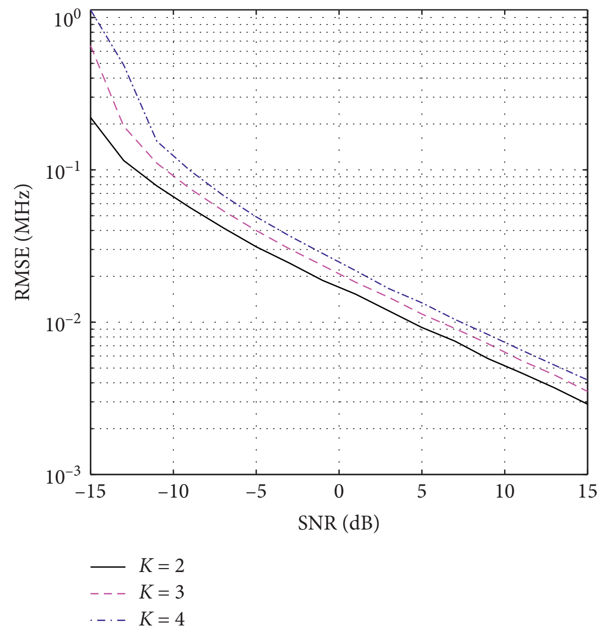

Figure 11: RMSEs of f_k under different numbers of signal sources.

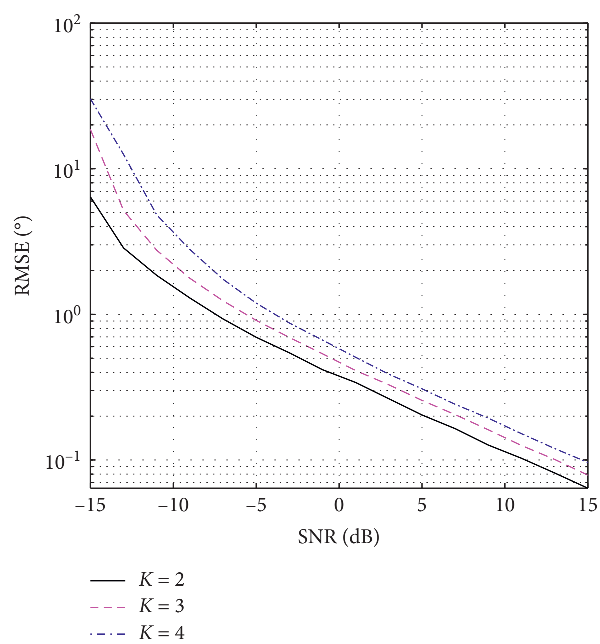

Figure 12: RMSEs of the DOA under different numbers of signal sources.

SNR = 5 dB. As shown in Figure 13, for signal sources with close angles, the proposed method can also perform effective identification and parameter estimation.

3.2.7. Performance Analysis of the Proposed Method in a Nonuniform Array. In an actual field receiving system, the assumed reception model is different from the true model even after a calibration procedure [31]. Therefore, in this section, we mainly discuss the performance analysis under

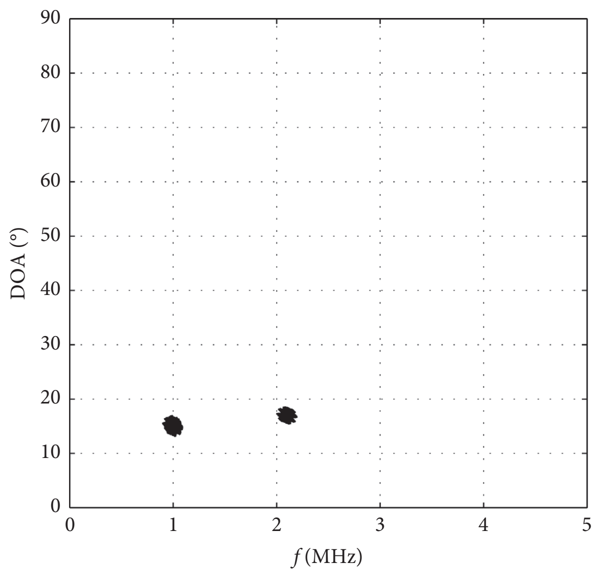

Figure 13: The identification ability of the proposed method.

the condition of a nonuniform array, such as array element position deviation [32] and uneven distance between array elements.

In this section, we assume that the array receives signals emitted by three incoherent far-field sources. The DOAs and operating frequencies of the signals are $(\theta_1, f_1) = (15^{\circ}, 1\,\text{MHz})$, $(\theta_2, f_2) = (20^{\circ}, 1.9\,\text{MHz})$, and $(\theta_3, f_3) = (30^{\circ}, 2.8\,\text{MHz})$. SNR = 0 dB, $M = 12$, $P = 5$, $N = 300$, and $K = 3$. For analyzing array element position deviation, we set $d = [0; 50; 101; 149; 200; 251; 300; 352; 401; 449; 501; 548]\ m$. For uneven distance between array elements, we set $d = [0; 40; 100; 150; 195; 235; 310; 365; 395; 450; 500; 540]\ m$. The scatter diagram of the joint frequency and DOA estimation of the proposed method in this paper is shown in Figures 14 and 15. Figures 14 and 15 show that the proposed method is efficient in estimating the frequency and DOA results for both nonuniform array conditions.

3.2.8. Analysis of the Performances of Different Methods. In this section, we focus on analyzing the performances of different methods. We assume that the array receives signals emitted by two incoherent far-field sources. The DOAs and operating frequencies of the signals are $(\theta_1, f_1) = (15^{\circ}, 1\,\text{MHz})$ and $(\theta_2, f_2) = (40^{\circ}, 2.1\,\text{MHz})$. We set $d = 50\,\text{m}$, $K = 2$, $P = 2$, $N = 400$, and $M = 12$. The range of the SNR is from −15 dB to 15 dB (step: 2 dB), and the RMSEs of the Cramer–Rao lower bound (CRLB), the PM, the CR-PM, the ESPRIT method [16], the improved ESPRIT method [20], and the method proposed in this paper with respect to the frequency and DOA estimations are shown in Figures 16 and 17, respectively.

To quantitatively illustrate, under the condition of a low SNR, compared with the improved ESPRIT method [20], the estimate improvement of the method proposed in this paper, we define the relative improvement ratio as

$$\text{ratio}_{\text{frequency}} = 1 - \frac{\text{RMSE}_{\text{frequency}}\,(\text{CR} - \text{ESPRIT})}{\text{RMSE}_{\text{frequency}}\,(\text{Improved ESPRIT})} \times 100\%, \tag{35}$$

$$\text{ratio}_{\text{DOA}} = 1 - \frac{\text{RMSE}_{\text{DOA}}\,(\text{CR} - \text{ESPRIT})}{\text{RMSE}_{\text{DOA}}\,(\text{Improved ESPRIT})} \times 100\%. \tag{36}$$

According to the definitions of equations (35) and (36), we show the relative improvement ratio in Figures 18 and 19.

As shown in Figures 16 and 17, when the SNR is within the range of −15 dB to 15 dB (in steps of 2 dB), the estimation accuracy of the proposed method is better than that of the PM, the CR-PM, the ESPRIT method [16], and the improved ESPRIT method [20] in terms of both the DOA and frequency. Among them, the ESPRIT method has extremely poor angle estimation accuracy since it cannot automatically pair parameters.

As shown in Figures 18 and 19, when SNR = −15 dB to −1 dB, compared with the improved ESPRIT method, the estimation accuracy of the proposed method is greatly improved. In particular, when SNR = −15 dB, compared with the improved ESPRIT method, the frequency estimation accuracy of the method proposed in this paper is an approximately 25.50% improvement; the DOA estimation

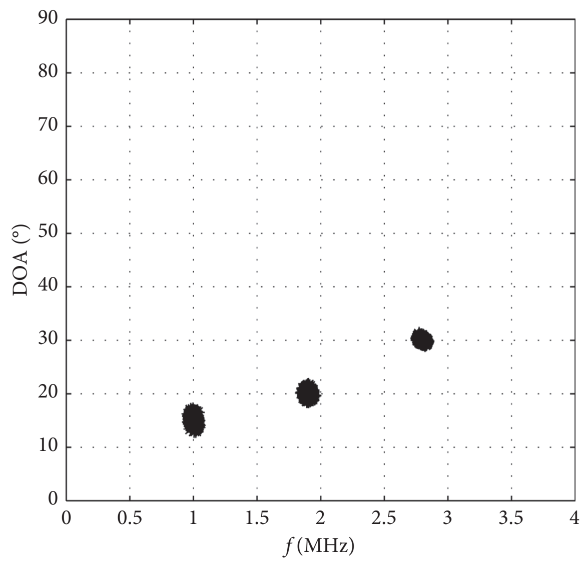

Figure 14: Parameter estimation for array element position deviation.

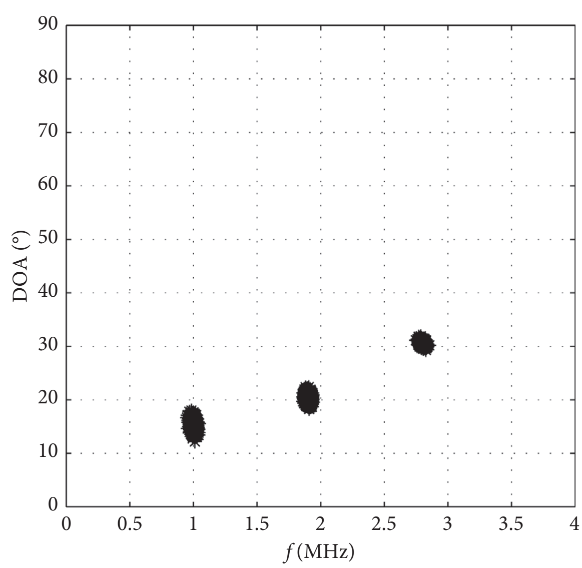

Figure 15: Parameter estimation for uneven distances between array elements.

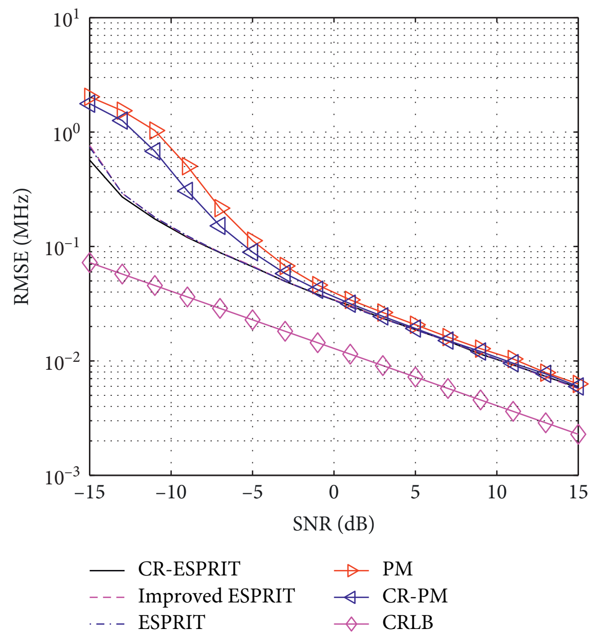

Figure 16: RMSEs of f_k under different methods.

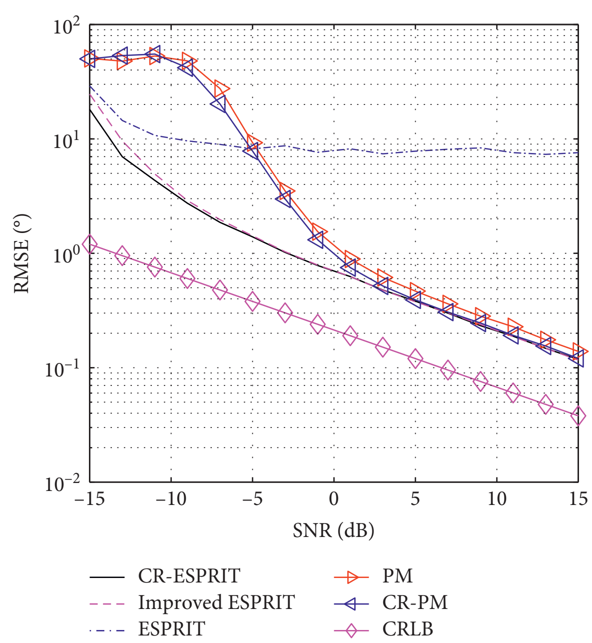

Figure 17: RMSEs of the DOA under different methods.

accuracy of the method proposed in this paper is an approximately 31.95% improvement. However, when SNR = −1 dB to 15 dB, the relative improvement ratio fluctuates around zero. This result illustrates that the estimation accuracy of the proposed method is almost the same as that of the improved ESPRIT method. For fluctuation, we surmise that the reason for this phenomenon may be the result of too few simulations in this paper.

In summary, a comprehensive analysis of Figures 16–19 shows that the estimation accuracy of the proposed method is improved over that of the PM, the CR-PM, the ESPRIT method, and the improved ESPRIT method. The results further verify that the method proposed in this paper has good anti-noise performance and stability under different SNRs. Therefore, compared to the PM, the CR-PM, the ESPRIT method, and the improved ESPRIT method, the method proposed in this paper is more suitable for use in a complex electromagnetic environment.

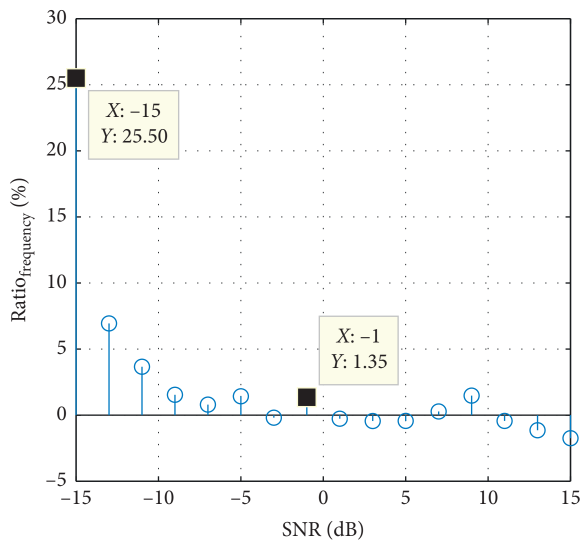

FIGURE 18: The relative improvement ratios of the frequency estimation.

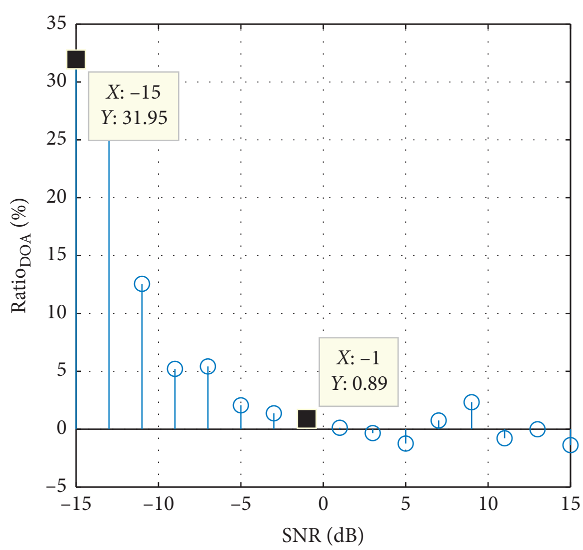

FIGURE 19: The relative improvement ratios of the DOA estimation.

4. Conclusions

For linear arrays, this paper proposes a joint angle and frequency estimation method based on CR-ESPRIT. We first preprocess the received signal by taking full advantage of the conjugate information contained in the originally received data, and we reconstruct a new total covariance matrix. Then, we use the LS-ESPRIT algorithm to estimate the frequency parameter. According to the unique relationship between angles and frequencies, we estimate the DOAs based on the reconstructed received signal. The complexity of the method proposed in this paper is almost the same as that of the ESPRIT and the improved ESPRIT. Numerical simulations and comparisons with the PM, the CR-PM, the ESPRIT method, and the improved ESPRIT method prove the superiority of the proposed method. In a real space environment, under the condition of a uniform or a nonuniform array, this method can realize the automatic pairing of the estimated DOAs and frequencies of radiation source signals without an additional parameter pairing process. Moreover, this method has high accuracy and strong anti-noise performance when conducting parameter estimation.

Data Availability

The data used to support the findings of the study are included within this paper.

Conflicts of Interest

The authors declare that there are no conflicts of interest regarding the publication of this paper.

Acknowledgments

The authors would like to thank Prof. M. H. PAN for his support and funding for this project. The authors thank C. Wang and C. B. Ye for their help. This work was supported by the National Natural Science Foundation of China under Grant no. 61671241.

References

[1] J.-D. Lin, W.-H. Fang, Y.-Y. Wang, and J.-T. Chen, “FSF MUSIC for joint DOA and frequency estimation and its performance analysis,” *IEEE Transactions on Signal Processing*, vol. 54, no. 12, pp. 4529–4542, 2006.

[2] J. R. Jensen, M. G. Christensen, and S. H. Jensen, “Nonlinear least squares methods for joint DOA and pitch estimation,” *IEEE Transactions on Audio, Speech, and Language Processing*, vol. 21, no. 5, pp. 923–933, 2013.

[3] V. Varadarajan and J. Krolik, “Array shape estimation and tracking using active sonar reverberation,” *IEEE Transactions on Aerospace and Electronic Systems*, vol. 40, no. 3, pp. 1073–1086, 2004.

[4] J. Wang, G. Ding, Q. Wu, L. Shen, and F. Song, “Spatial-temporal spectrum hole discovery: a hybrid spectrum sensing and geolocation database framework,” *Chinese Science Bulletin*, vol. 59, no. 16, pp. 1896–1902, 2014.

[5] X. Zeng, B. Tang, and Y. Xiong, “Interception algorithm of S-cubed signal model in stealth radar equipment,” *Chinese Journal of Aeronautics*, vol. 25, no. 3, pp. 416–422, 2012.

[6] G. Hu, Y. Zhang, M. Jing, Y. Tang, and B. Gu, “Credibility test for blind processing results of sinusoid using Chebyshev’s Inequality,” in *Proceedings of the 2013 IEEE International Conference on Signal Processing, Communication and Computing (ICSPCC 2013)*, pp. 1–6, IEEE, Kunming, China, August 2013.

[7] G. Hu, P. Zhao, Z. Chen, and R. Luo, “Confidence evaluation for blind analysis of LFM/BPSK hybrid signals based on extreme value theory,” *IET Radar, Sonar & Navigation*, vol. 13, no. 3, pp. 473–482, 2018.

[8] G. Hu and P. Zhao, “Confidence test for blind analysis of BPSK signals,” *IEEE Transactions on Aerospace and Electronic Systems*, vol. 55, no. 2, pp. 658–675, 2019.

[9] M. A. Hannan, P. Rocca, and A. Massa, “Robust BCS-based direction-of-arrival and bandwidth estimation of unknown signals for cognitive radar,” in *Proceedings of the 2018 IEEE International Symposium on Antennas and Propagation and*

USNC/URSI National Radio Science Meeting, pp. 625-626, IEEE, Boston, MA, USA, May 2018.
[10] M. Zuo, S. Xie, Y. Li, and C. Zhang, "Joint estimation method for frequency and DOA of virtual antenna array in space-time domain," in *Proceedings of the 2019 International Applied Computational Electromagnetics Society Symposium - China (ACES)*, pp. 1-2, IEEE, Nanjing, China, August 2019.
[11] X. Huang, L. Cao, and A. Liu, "Sequential estimation of frequency and direction-of-arrival based on the relaxed coprime array for multiple targets," *IEEE Access*, vol. 8, pp. 80318–80332, 2020.
[12] X. Zhang, L. Xu, L. Xu, and D. Xu, "Direction of departure (DOD) and direction of arrival (DOA) estimation in MIMO radar with reduced-dimension MUSIC," *IEEE Communications Letters*, vol. 14, no. 12, pp. 1161–1163, 2010.
[13] X. Zhang and D. Xu, "Angle estimation in bistatic MIMO radar using improved reduced dimension Capon algorithm," *Journal of Systems Engineering and Electronics*, vol. 24, no. 1, pp. 84–89, 2013.
[14] C. Wang, *Research on Identification and Parameter Estimation of Intra-pulse Modulated Signals at Low SNR*, Northeast Normal University, Changchun, China, 2019.
[15] S. Sirianunpiboon, S. D. Howard, and S. D. Elton, "Time-decentralized DOA estimation for electronic surveillance," in *Proceedings of the 2017 51st Asilomar Conference on Signals, Systems, and Computers*, pp. 1137–1141, IEEE, Pacific Grove, CA, USA, June 2017.
[16] X. Wang, "Joint angle and frequency estimation using multiple-delay output based on ESPRIT," *EURASIP Journal on Advances in Signal Processing*, vol. 2010, no. 1, Article ID 358659, 2010.
[17] R. Schmidt, "Multiple emitter location and signal parameter estimation," *IEEE Transactions on Antennas and Propagation*, vol. 34, no. 3, pp. 276–280, 1986.
[18] A. N. Lemma, A. van der Veen, and E. F. Deprettere, "Analysis of joint angle-frequency estimation using ESPRIT," *IEEE Transactions on Signal Processing*, vol. 51, no. 5, pp. 1264–1283, 2003.
[19] Z. Sun, X. Zhang, H. Wu, and J. Liu, "Propagator method-based joint angle and frequency estimation using multiple delay output," *ICIC Express Letters*, vol. 2, no. 4, pp. 827–832, 2011.
[20] X. Wang, X. Zhang, J. Li, and J. Bai, "Improved ESPRIT method for joint direction-of-arrival and frequency estimation using multiple-delay output," *International Journal of Antennas and Propagation*, vol. 2012, pp. 1018–1020, 2012.
[21] Y. Gao, Y. Ma, S. Li, X. Zhou, and S. Wu, "A novel joint angle and frequency estimation method based on the extended OMP algorithm," in *Proceedings of the 2019 IEEE Globecom Workshops (GC Wkshps)*, pp. 1–5, IEEE, Waikoloa, HI, USA, May 2019.
[22] L. Xu, F. Wen, and X. Zhang, "A novel unitary PARAFAC algorithm for joint DOA and frequency estimation," *IEEE Communications Letters*, vol. 23, no. 4, pp. 660–663, 2019.
[23] B. E. Nazarenko, T. K. Artemova, and A. S. Gvozdarev, "Linear antenna array circular bending effect on the impedance matrix and input impedances' unbalance," in *Proceedings of the 2020 International Youth Conference on Radio Electronics, Electrical and Power Engineering (REEPE)*, pp. 1–5, IEEE, Moscow, Russia, July 2020.
[24] A. A. Kumar, S. G. Razul, M. G. Chandra, C. M. See, and P. Balamuralidhar, "Joint frequency and direction of arrival estimation with space-time array," in *Proceedings of the 2016 IEEE Sensor Array and Multichannel Signal Processing Workshop (SAM)*, pp. 1–5, IEEE, Rio de Janeiro, Brazil, October 2016.
[25] L. Xu, R. Wu, X. Zhang, and Z. Shi, "Joint two-dimensional DOA and frequency estimation for L-shaped array via compressed sensing PARAFAC method," *IEEE Access*, vol. 6, pp. 37204–37213, 2018.
[26] L. Xu, R. Wu, X. Zhang, and Z. Shi, "Efficient 2-D DOA and frequency estimation for L-shaped array via RD-PM," *International Journal of Electronics*, vol. 106, no. 9, pp. 1394–1411, 2019.
[27] S. Zheng, X. Zhang, B. Zong, and J. Xu, "Parameter estimation of the 3D-GTD model based on a modified 3D-ESPRIT algorithm," *Journal of Beijing University of Posts and Telecommunications*, vol. 43, no. 4, pp. 32–38, 2020.
[28] S. Zheng, X. Zhang, Y. Guo, B. Zong, and J. Xu, "Parameter estimation of 1D GTD scattering center model based on an improved MUSIC algorithm," *Journal of Beijing University of Aeronautics and Astronautics*, vol. 46, no. 11, pp. 2149–2155, 2020.
[29] L. Xu, R. Wu, and X. Zhang, "2D-DOA and frequency estimation for L-shaped array via reduced-dimensional MUSIC," *Systems Engineering and Electronics*, vol. 41, no. 1, pp. 1–8, 2019.
[30] C. Chen and X. Zhang, "A coherent direction of arrival estimation method using a single pulse," *Computers and Electrical Engineering*, vol. 40, no. 5, pp. 1731–1740, 2014.
[31] A. Ferréol, P. Larzabal, and M. Viberg, "Statistical analysis of the MUSIC algorithm in the presence of modeling errors, taking into account the resolution probability," *IEEE Transactions on Signal Processing*, vol. 58, no. 8, pp. 4156–4166, 2010.
[32] Y. Tian, J. X. Shi, and Y. R. Wang, "Direction of arrival estimation method using partly calibrated nested array in the presence of gain-phase errors," *Acta Electronica Sinica*, vol. 47, no. 12, pp. 2465–2471, 2019.

Hindawi
Mathematical Problems in Engineering
Volume 2021, Article ID 5584688, 8 pages
https://doi.org/10.1155/2021/5584688

Research Article

Computationally Efficient Unitary ESPRIT Algorithm in Bistatic MIMO Radar

Baobao Liu ,[1] Tao Xue,[1] Cong Xu,[2] and Yongjun Liu[3]

[1]*School of Computer Science, Xi'an Polytechnic University, Xi'an 710048, China*
[2]*School of Information Engineering, Xijing University, Xi'an 710123, China*
[3]*School of Electronic Engineering, Xidian University, Xi'an 710071, China*

Correspondence should be addressed to Baobao Liu; liubaobao1222@163.com

Received 2 March 2021; Revised 12 April 2021; Accepted 6 June 2021; Published 17 June 2021

Academic Editor: Junpeng Shi

A low complexity unitary estimating signal parameter via rotational invariance techniques (ESPRIT) algorithm is presented for angle estimation in bistatic multiple-input-multiple-output (MIMO) radar. The devised algorithm only requires calculating two submatrices covariance matrix, which reduces the computation cost in comparison with subspace methods. Moreover, the signal subspace can be efficiently acquired by exploiting the NystrÖm method, which only needs $O(MNK^2)$ flops. Thus, the presented algorithm has an essentially diminished computational effort, especially useful when $K \ll MN$, while it can achieve efficient angle estimation accuracy as well as the existing algorithms. Several theoretical analysis and simulation results are provided to demonstrate the usefulness of the proposed scheme.

1. Introduction

Target estimation has been a significant problem in radar systems, which has been applied in widespread in sonar, guidance systems, speech processing, communication, medical signal processing, and other fields [1–3]. In recent years, considerable research interests have been drawn to MIMO radar [4–13], which exploits multiple antennas to emit diverse waveforms and utilizes multiple antennas to receive the echo signals [14]. This leads to its more underlying benefits over phased-array radar [15–17] (e.g., enhancing the spatial resolution, fading effect overcoming, and enhancing the parameter identifiability). MIMO radar can be regarded as an expansion of the phased-array radar, where the exploited waveforms are effectively independent [18]. Generally, MIMO radars can be divided into two types, the collocated MIMO radar and the statistical MIMO radar, based on the different array antenna configurations [19]. Furthermore, the collocated MIMO radars are categorised into two types, namely, the monostatic MIMO radar and the multistatic MIMO radar. Due to the fact that the emitting and receiving antennas are not in the identical location, the DOD and DOA estimation has become a considerable research matter [4, 18–21]. In our work, we mainly focus on the DOD and DOA estimation issue in the bistatic MIMO radar.

According to the recent researches, several algorithms [4–10] have been proposed for estimation angle in the bistatic MIMO radar. In [4], the reduced-dimension multiple signal classification (MUSIC) algorithm that uses one-dimensional search is presented to angle estimation, which achieves high angle estimation accuracy in comparison with Capon algorithm [20]. In [5], the Capon algorithm is extended to DOD and DOA estimation, which has heavy computational complexity for requiring two-dimensional angle search. Moreover, the technique is subjected to some performance degradations for the proximate receiving steering vector. Besides, the estimation of angles needs peak searching with computational intensive. The root-MUSIC algorithm [6] without peak searching is presented by utilizing polynomial rooting technique to reduce the computational cost. In [7], the ESPRIT technique that uses the invariance technique of both the transmitting array and the receiving array is presented to estimate angle in the bistatic MIMO radar. However, the algorithm requires the pairing operation. In [8], to address the problem of automatic pairing, a combination ESPRIT-MUSIC algorithm is developed, which provides beneficial angle accuracy. In [9], a unitary ESRPIT technique that exploits the real-valued processing is devised for estimating angle in the bistatic MIMO radar, which has high estimation precision. In [10], the maximum likelihood algorithm is presented for direction finding estimation in MIMO radar. In [22], the novel joint angle estimation method is proposed by using tensor decomposition in the nested bistatic MIMO radar. Moreover, various methods are introduced for bistatic MIMO radar in [23–25]. However, the abovementioned algorithms have a large amount of computation since they require the calculation of sample covariance matrix (SCM) and its eigenvalue decomposition (EVD) to obtain the noise subspace or signal noise, especially for large MIMO radar array and a great deal of snapshots scenarios. In order to tackle this serious problem, a computationally efficient algorithm is devised for direction estimation in this work. Unlike the existing algorithms [4–10], the presented algorithm only requires to compute two submatrices of the SCM, which avoids calculating of SCM and its EVD by exploiting the NystrÖm technique. The proposed method can be also applied in the nonuniform linear array, L-shape array, and uniform circular array for angle estimation. The NystrÖm method has been extensively applied in speed up methods [26, 27] and is first utilized by Williams and Seeger [27] for sparsifying kernel matrices. By exploiting the NystrÖm method [28, 29], we extend the previous work [30] and develop a low complexity unitary ESPRIT algorithm which not only has high angle estimation precision but also obtains light computational cost, especially in large MIMO radar array scenario. In this paper, we derive a new powerful unitary ESPRIT approach, which exhibits many benefits as follows: (a) it has much lower computational cost than that of the ESRPIT and unitary ESPRIT methods; (b) it enjoys higher angle estimation precision than the ESPRIT algorithm; (c) it is suitable for direction finding estimation of large MIMO radar array. The benefits of the presented algorithm are shown by some simulation experiments.

2. Data Model

In this paper, we think about a bistatic MIMO radar system (Figure 1) constituted of M-transmitting antenna array and N-receiving antenna array, both of which are half-wavelength spaced uniform linear arrays [7–9]. Assume that there exist P noncoherent targets located in the same range bin. The DOD and DOA of the pth target relative to the transmitting array normal and the receiving array normal are denoted by θ_p and ϕ_p $(p = 1, 2, \ldots, P)$, respectively. Thus, the signal model can be given as [7, 8]

$$\mathbf{y}(t) = \mathbf{A}\mathbf{s}(t) + \mathbf{n}(t), \tag{1}$$

where $\mathbf{A} = [\mathbf{a}_1, \mathbf{a}_2, \ldots, \mathbf{a}_P]$ denotes an $MN \times P$ matrix consisting of the P steering vectors and $\mathbf{a}_p = \mathbf{a}_r(\phi_p) \otimes \mathbf{a}_t(\theta_p)$ illustrates the Kronecker product of the receiving array steering vector and the transmitting array steering vector for the pth source. $\mathbf{a}_r(\phi_p)$ and $\mathbf{a}_t(\theta_p)$ are respectively rewritten as

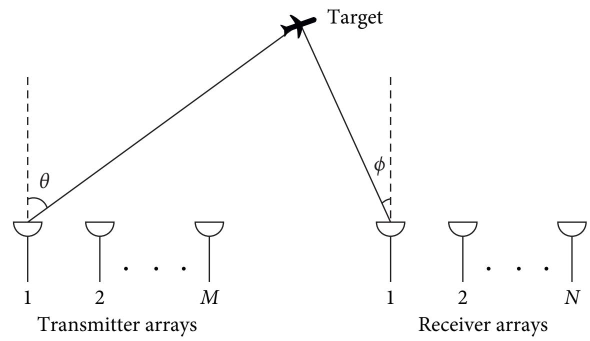

Figure 1: Radar configuration.

$$\begin{aligned}
\mathbf{a}_r(\phi_p) &= \left[1, \exp(j\pi v_p), \ldots, \exp(j\pi(N-1)v_p)\right]^T, \\
\mathbf{a}_t(\theta_p) &= \left[1, \exp(j\pi u_p), \ldots, \exp(j\pi(M-1)u_p)\right]^T,
\end{aligned} \tag{2}$$

and $u_p = \sin\theta_p, v_p = \sin\phi_p$, where ϕ_p and θ_p represent the DOA and DOD, respectively. $\mathbf{s}(t) = [s_1(t), s_2(t), \ldots, s_P(t)]^T$ is a column vector, in which $s_p(t) = \alpha_p e^{j2\pi f_{dp} t}$ denotes the envelope of the reflected signal with α_p being the amplitude containing the reflection coefficients and path losses and so on [7–9]. $\mathbf{n}(t)$ denotes an $MN \times 1$ complex Gaussian white noise vector with zero mean and covariance matrix $\sigma^2 I_{MN}$.

3. NystrÖm Method-Based Unitary ESPRIT for Angle Estimation

3.1. Real-Valued Processing. In order to reduce computational complexity, we have to transform the complex data to real data by matrix method since the array, the received data, is complex data. Let $\mathbf{Y}$ be represented as the data matrix consisting of L snapshots $\mathbf{y}(t_l)$, $1 \le l \le L$. The augmented data matrix is defined as $\mathbf{Z} = [\mathbf{Y}\boldsymbol{\Pi}_{MN}\mathbf{Y}^*\boldsymbol{\Pi}_L]$, where $\boldsymbol{\Pi}_{MN}$ represents the exchange matrix including J ones on its antidiagonal and zeros elsewhere. Then, the real-valued matrix is expressed as [9, 11]

$$\boldsymbol{\Gamma} = \mathbf{Q}_{MN}^H \mathbf{Z} \mathbf{Q}_{2L}, \tag{3}$$

where $\mathbf{Q}_J$ signifies sparse unitary matrix, expressed as

$$\begin{aligned}
\mathbf{Q}_{2J} &= \frac{1}{\sqrt{2}} \begin{bmatrix} \mathbf{I}_J & j\mathbf{I}_J \\ \boldsymbol{\Pi}_J & -j\boldsymbol{\Pi}_J \end{bmatrix}, \\
\mathbf{Q}_{2J+1} &= \frac{1}{\sqrt{2}} \begin{bmatrix} \mathbf{I}_J & 0 & j\mathbf{I}_J \\ \mathbf{0}^T & \sqrt{2} & \mathbf{0}^T \\ \boldsymbol{\Pi}_J & 0 & -j\boldsymbol{\Pi}_J \end{bmatrix}.
\end{aligned} \tag{4}$$

3.2. Signal Subspace Estimation. To use the NystrÖm technique [27, 28] for estimating angle, we disintegrate the matrix $\boldsymbol{\Gamma}$ as follows [30]:

$$\mathbf{\Gamma} = \begin{bmatrix} \mathbf{\Gamma}_1 \\ \mathbf{\Gamma}_2 \end{bmatrix}, \tag{5}$$

where $\Gamma_1 \in \mathbb{R}^{K\times L}$ and $\Gamma_2 \in \mathbb{R}^{(MN-K)\times L}$ are the real-valued submatrices received by the first K antenna and the rest of the $(MN-K)$ antennas, respectively. We define

$$\mathbf{R}_{11} = \mathbf{E}\left[\mathbf{\Gamma}_1\mathbf{\Gamma}_1^H\right], \quad \mathbf{R}_{21} = \mathbf{E}\left[\mathbf{\Gamma}_2\mathbf{\Gamma}_1^H\right]. \tag{6}$$

Moreover, we must ensure that $\mathbf{R}_{11}$ denotes full rank matrix where K satisfies $\{K \mid P \le K \le \min(MN, L)\}$, $K = 1, 2, \ldots, MN$. It is noted that K has not been required to ascend substantially with MN. For instance, when MN grows from 10 to 30, a relatively little K, such as $K = 12$, is sufficient to insure estimating precision, which also reduces the computational complexity.

Suppose that the EVD of $\mathbf{R}_{11}$ is $\mathbf{U}_{11}\Lambda_{11}\mathbf{U}_{11}^H$, where $\mathbf{U}_{11} \in \mathbb{C}^{K\times K}$ denotes the eigenvector matrix and Λ_{11} represents the diagonal matrix. Defining $\mathbf{U}_{21} \triangleq \mathbf{R}_{21}\mathbf{U}_{11}\Lambda_{11}^{-1}$, we can constitute a new matrix as follows [30]:

$$\mathbf{U} \triangleq \begin{bmatrix} \mathbf{U}_{11} \\ \mathbf{U}_{21} \end{bmatrix}. \tag{7}$$

Then, according to the results from the remark, we can obtain the signal subspace without the computation of SCM and its EVD.

Remark 1 (see [30]). Suppose that the EVD of $\mathbf{G}^H\mathbf{G}$ is $\mathbf{U}_G\Lambda_G\mathbf{U}_G^H$ and $\mathbf{G} = \mathbf{U}\Lambda_{11}^{1/2}$, where $\Lambda_G = \operatorname{diag}[\lambda_{G1}, \ldots, \lambda_{GK}]$ denotes the eigenvalue matrix with $\lambda_{G1} \ge \cdots \ge \lambda_{GK}$ and $\mathbf{U}_G = [\mathbf{u}_{G1}, \ldots, \mathbf{u}_{GK}]$ represents the corresponding eigenvector matrix with $\mathbf{u}_{Gi}\,(i = 1, \ldots, K)$ being the ith eigenvector. Then, the signal subspace is constructed by the first P column vectors of Π as follows:

$$\operatorname{span}\{\mathbf{E}_s\} = \operatorname{span}\{\mathbf{A}\}, \tag{8}$$

where $\mathbf{E}_s \triangleq \Pi(:, 1{:}\ P)$ and $\Pi = \mathbf{G}\mathbf{U}_G$.

3.3. Angle Estimation. Then, according to the unitary ESPRIT algorithm [9, 11], the real-valued invariance relation is described as follows:

$$\mathbf{F}_2^\theta\mathbf{d}_p = \tan\left(\frac{\pi u_p}{2}\right)\mathbf{F}_1^\theta\mathbf{d}_p, \tag{9}$$

where $\mathbf{F}_1^\theta = \operatorname{Re}\left\{\mathbf{Q}_{(M-1)N}^H \operatorname{diag}^N\left\{\mathbf{J}_2^\theta\right\}\mathbf{Q}_{MN}\right\}$ and $\mathbf{F}_2^\theta = \operatorname{Im}\left\{\mathbf{Q}_{(M-1)N}^H\operatorname{diag}^N\left\{\mathbf{J}_2^\theta\right\}\mathbf{Q}_{MN}\right\}$ denote real-valued matrix, respectively, and $\mathbf{J}_2^\theta$ is defined in [9, 11]. $\mathbf{d}_p = \mathbf{Q}_{MN}^H\mathbf{a}_p$ denotes a steering vector that is real-valued. Thus, $\mathbf{F}_2^\theta\mathbf{E}_s = \mathbf{F}_1^\theta\mathbf{E}_s\mathbf{\Psi}_\theta$ represents the real-valued invariance equation for the transmitter array where $\mathbf{\Psi}_\theta = \mathbf{T}^{-1}\mathbf{\Phi}_\theta\mathbf{T}$ and $\mathbf{\Phi}_\theta = \operatorname{diag}[\tan(\pi u_1/2), \tan(\pi u_1/2), \ldots, \tan(\pi u_p/2)]$ signifies a real-valued diagonal matrix whose diagonal elements include information of estimating DOD [9, 11]. In the receiving array, similarly, the real-valued invariance equation is constructed by

$$\mathbf{F}_2^\phi\mathbf{E}_s = \mathbf{F}_1^\phi\mathbf{E}_s\mathbf{\Psi}_\phi, \tag{10}$$

where $\mathbf{F}_1^\phi = \operatorname{Re}\left\{\mathbf{Q}_{(M-1)N}^H\mathbf{J}_2^\phi\mathbf{Q}_{MN}\right\}$ and $\mathbf{F}_2^\phi = \operatorname{Im}\left\{\mathbf{Q}_{(M-1)N}^H \mathbf{J}_2^\phi\mathbf{Q}_{MN}\right\}$, $\mathbf{J}_1^\phi = [\mathbf{I}_{M(N-1)\times M(N-1)}\mathbf{0}_{M(N-1)\times M}]$ and $\mathbf{J}_2^\phi = [\mathbf{0}_M (N-1)\times M\mathbf{I}_{M(N-1)\times M(N-1)}]$, $\mathbf{\Psi}_\phi = \mathbf{T}^{-1}\Phi_\phi\mathbf{T}$, $\Phi_\phi = \operatorname{diag}[\tan(\pi v_1/2), \tan(\pi v_2/2), \ldots, \tan(\pi v_p/2)]$, and $\mathbf{T}$ stands for a nonsingular matrix. $\mathbf{\Phi}_\theta$ represents a real-valued diagonal matrix whose diagonal elements include information of estimating DOA. Then, $\mathbf{\Psi}_\theta + j\mathbf{\Psi}_\varphi$ is described as [9, 11]

$$\mathbf{\Psi}_\theta + j\mathbf{\Psi}_\varphi = \mathbf{T}^{-1}\{\mathbf{\Psi}_\theta + j\mathbf{\Psi}\}\mathbf{T}. \tag{11}$$

Then, the DODs and DOAs can be estimated by

$$\begin{aligned} \widehat{\theta}_p &= \arcsin\left\{2\arctan\frac{\left([\mathbf{\Phi}_\theta]_{pp}\right)}{\pi}\right\}, \quad p = 1, \ldots, P, \\ \widehat{\phi}_p &= \arcsin\left\{2\arctan\frac{\left([\mathbf{\Phi}_\phi]_{pp}\right)}{\pi}\right\}, \quad p = 1, \ldots, P. \end{aligned} \tag{12}$$

4. Computational Complexity and Cramér-Rao Bound (CRB)

The presented technique does not need utilizing the whole SCM. Instead, it requires calculating $\mathbf{R}_{11}$ and $\mathbf{R}_{21}$ which need $O(LK^2)$ and $O(MNLK - LK^2)$ flops, respectively. Meanwhile, the signal subspace is constructed by exploiting the NystrÖm approach, where the computational complexity is $O(MNK^2)$. Thus, the presented method requires $O(MNLK + MNK^2)$. However, the classical unitary ESPRIT and ESPRIT algorithms need $O((M^2N^2L + M^3N^3)/4)$ and $O(M^2N^2L + M^3N^3)$ flops, respectively, which are much higher than $O(MNLK + MNK^2)$ flops on condition that $K \ll \min(MN, L)$. Furthermore, referring to [11], we use CRB in simulation as follows:

$$\mathrm{CRB} = \frac{\sigma^2}{2L}\left\{\operatorname{Re}\left[\mathbf{D}^H\mathbf{\Pi}_A^\perp \odot \widehat{\mathbf{P}}_w^T\right]\right\}^{-1}, \tag{13}$$

where

$$\mathbf{D} = \left[\frac{\partial \mathbf{a}_1}{\partial \theta_1}, \frac{\partial \mathbf{a}_2}{\partial \theta_2}, \dots, \frac{\partial \mathbf{a}_k}{\partial \theta_k}, \frac{\partial \mathbf{a}_1}{\partial \phi_1}, \frac{\partial \mathbf{a}_2}{\partial \phi_2}, \dots, \frac{\partial \mathbf{a}_k}{\partial \phi_k}\right],$$

$$\mathbf{\Pi}_A^{\perp} = \mathbf{I}_{MN} - \mathbf{A}\left(\mathbf{A}^H\mathbf{A}\right)^{-1}\mathbf{A}^H,$$

$$\widehat{\mathbf{P}}_w = \begin{bmatrix} \widehat{\mathbf{P}}_s & \widehat{\mathbf{P}}_s \\ \widehat{\mathbf{P}}_s & \widehat{\mathbf{P}}_s \end{bmatrix}, \tag{14}$$

$$\widehat{\mathbf{P}}_s = \frac{1}{L}\sum_{t=1}^{L} \mathbf{s}(t)\mathbf{s}^H(t).$$

5. Simulation Results

In this installment, a vast number of computer simulations are demonstrated to prove the effectiveness of the proposed technique. We compare performance of the estimating angle of the presented method with the ESPRIT algorithms [7] and unitary ESPRIT [9] and present their computational complexity analysis. In the following simulation experiments, 200 Monte-Carlo iterations are adopted for the bistatic MIMO radar in the experiments. We suppose that there exist three noncoherent targets and their location is at angles $(\theta_1, \phi_1) = (10^\circ, 20^\circ)$, $(\theta_2, \phi_2) = (-8^\circ, 30^\circ)$, and $(\theta_3, \phi_3) = (0^\circ, 45^\circ)$, respectively. The root mean squared error (RMSE) of over angle [9] is exploited in the simulation experiments.

Figures 2 and 3 describe the angle estimation paired results of the presented scheme with SNR = 10 dB and SNR = 10 dB, respectively. It can be shown that the transmit angles (DODs) and receive angles (DOAs) can be clearly seen. Figure 3 also implies that the presented scheme can efficiently estimate angle of the targets in low SNR scenario.

Figures 4 and 5 demonstrate performance comparison of the estimating angle with $M = 8$, $N = 6$ and $M = 6$, $N = 6$, respectively. We compare the presented technique with the ESPRIT and the unitary ESPRIT methods. Figures 4 and 5 demonstrate that the proposed algorithm has much better estimation precision than the ESPRIT method and enjoys high estimation precision that is almost the same as the unitary ESPRIT scheme at high SNR range. However, the presented algorithm is somewhat inferior to the unitary ESPRIT scheme at the low SNR scenario.

Figures 6–9 show performance comparison of estimation of the presented technique with $L = 50$ and $L = 100$ for different M/N, respectively. From Figures 6–9, we can find that the angle estimation precision of the presented scheme is significantly enhanced with the number of transmitting array elements/receiving array elements increasing. Multiple receiving/transmitting array elements enhance estimation precision owing to diversity gain.

Figures 10 and 11 illustrate estimation precision comparison of the presented technique with $M = 6$ and $N = 6$ for different values of L, respectively. As shown in Figures 10 and 11, the estimation precision of the presented technique is boosted with L increasing. Meanwhile, Figure 10 also indicates that the presented method has

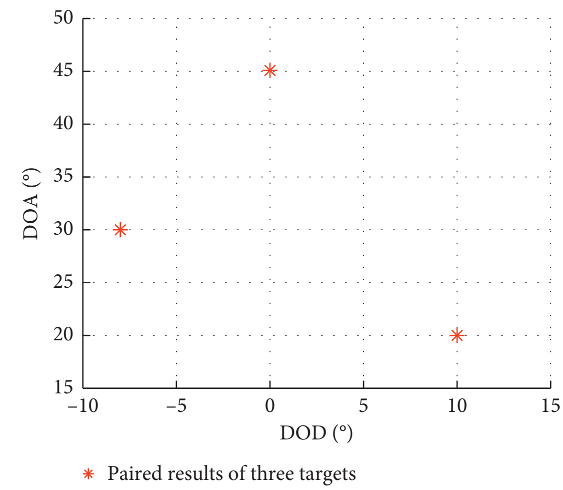

FIGURE 2: Paired results with SNR = 10 dB, $M = 8$, $N = 6$, and $L = 200$.

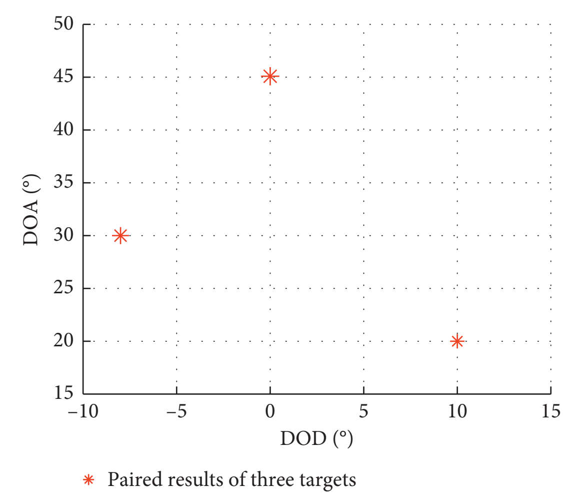

FIGURE 3: Paired results with SNR = 5 dB, $M = 8$, $N = 6$, and $L = 200$.

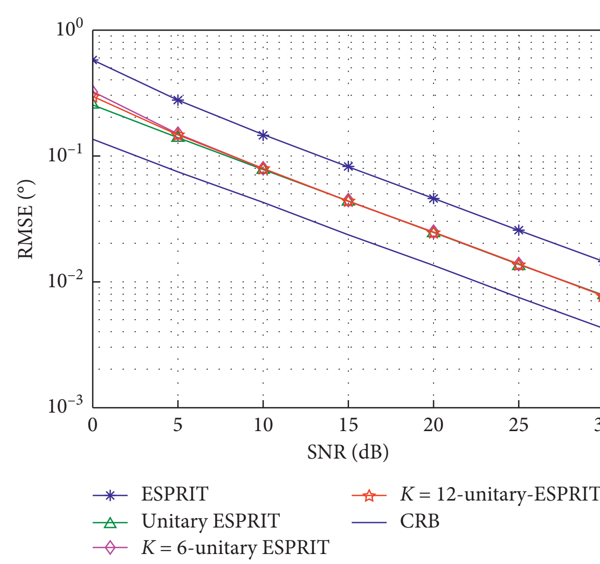

FIGURE 4: RMSE with $M = 8$, $N = 6$, and $L = 50$.

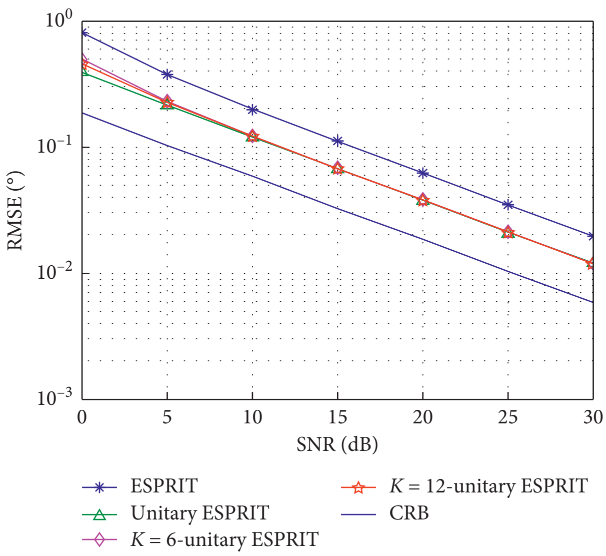

Figure 5: RMSE with $M = 6$, $N = 6$, and $L = 50$.

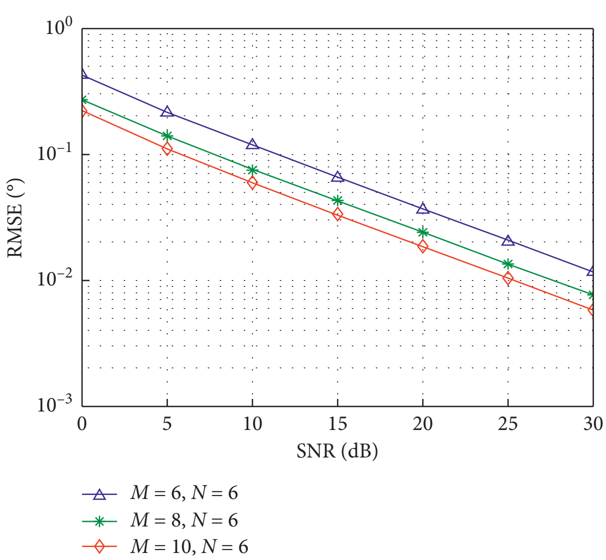

Figure 6: RMSE with $L = 50$ and different M.

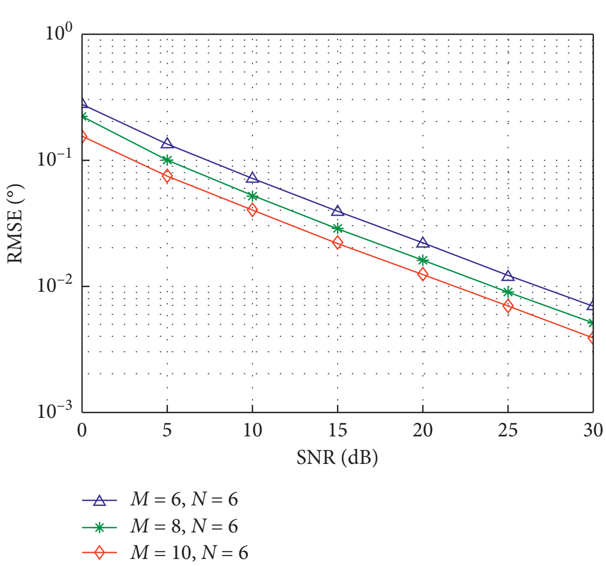

Figure 7: RMSE with $L = 100$ and different M.

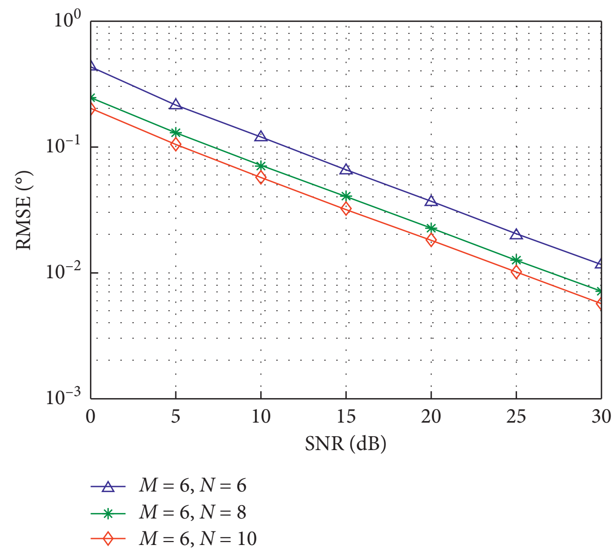

Figure 8: RMSE with $L = 50$ and different N.

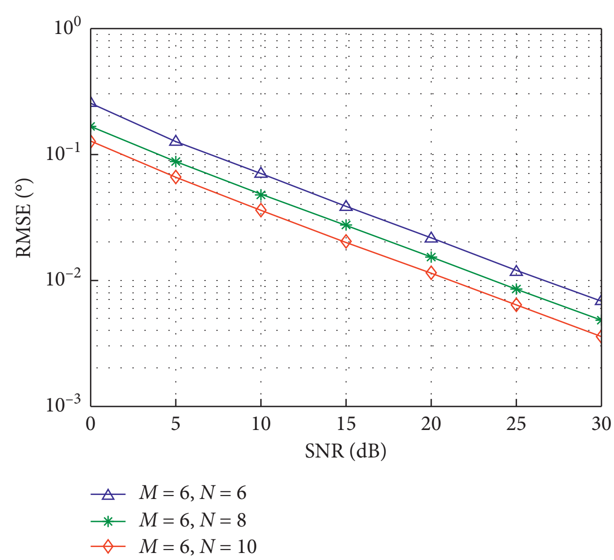

Figure 9: RMSE with $L = 100$ and different N.

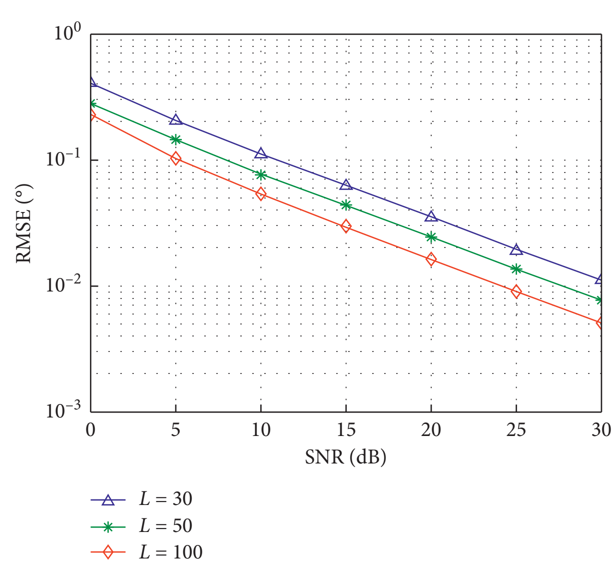

Figure 10: RMSE with $M = 6$, $N = 6$, and different L.

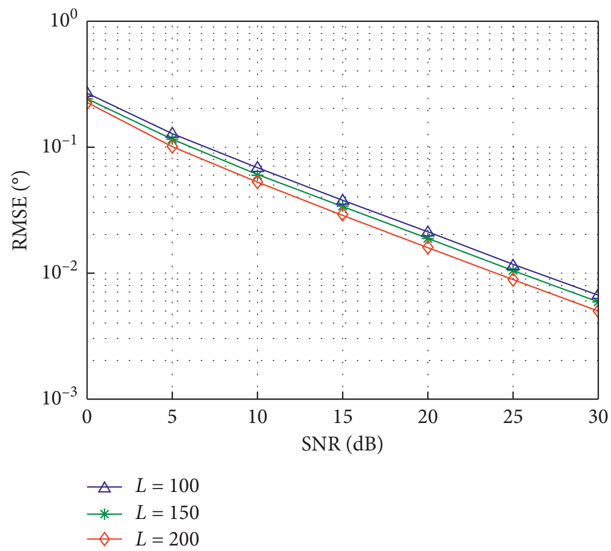

Figure 11: RMSE with $M = 6$, $N = 6$, and different L.

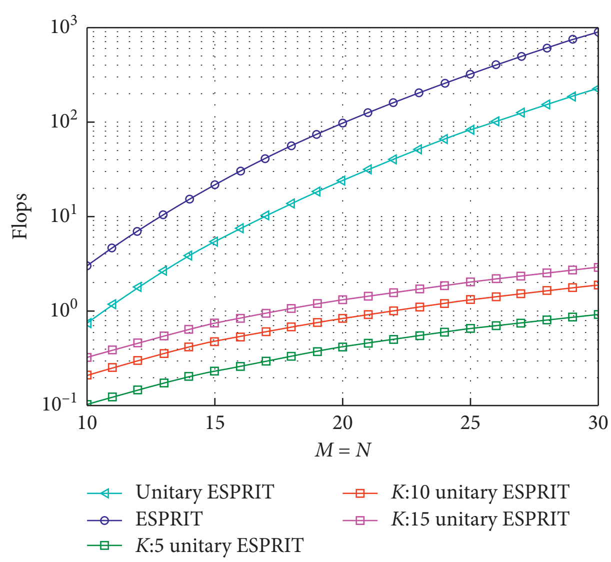

Figure 12: Complexity comparison with $L = 200$.

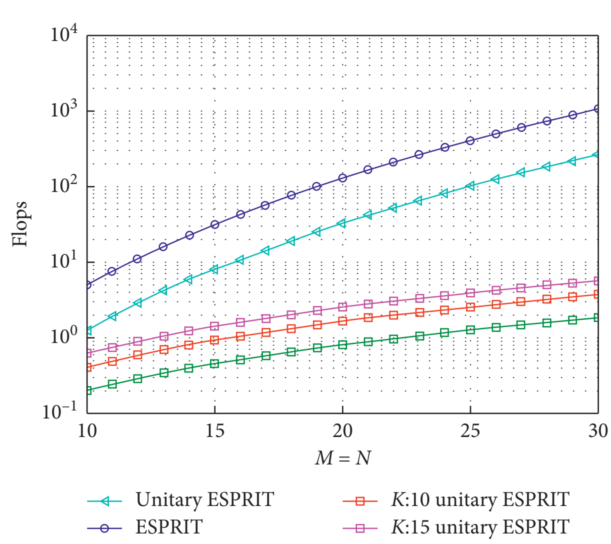

Figure 13: Complexity comparison with $L = 400$.

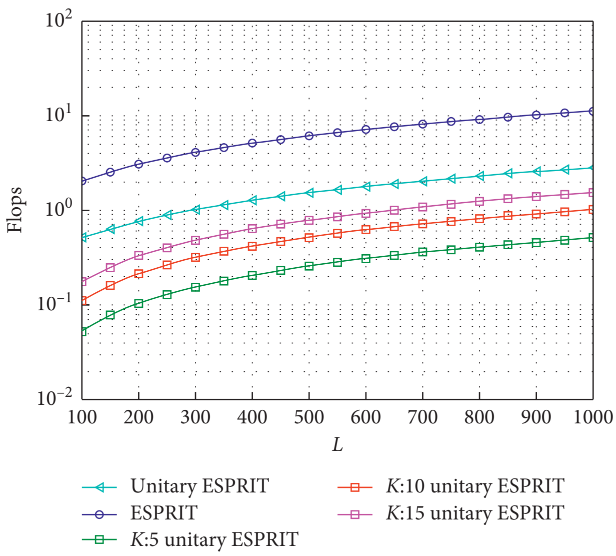

Figure 14: Complexity comparison against L with $M = N = 10$.

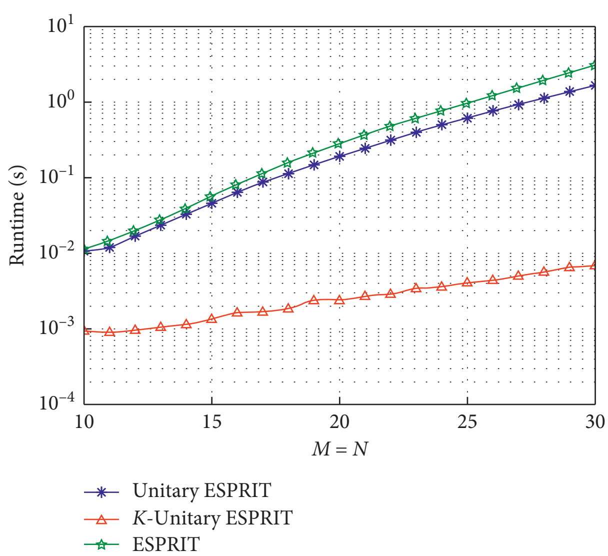

Figure 15: Runtime comparison versus $M = N$ with $L = 100$ and $K = 12$.

beneficial estimation precision at small number of snapshots scenario.

Figures 12–14 illustrate the complexity comparison with $K = 5, 10, 15$, where we can find the proposed algorithm has much less computational cost in comparison with the ESPRIT and the unitary ESPRIT schemes, particularly when $M = N$ becomes larger.

Figure 15 and Table 1 describe the runtime of the three ESPRIT schemes. They depict the average CPU time required to calculate each ESPRIT approach on the personal computer with Intel(R) core(TM) 2 Duo CPU T3700 processor. We can clearly observe that the presented approach is much more computationally effective than the existing schemes, especially when $M = N$ becomes bigger.

Table 1: Computations time comparison ($P = 3$, $L = 100$, $K = 12$, and SNR = 10 dB).

Transmit and receive elements	Unitary ESPRIT average runtime (s)	ESPRIT average runtime (s)	Proposed method average runtime (s)
$M = N = 10$	0.01023	0.01081	0.00089
$M = N = 15$	0.04329	0.05503	0.00132
$M = N = 20$	0.18280	0.27440	0.00234
$M = N = 25$	0.59890	0.94800	0.00397
$M = N = 30$	1.60200	2.90600	0.00654

6. Conclusion

In this paper, we have developed a low complexity unitary ESPRIT method for estimating angle in the bistatic MIMO radar. Compared with the existing unitary ESPRIT and ESPRIT algorithms which require $O((M^2N^2L + M^3N^3)/4)$ and $O(M^2N^2L + M^3N^3)$ flops, respectively, our approach only needs $O(2MNLK + MNK^2)$ flops, thereby being much more computationally effective, especially for the case of a large MIMO radar array. Moreover, extensive simulation results demonstrate that the estimation precision of the presented scheme is much higher by comparison with the ESPRIT method and very similar to the unitary ESPRIT algorithm. In the future research, the presented technique can be extended to a different application such as estimating angle in the monostatic MIMO radar.

Data Availability

The relevant data used to support the findings of this study are within the manuscript.

Conflicts of Interest

The authors declare that there are no conflicts of interest in this work.

Acknowledgments

The authors wish to express their sincere thanks to the Natural Science Research Plan in Shaanxi Province of China (General Program, no.2020JM-574), the Ph.D Science Foundation of Polytechnic University (no.107020313), the National Natural Science Foundation of China (no.62001352), and the Technology Innovation Guidance Project of Shaanxi Province of China (no.2020CGXNG-012) for their support.

References

[1] A. Hassanien and S. A. Vorobyov, "Transmit energy focusing for DOA estimation in MIMO radar with colocated antennas," *IEEE Transactions on Signal Processing*, vol. 59, no. 6, pp. 2669–2682, 2011.

[2] Y. L. Yang, X. P. Mao, Y. G. Hou, and G. J. Jiang, "2-D DOA estimation via correlation matrix reconstruction for nested L-shaped array," *Digital Signal Processing*, vol. 98, pp. 1–11, 2020.

[3] C. J. Hung, "Fast DOA estimation algorithm based on a combination of an orthogonal projection and noise pseudo-eigenvector approach," *ISRN Signal Processing*, vol. 2011, Article ID 751670, 8 pages, 2011.
[4] H. D. Yan, J. Li, and G. S. Liao, "Multitarget identification and localization using bistatic MIMO radar systems," *EURASIP Journal on Advances in Signal Processing*, vol. 2008, Article ID 973932, 8 pages, 2008.
[5] M. L. Bencheikn, Y. D. Wang, and H. Y. He, "Polynomial root finding technique for joint DOD and DOD estimation in bistatic MIMO radar," *Signal Processing*, vol. 90, pp. 2723–2730, 2010.
[6] D. F. Chen, B. X. Chen, and G. D. Qian, "Angle estimation using ESPRIT in MIMO radar," *Electronics Letters*, vol. 44, no. 12, pp. 770-771, 2008.
[7] M. L. Bencheikh and Y. Wang, "Joint DOD-DOA estimation using combined ESPRIT-MUSIC approach in MIMO radar," *Electronics Letters*, vol. 46, no. 15, pp. 1081–1083, 2010.
[8] G. Zheng, B. Chen, and M. Yang, "Unitary ESPRIT algorithm for bistatic MIMO radar," *Electronics Letters*, vol. 48, no. 3, pp. 179–181, 2012.
[9] B. Tang, J. Tang, Y. Zhang, and Z. D. Zhang, "Maximum likelihood estimation of DOD and DOA for bistatic MIMO radar," *Signal Processing*, vol. 93, pp. 1394–1357, 2013.
[10] W.-G. Tang, H. Jiang, and S.-X. Pang, "Grid-free DOD and DOA estimation for MIMO radar via duality-based 2D atomic norm minimization," *IEEE Access*, vol. 7, pp. 60827–60836, 2019.
[11] X. Zhang and D. Xu, "Angle estimation in bistatic MIMO radar using improved reduced dimension Capon algorithm," *Journal of Systems Engineering and Electronics*, vol. 24, no. 1, pp. 84–89, 2013.
[12] J. Shi, G. Hu, X. Zhang, and F. Sun, "Sparsity-based DOA estimation of coherent and uncorrelated targets with flexible MIMO radar," *IEEE Transactions on Vehicular Technology*, vol. 68, no. 6, pp. 5835–5848, 2019.
[13] H. Zhang, W. Liu, Z. Zhang, W. Lu, and J. Xie, "Joint target assignment and power allocation in multiple distributed MIMO radar networks," *IEEE Systems Journal*, vol. 15, no. 1, pp. 694–704, 2021.
[14] X. Zhang, C. Chen, and J. Li, "Angle estimation using quaternion-ESPRIT in bistatic MIMO-radar," *Wireless Personal Communications*, vol. 69, no. 2, pp. 551–560, 2013.
[15] E. Fishler, A. Haimovich, R. Blum et al., "An idea whose time has come," in *Proceedings of the 2004 International Radar Conference*, pp. 71–78, Delft, Netherlands, April 2004.
[16] J. Li and P. Stoica, "MIMO radar with colocated antennas," *IEEE Signal Processing Magazine*, vol. 24, no. 5, pp. 106–114, 2007.
[17] B. Liao, "Fast angle estimation for MIMO radar with non-orthogonal waveforms," *IEEE Transactions on Aerospace and Electronic Systems*, vol. 54, no. 4, pp. 2091–2096, 2018.
[18] H. Ali, S. Ahmed, M. S. Sharawi, M. S. Alouini, and T. Y. Al-Naffouri, "Reduced complexity DOA and DOD estimation for a single moving target in bistatic MIMO radar," *Signal Processing*, vol. 166, pp. 1–11, 2020.
[19] Y. Cheng, R. Yu, H. Gu, and W. Su, "Multi-SVD based subspace estimation to improve angle estimation accuracy in bistatic MIMO radar," *Signal Processing*, vol. 93, no. 7, pp. 2003–2009, 2013.
[20] X. Zhang and D. Xu, "Angle estimation in MIMO radar using reduced-dimension Capon," *Electronics Letters*, vol. 46, no. 12, pp. 860-861, 2010.
[21] X. Zhang, L. Xu, L. Xu, and D. Xu, "Direction of departure (DOD) and direction of arrival (DOA) estimation in MIMO radar with reduced-dimension MUSIC," *IEEE Communications Letters*, vol. 14, no. 12, pp. 1161–1163, 2010.
[22] M. Haardt and J. A. Nossek, "Unitary ESPRIT: how to obtain increased estimation accuracy with a reduced computational burden," *IEEE Transactions on Signal Processing*, vol. 43, no. 5, pp. 1232–1242, 1995.
[23] B. Xu and Y. Zhao, "Transmit beamspace based unitary parallel factor method for DOD and DOA estimation in bistatic MIMO radar," *IEEE Access*, vol. 6, pp. 65573–65581, 2018.
[24] Y. D. Guo, Y. S. Zhang, and N. N. Tong, "Beamspace ESPRIT algorithm for bistatic MIMO radar," *Electronics Letters*, vol. 47, no. 15, pp. 876–878, 2011.
[25] A. Nicholas and J. W. Patrick, "Estimating principal components of large covariance matrices using the NystrÖm method," in *Proceedings of the IEEE International Conference on Acoustics, Speech, and Signal Processing (ICASSP)*, pp. 3784–3787, Prague, Czech Republic, May 2011.
[26] P. Drineas and W. M. Micheal, "On the NystrÖm method for approximating a gram matrix for improved kernel-based learning," *Journal of Machine Learning Research*, vol. 6, pp. 2153–2175, 2005.
[27] C. K. I. Williams and M. Seeger, "Using the NystrÖm method to speed up kernel machines," *Advances in Neural Information Processing Systems 2000*, MIT Press, Cambridge, MA, USA, 2001.
[28] C. Fowlkes, S. Belongie, F. Chung, and J. Malik, "Spectral grouping using the nystrom method," *IEEE Transactions on Pattern Analysis and Machine Intelligence*, vol. 26, no. 2, pp. 214–225, 2004.
[29] C. Qian, L. Huang, and H. C. So, "Computationally efficient ESPRIT algorithm for direction-of-arrival estimation based on Nyström method," *Signal Processing*, vol. 94, pp. 74–80, 2014.
[30] J. P. Shi, F. Q. Wen, and T. P. Liu, "Nested MIMO radar: coarrays, tensor modeling and angle estimation," *IEEE Transactions on Aerospace and Electronic Systems*, vol. 57, no. 1, pp. 574–585, 2021.

Hindawi
Mathematical Problems in Engineering
Volume 2021, Article ID 7521573, 8 pages
https://doi.org/10.1155/2021/7521573

Research Article

Joint TOA and DOA Estimation for UWB Systems with Antenna Array via Doubled Frequency Sample Points and Extended Number of Clusters

Liangliang Gong, Yang Hu, Junyao Zhang, and Gaofeng Zhao

NARI Group Corporation (State Grid Electric Power Research Institute), Nanjing 211000, China

Correspondence should be addressed to Liangliang Gong; gongliangliangnr@163.com

Received 12 April 2021; Accepted 29 May 2021; Published 7 June 2021

Academic Editor: Junpeng Shi

The ultra-wideband (UWB) system, which transmits information using nanosecond or even sub-nanosecond pulses, has been widely applied in precise positioning. In this paper, we investigate the problem of the time of arrival (TOA) estimation and the direction of arrival (DOA) estimation in the UWB systems with antenna array and propose a joint TOA and DOA estimation algorithm with doubled frequency sample points and extended number of clusters. Specifically, the proposed algorithm uses two antennas to receive impinging signals and utilizes the conjugate symmetry characteristic of the delay matrices to extend the sample points as well as the number of clusters. Moreover, in order to obtain TOA estimates with low computational complexity, the proposed algorithm transforms the two-dimensional (2D) spectral search to one-dimensional (1D) searches. The DOA estimates can then be achieved by using the TOA estimation results and the geometric information. Simulation results are given to testify the performance of the proposed algorithm.

1. Introduction

The ultra-wideband (UWB) technique is a kind of wireless communication technology which uses nanosecond or even sub-nanosecond pulses as carrier to transmit information. Benefiting from the high transmission rate, low power consumption, and the anti-multipath characteristics, the UWB system has been widely applied in various fields such as radar, imaging, and positioning [1–3]. Due to the extremely narrow pulse, the positioning precision of the UWB system can reach centimeter level or even millimeter level. Even under complex multipath conditions such as indoor environment, the UWB system can still achieve accurate positioning due to its strong anti-multipath and penetration ability [4–6]. At present, IEEE 802.15.4a standard has taken UWB as the preferred technology for positioning application [7].

One of the basic problems in the UWB positioning system is the time of arrival (TOA) estimation. TOA estimation algorithms can be divided into two categories: one is the traditional algorithms based on the time domain, and the other is the high-resolution algorithms based on the frequency domain. The former mainly includes the coherent detection method using pulse template matched filter [8] and the incoherent TOA estimation algorithm based on threshold or energy detection [9–11]. The coherent algorithm based on matched filter can obtain TOA estimates with high accuracy but at the same time with high sampling rate, complex receiver structure, and expensive equipment cost. The incoherent TOA estimation algorithm has the advantages of low sampling rate, fast convergence speed, and low hardware resource occupation rate. However, the low sampling rate leads to low time resolution, which reduces the accuracy of the TOA estimation. The traditional time-domain-based algorithms obtain TOA estimates by estimating the arrival time of the direct path (DP) component in the received signal. However, due to the multipath effect and the nonline-of-sight (NLOS) condition, DP may not be the strongest path; thus the algorithm resolution declines. Therefore, super-resolution estimation algorithms based on frequency-domain processing are proposed [12–18]. These algorithms, such as the multiple signal classification (MUSIC) algorithm [12, 13], the propagator method (PM) [14], the estimation of signal parameters via rotational invariance techniques (ESPRIT) algorithm [15, 16], and the matrix pencil algorithm [17, 18], model the channel impulse response in frequency domain and realize the TOA estimation using the orthogonality between the signal subspace and the noise subspace, which can achieve high estimation resolution.

Researches on DOA estimation in UWB systems were also done. Since the UWB system has high time resolution, some joint TOA and DOA estimation algorithms were proposed. The matrix pencil algorithm was applied to the joint estimation in [19]. In [20], the rough TOA estimates were obtained via energy estimation and the minimum distance criterion, the accurate estimates were then achieved by a low-complexity and high-resolution method based on the signal power delay spectrum, and the DOA estimates were finally obtained by the minimum-variance unbiased estimation using the TOA estimation results. Besides, the electromagnetic vector sensor (EMVS) with multiple-input multiple-output (MIMO) radar [21] also has the potential to be exploited in the UWB systems.

In this paper, we investigate the problem of joint TOA and DOA estimation in UWB systems and propose a computationally efficient algorithm. Specifically, the proposed algorithm uses two antennas to receive impinging signals and utilizes the conjugate symmetry characteristic of the delay matrices to double the equivalent frequency sample points and extend the number of clusters. Moreover, to obtain TOA estimates with low computational complexity, the proposed algorithm transforms the two-dimensional (2D) spectral search to one-dimensional (1D) searches. The DOA estimates can then be achieved by using the TOA estimation results and the geometric information. The main contributions of this paper are summarized as follows:

(1) We propose an effective algorithm for UWB systems to jointly obtain the DOA and TOA estimation results.

(2) We transform the time-consuming 2D spectral search to twice 1D searches in order to release the computational burden.

(3) The proposed algorithm can obtain high estimation accuracy due to the doubled sample points and the extended number of clusters.

The rest of this paper is organized as follows: Section 2 introduces the data model of the UWB system. The proposed joint TOA and DOA estimation algorithm is derived in Section 3. Section 4 then analyses the estimation performance of the proposed algorithm and Section 5 gives the simulation results to testify the algorithm effectiveness. Finally, Section 6 concludes this paper.

Notation 1. In this paper, we use upper (lower) bold characters to represent matrices (vectors). $(\cdot)^*$, $(\cdot)^T$, and $(\cdot)^H$, respectively, denote the operation of conjugate, transpose, and conjugate transpose. $*$ denotes the convolution operation, and $\otimes$ denotes the Kronecker product. $\mathbf{A}(:, m{:}\, n)$ generates a new matrix consisted by the m-th to the n-th columns of the matrix $\mathbf{A}$. $E\{\cdot\}$ represents the expectation operation. $\mathbf{I}_M$ stands for an $M \times M$ identity matrix.

2. Data Model

2.1. Transmit Signals of UWB Systems. In this paper, we utilize the second derivation of the Gaussian pulse as the UWB transmit signal and modulate it with the direct sequence binary phase shift keying (DS-BPSK). The transmit signal of the UWB system can then be expressed as [22]

$$s(t) = \sum_{\gamma=-\infty}^{+\infty} \sum_{n=0}^{N_c-1} b_\gamma c_n p(t - \gamma T_s - nT_c), \tag{1}$$

where $b_\gamma \in \{-1, +1\}$ is the modulated binary data symbol sequence, $c_n \in \{-1, +1\}$ is the pseudorandom sequence used to realize the multiple access communication, T_c denotes the repeat period of the pulse, T_s represents the period of the binary data symbol, and N_c is the pulse repetition times of a single binary data symbol. The term $p(t)$ is the second derivation of the Gaussian pulse and can be further expressed as

$$p(t) = e^{-(2\pi t^2/\Gamma^2)}\left(1 - \left(4\pi t^2/\Gamma^2\right)\right), \tag{2}$$

where Γ is the pulse forming factor related to the pulse width.

2.2. Channel Model of UWB Systems. According to the Saleh–Valenzuela (SV) model [23], we consider that the transmit signal produces multiple multipath components after passing through the channel, and these multipath components arrive at the receiver in the form of clusters. Specifically, we assume there are K clusters and L multipath per cluster in the UWB channel, then the channel impulse response of the kth cluster is given by

$$h^{(k)}(t) = \sum_{l=1}^{L} \alpha_l^{(k)} e^{j\theta_l^{(k)}} \delta\left(t - \tau_l^{(k)}\right), \tag{3}$$

where $\alpha_l^{(k)}$ is the channel fading factor of the lth path in the kth cluster, which obeys the Rayleigh distribution. $\theta_l^{(k)}$ distributes uniformly in the range $[0, 2\pi]$, $\delta(\cdot)$ is the Dirac function, and $\tau_l^{(k)}$ is the channel delay of the lth path in the kth cluster. Normally, the change rate of the channel is slow compared with the pulse speed of the transmit signal; hence we have $\tau_l^{(k)} = \tau_l$. Define $\beta_l^{(k)} = \alpha_l^{(k)} e^{j\theta_l^{(k)}}$ to denote the random complex fading amplitude, then (3) can be rewritten as

$$h^{(k)}(t) = \sum_{l=1}^{L} \beta_l^{(k)} \delta(t - \tau_l). \tag{4}$$

2.3. Received Signals of UWB Systems. According to the basic theory of the digital signal processing, the received signal of the kth cluster in the time domain can be expressed as [23]

$$y^{(k)}(t) = s(t) * h^{(k)}(t) + w^{(k)}(t) = \sum_{l=1}^{L} \sum_{\gamma=-\infty}^{+\infty} \sum_{n=1}^{N_c-1} \beta_l^{(k)} b_\gamma c_n p(t - \gamma T_s - nT_c - \tau_l) + w^{(k)}(t), \tag{5}$$

where $w^{(k)}(t)$ is the additive Gaussian white noise of the kth cluster. Transform (5) into frequency domain, *i.e.*,

$$Y^{(k)}(\omega) = S(\omega)H^{(k)}(\omega) + W^{(k)}(\omega) = \sum_{l=1}^{L} \beta_l^{(k)} S(\omega) e^{-j\omega\tau_l} + W^{(k)}(\omega), \tag{6}$$

where $Y^{(k)}(\omega)$, $S(\omega)$, $H^{(k)}(\omega)$, and $W^{(k)}(\omega)$, respectively, represent the Fourier transformation of $y^{(k)}(t)$, $s(t)$, $h^{(k)}(t)$, and $w^{(k)}(t)$. Subsequently, by sampling N $(N > L)$ points with interval $\Delta\omega = (2\pi/N)$ in the frequency domain, we can obtain the measurement data vector as [23]

$$\mathbf{y}_k = \mathbf{S}\mathbf{E}(\tau)\boldsymbol{\beta}_k + \mathbf{w}_k, \tag{7}$$

where vector $\mathbf{y}_k = [Y^{(k)}(\omega_0), \ldots, Y^{(k)}(\omega_{N-1})]^T$ with $\omega_n = n\Delta\omega$ $(n = 0, 1, \ldots, N-1)$. $\mathbf{S} = \operatorname{diag}\{S(\omega_0), \ldots, S(\omega_{N-1})\}$ is an $N \times N$ diagonal matrix. $\mathbf{E}(\tau) = [\mathbf{e}(\tau_1), \mathbf{e}(\tau_2), \ldots, \mathbf{e}(\tau_L)]$ is the delay matrix which contains the information of the signal multipath delay, where $\mathbf{e}(\tau_i) = [1, e^{-j\Delta\omega\tau_i}, \ldots, e^{-j(N-1)\Delta\omega\tau_i}]^T$. Moreover, $\beta_k = [\beta_1^{(k)}, \beta_2^{(k)}, \ldots, \beta_L^{(k)}]^T$ contains the complex channel fading factor of the kth cluster and $\mathbf{w}_k = [W^{(k)}(\omega_0), W^{(k)}(\omega_1), \ldots, W^{(k)}(\omega_{N-1})]^T$ is the observe vector of the noise.

In this paper, we use two array antennas to receive the impinging signals. As shown in Figure 1, we assume there are L far-field signals from direction $\{\theta_1, \theta_2, \ldots, \theta_L\}$. The TOA of the two antennas is $\tau = [\tau_1, \tau_2, \ldots, \tau_L]$ and $\varsigma = [\varsigma_1, \varsigma_2, \ldots, \varsigma_L]$, respectively. The distance between the two antennas is d, and c denotes the light speed. According to (7), the received signal of the two antennas in the frequency domain can be expressed as [23]

$$\begin{aligned} \mathbf{Y}_1 &= \mathbf{S}\mathbf{E}_1(\tau)\mathbf{B} + \mathbf{W}_1, \\ \mathbf{Y}_2 &= \mathbf{S}\mathbf{E}_2(\varsigma)\mathbf{B} + \mathbf{W}_2, \end{aligned} \tag{8}$$

where $\mathbf{B} = [\beta_1\ \beta_2\ \ldots\ \beta_K]$, $\mathbf{W}_1 = [\mathbf{w}_1^{(1)}\ \mathbf{w}_2^{(1)}\ \ldots\ \mathbf{w}_K^{(1)}]$, and $\mathbf{W}_2 = [\mathbf{w}_1^{(2)}\ \mathbf{w}_2^{(2)}\ \ldots\ \mathbf{w}_K^{(2)}]$. $\mathbf{E}_1(\tau)$ and $\mathbf{E}_2(\varsigma)$ are the delay matrices of the two antennas, respectively, which can be expressed as

$$\mathbf{E}_1(\tau) = [\mathbf{e}_1(\tau_1)\ \ \mathbf{e}_1(\tau_2)\ \ \ldots\ \ \mathbf{e}_1(\tau_L)] = \begin{bmatrix} 1 & 1 & \cdots & 1 \\ e^{-j\Delta\omega\tau_1} & e^{-j\Delta\omega\tau_2} & \cdots & e^{-j\Delta\omega\tau_L} \\ \vdots & \vdots & \ddots & \vdots \\ e^{-j(N-1)\Delta\omega\tau_1} & e^{-j(N-1)\Delta\omega\tau_2} & \cdots & e^{-j(N-1)\Delta\omega\tau_L} \end{bmatrix}, \tag{9}$$

$$\mathbf{E}_2(\varsigma) = [\mathbf{e}_2(\varsigma_1)\ \ \mathbf{e}_2(\varsigma_2)\ \ \ldots\ \ \mathbf{e}_2(\varsigma_L)] = \begin{bmatrix} 1 & 1 & \cdots & 1 \\ e^{-j\Delta\omega\varsigma_1} & e^{-j\Delta\omega\varsigma_2} & \cdots & e^{-j\Delta\omega\varsigma_L} \\ \vdots & \vdots & \ddots & \vdots \\ e^{-j(N-1)\Delta\omega\varsigma_1} & e^{-j(N-1)\Delta\omega\varsigma_2} & \cdots & e^{-j(N-1)\Delta\omega\varsigma_L} \end{bmatrix}. \tag{10}$$

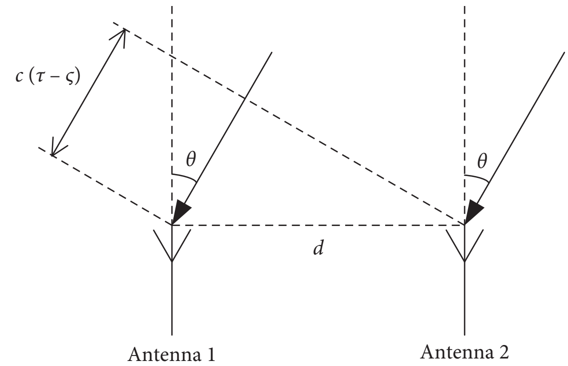

Figure 1: Array model.

The estimation of the two channel impulse responses in the frequency domain can be achieved by

$$\begin{aligned} \widehat{H}_1 &= \frac{\mathbf{Y}_1}{\mathbf{S}} = \mathbf{E}_1(\tau)\mathbf{B} + \mathbf{V}_1, \\ \widehat{H}_2 &= \frac{\mathbf{Y}_2}{\mathbf{S}} = \mathbf{E}_2(\varsigma)\mathbf{B} + \mathbf{V}_2, \end{aligned} \tag{11}$$

where $\mathbf{V}_1 = (\mathbf{W}_1/\mathbf{S})$ and $\mathbf{V}_2 = (\mathbf{W}_2/\mathbf{S})$. In the next section, we propose a joint TOA and DOA estimation algorithm utilizing the channel impulse response $\widehat{H}_1$ and $\widehat{H}_2$.

3. Proposed Algorithm

3.1. Sample Points and Clusters Extension. The cross-correlation matrix of the channel impulse response can be constructed as

$$\mathbf{R}_H = E\{\mathbf{H}_1\mathbf{H}_2^H\} \approx \mathbf{E}_1(\tau)\mathbf{R}_B\mathbf{E}_2^H(\varsigma), \tag{12}$$

where $\mathbf{R}_B = E\{\mathbf{B}\mathbf{B}^H\} \in \mathbb{C}^{L\times L}$ is a diagonal matrix. We divide the cross-correlation matrix $\mathbf{R}_H \in \mathbb{C}^{N\times N}$ into two $N \times (N-1)$ matrices, *i.e.*,

$$\mathbf{X}_1 = \mathbf{R}_H(:, 1{:}\ N-1) = \mathbf{E}_1(\tau)\mathbf{R}_B\mathbf{E}_{2a}^H(\varsigma), \tag{13}$$

$$\mathbf{X}_2 = \mathbf{R}_H(:, 2{:}\ N) = \mathbf{E}_1(\tau)\mathbf{R}_B\mathbf{E}_{2b}^H(\varsigma), \tag{14}$$

where $\mathbf{X}_1$ and $\mathbf{X}_2$ consist of the first and the last $N-1$ columns of $\mathbf{R}_H$ and $\mathbf{E}_{2a}(\varsigma)$ and $\mathbf{E}_{2b}(\varsigma)$ consist of the first and the last $N-1$ rows of $\mathbf{E}_2(\varsigma)$. According to the form of the delay matrix, we have

$$\mathbf{E}_{2b}(\varsigma) = \mathbf{E}_{2a}(\varsigma)\boldsymbol{\Psi}(\varsigma), \tag{15}$$

where $\Psi(\varsigma)$ is an $L \times L$ diagonal matrix given by

$$\boldsymbol{\Psi}(\varsigma) = \begin{bmatrix} e^{-j\Delta\omega\varsigma_1} & & & \\ & e^{-j\Delta\omega\varsigma_2} & & \\ & & \ddots & \\ & & & e^{-j\Delta\omega\varsigma_L} \end{bmatrix}. \tag{16}$$

According to (9) and (10), the two delay matrices of the two antennas are Vandermonde matrices and have the characteristic of conjugate symmetry, *i.e.*,

$$\begin{aligned}\mathbf{J}_N\mathbf{E}_1^*(\tau) &= \mathbf{E}_1(\tau)\widetilde{\Phi}(\tau),\\ \mathbf{J}_N\mathbf{E}_2^*(\varsigma) &= \mathbf{E}_2(\varsigma)\widetilde{\Phi}(\varsigma),\end{aligned} \tag{17}$$

where $\mathbf{J}_N \in \mathbb{C}^{N\times N}$ is the antidiagonal matrix, and the rotation matrices $\widetilde{\Phi}(\tau)$ and $\widetilde{\Phi}(\varsigma)$ are, respectively, given by

$$\begin{aligned}\widetilde{\Phi}(\tau) &= \begin{bmatrix} e^{-j\Delta\omega\tau_1} & & \\ & e^{-j\Delta\omega\tau_2} & \\ & & \ddots \\ & & & e^{-j\Delta\omega\tau_L}\end{bmatrix},\\ \widetilde{\Phi}(\varsigma) &= \begin{bmatrix} e^{-j\Delta\omega\varsigma_1} & & \\ & e^{-j\Delta\omega\varsigma_2} & \\ & & \ddots \\ & & & e^{-j\Delta\omega\varsigma_L}\end{bmatrix}.\end{aligned} \tag{18}$$

By utilizing the above properties of the delay matrices, we can construct a new matrix using $\mathbf{X}_1$ and $\mathbf{X}_2$ as

$$\mathbf{X} = \begin{bmatrix}\mathbf{X}_1, \mathbf{J}_N\mathbf{X}_2^*\\ \mathbf{X}_2, \mathbf{J}_N\mathbf{X}_1^*\end{bmatrix} = \mathbf{E}_e(\tau,\varsigma)\mathbf{B}_e(\tau,\varsigma), \tag{19}$$

where

$$\begin{aligned}\mathbf{E}_e(\tau,\varsigma) &= \begin{bmatrix}\mathbf{E}_1(\tau)\\ \mathbf{E}_1(\tau)\mathbf{\Psi}^*(\varsigma)\end{bmatrix} \in \mathbb{C}^{2N\times L},\\ \mathbf{B}_e(\tau,\varsigma) &= \left[\mathbf{R}_B\mathbf{E}_{2a}^H(\varsigma)\;\; \widetilde{\Phi}(\tau)\mathbf{R}_B\mathbf{\Psi}(\varsigma)\mathbf{E}_{2a}^T(\varsigma)\right] \in \mathbb{C}^{L\times 2(N-1)}.\end{aligned} \tag{20}$$

Equation (19) can be seen as the equivalent channel impulse response with doubled sample points and increased number of clusters, which can improve the maximum number of detectable signals as well as the estimation performance.

3.2. Reduced-Dimension TOA Estimation. The correlation matrix of the extended observation matrix $\mathbf{X}$ can be constructed as $\mathbf{R}_X = \mathbf{X}\mathbf{X}^H$. By applying the eigenvalue decomposition, the correlation matrix can be decomposed as

$$\mathbf{R}_X = \mathbf{U}_s\mathbf{\Lambda}_s\mathbf{U}_s^H + \mathbf{U}_v\mathbf{\Lambda}_v\mathbf{U}_v^H, \tag{21}$$

where $\mathbf{U}_s$ and $\mathbf{U}_v$ are the signal subspace and the noise subspace, respectively, and $\Lambda_s = \mathrm{diag}\{\lambda_1\;\lambda_2\;\ldots\;\lambda_L\}$ and $\Lambda_v = \mathrm{diag}\{\lambda_{L+1}\;\lambda_{L+2}\;\ldots\;\lambda_{2N}\}$ are diagonal matrices consisting of the largest L eigenvalues and the smallest $2N-L$ eigenvalues of $\mathbf{R}_X$.

Similar to the classical MUSIC algorithm, we can construct the 2D-MUSIC spectrum as

$$f_{2D}(\tau,\varsigma) = \frac{1}{\mathbf{e}_e^H(\tau,\varsigma)\mathbf{U}_v\mathbf{U}_v^H\mathbf{e}_e(\tau,\varsigma)}, \tag{22}$$

where

$$\mathbf{e}_e(\tau,\varsigma) = \begin{bmatrix}\mathbf{e}_1(\tau)\\ \mathbf{e}_1(\tau)e^{j\Delta\omega\varsigma}\end{bmatrix}. \tag{23}$$

Apparently, (22) needs time-consuming 2D spectral search to obtain TOA estimates. Aiming to reduce the computational complexity, we split $\mathbf{e}_e(\tau,\varsigma)$ as

$$\mathbf{e}_e(\tau,\varsigma) = \begin{bmatrix}1\\ e^{j\Delta\omega\varsigma}\end{bmatrix}\otimes\mathbf{e}_1(\tau) = (\mathbf{I}_2\otimes\mathbf{e}_1(\tau))\mathbf{q}(\varsigma), \tag{24}$$

where $\mathbf{q}(\varsigma) = [1, e^{j\Delta\omega\varsigma}]^T$. Substituting (24) into (23), the spectrum function can be rewritten as

$$f_{2D}(\tau,\varsigma) = \frac{1}{\mathbf{q}^H(\varsigma)\mathbf{F}(\tau)\mathbf{q}(\varsigma)}, \tag{25}$$

where $\mathbf{F}(\tau) = (\mathbf{I}_2\otimes e_1(\tau))^H\mathbf{U}_v\mathbf{U}_v^H(\mathbf{I}_2\otimes\mathbf{e}_1(\tau))$ and the vector $\mathbf{q}(\varsigma)$ satisfies $\mathbf{u}^H\mathbf{q}(\varsigma) = 1$ with $\mathbf{u} = [1,0]^T$. Equation (25) can be regarded as the following optimization problem:

$$\begin{aligned}&\min_{\tau,\varsigma}\mathbf{q}^H(\varsigma)\mathbf{F}(\tau)\mathbf{q}(\varsigma)\\ &\mathrm{s.t.}\,\mathbf{u}^H\mathbf{q}(\varsigma) = 1.\end{aligned} \tag{26}$$

According to (26), we can construct the cost function as

$$L(\tau,\varsigma) = \mathbf{q}^H(\varsigma)\mathbf{F}(\tau)\mathbf{q}(\varsigma) - \rho\left(\mathbf{u}^H\mathbf{q}(\varsigma) - 1\right), \tag{27}$$

where ρ is a constant value. In order to get the extremum, we can construct the partial derivation of $L(\tau,\varsigma)$ with respect to $\mathbf{q}(\varsigma)$, *i.e.*,

$$\frac{\partial L(\tau,\varsigma)}{\partial\mathbf{q}(\varsigma)} = 2\mathbf{F}(\tau)\mathbf{q}(\varsigma) + \rho\mathbf{u} = 0. \tag{28}$$

Thus, we have $\mathbf{q}(\varsigma) = \mu\mathbf{F}^{-1}(\tau)\mathbf{u}$ with $\mu = -0.5\rho$. Considering $\mathbf{u}^H\mathbf{q}(\varsigma) = 1$, the constant μ can be further expressed as

$$\mu = \frac{1}{\mathbf{u}^H\mathbf{F}^{-1}(\tau)\mathbf{u}}. \tag{29}$$

Therefore, the vector $\mathbf{q}(\varsigma)$ can be further transformed into

$$\mathbf{q}(\varsigma) = \frac{\mathbf{F}^{-1}(\tau)\mathbf{u}}{\mathbf{u}^H\mathbf{F}^{-1}(\tau)\mathbf{u}}. \tag{30}$$

Substituting (30) into (26), then the TOA estimation result of the first antenna is given by

$$\widehat{\tau} = \arg\min_{\tau}\frac{1}{\mathbf{u}^H\mathbf{F}^{-1}(\tau)\mathbf{u}} = \arg\max_{\tau}\mathbf{u}^H\mathbf{F}^{-1}(\tau)\mathbf{u}, \tag{31}$$

which means we can get the TOA estimation of the first antenna by a 1D spectral search with the spectral function

$$f(\tau) = \mathbf{u}^H\left((\mathbf{I}_2\otimes\mathbf{e}_1(\tau))^H\mathbf{U}_v\mathbf{U}_v^H(\mathbf{I}_2\otimes\mathbf{e}_1(\tau))\right)^{-1}\mathbf{u}. \tag{32}$$

Similarly, in order to obtain the TOA estimates of the second antenna, we can exchange the order of $\mathbf{H}_1$ and $\mathbf{H}_2$ when constructing the cross-correlation matrix, *i.e.*,

$$\mathbf{R}_H = E\left\{\mathbf{H}_2\mathbf{H}_1^H\right\} \approx \mathbf{E}_2(\varsigma)\mathbf{R}_B\mathbf{E}_1^H(\tau). \tag{33}$$

Then, by following the same procedures described above, the 1D spectral function with respect to the TOA of the second antenna is given by

$$f(\varsigma) = \mathbf{u}^H\Big(\left(\mathbf{I}_2 \otimes \mathbf{e}_2(\varsigma)\right)^H \mathbf{U}_v \mathbf{U}_v^H \left(\mathbf{I}_2 \otimes \mathbf{e}_2(\varsigma)\right)\Big)^{-1}\mathbf{u}. \tag{34}$$

After obtaining the TOA estimates of both antennas, we can estimate the DOA of the impinging signals by using the TOA estimates as well as the geometric information, *i.e.*,

$$\widehat{\theta}_l = \arcsin\left(\frac{c\left(\widehat{\tau}_l - \widehat{\varsigma}_l\right)}{d}\right), \quad l = 1, 2, \ldots, L. \tag{35}$$

The main steps of the proposed algorithm are summarized as follows:

(1) Construct the cross-correlation matrix $\mathbf{R}_H$ according to (12).

(2) Divide $\mathbf{R}_H$ into $\mathbf{X}_1$ and $\mathbf{X}_2$ according to (13) and (14), and construct the extended observation matrix $\mathbf{X}$ as (19).

(3) Compute the correlation matrix of $\mathbf{X}$, and perform the eigenvalue decomposition to obtain the noise subspace $\mathbf{U}_v$.

(4) Construct the spectral function according to (32) and perform the 1D spectral search to obtain the TOA estimates $\widehat{\tau}$.

(5) Reconstruct $\mathbf{R}_H$ using (33) and repeat Step 2 and Step 3. The TOA estimates $\widehat{\varsigma}$ can be obtained by performing 1D spectral search on (34).

(6) Calculate the DOA estimates according to (35).

4. Performance Analysis

4.1. Complexity. According to Section 3, when estimating the TOA of the first antenna τ, constructing $\mathbf{R}_H$ needs $O\{N^2K\}$, computing $\mathbf{R}_X$ needs $O\{8N^2(N-1)\}$, and performing eigenvalue decomposition on it requires $O\{8N^3\}$. Constructing the spectral function and conducting 1D spectral search needs $O\{4N^2(2N-L) + 8n_s(N^2+N+1)\}$, where n_s denotes the search times. Therefore, the total complexity of the proposed algorithm is $O\{2N^2K + 48N^3 - 8N^2(L+2) + 16n_s(N^2+N+1)\}$. If we perform 2D spectral search on equation (22), then the complexity is increased to $O\{N^2K + 24N^3 - 4N^2(L+2) + 2n_s^2N(2N+1)\}$. The computational complexity of the proposed algorithm and some other algorithms are concluded in Table 1. Besides, the complexity comparison versus the number of frequency sample points of different algorithms is depicted in Figure 2, where $K = 100$, $L = 3$, and $n_s = 100$. As shown in Figure 2, the complexity of the proposed algorithm is remarkably reduced compared with the algorithms with 2D spectral search and is close to the complexity of the 2D-PM.

4.2. Algorithm Advantages. We conclude the advantages of the proposed algorithm as follows:

(1) The proposed algorithm reduces the computational complexity by transforming the 2D spectral search to twice 1D spectral search.

(2) The proposed algorithm doubles the equivalent frequency sample points and increases the equivalent number of clusters, which can improve the maximum number of detectable signals as well as the estimation accuracy.

(3) The proposed algorithm can obtain higher estimation accuracy compared with some existed algorithms.

5. Simulation Results

In this section, we perform large number of Monte Carlo trials to examine the effectiveness as well as the superiority of the proposed algorithm. The root mean square error (RMSE) of the trials is used to measure the estimation accuracy, which is given by

$$\begin{aligned} \mathrm{RMSE}_{\mathrm{TOA}} &= \frac{1}{L}\sum_{l=1}^{L}\sqrt{\frac{1}{Q}\sum_{q=1}^{Q}\left(\left(\tau_l - \widehat{\tau}_{l,q}\right)^2 + \left(\varsigma_l - \widehat{\varsigma}_{l,q}\right)^2\right)}, \\ \mathrm{RMSE}_{\mathrm{DOA}} &= \frac{1}{L}\sum_{l=1}^{L}\sqrt{\frac{1}{Q}\sum_{q=1}^{Q}\left(\theta_l - \widehat{\theta}_{l,q}\right)^2}, \end{aligned} \tag{36}$$

where Q is the number of Monte Carlo trials and $\widehat{\tau}_{l,q}$, $\widehat{\varsigma}_{l,q}$, and $\widehat{\theta}_{l,q}$ are the estimation result of τ_l, ς_l, and θ_l in the qth trial, respectively. In the following simulations, we set $Q = 500$, $d = 0.09$ m, and $L = 3$ with $\tau = [0.2\,\mathrm{ns}, 0.3\,\mathrm{ns}, 0.4\,\mathrm{ns}]$.

Figures 3 and 4 show the TOA estimation results of the proposed algorithm, where each point represents a trial, $K = 100$, $N = 64$, and the signal-to-noise ratio (SNR) is −10 dB and 10 dB, respectively. As shown in the two figures, the proposed algorithm can successfully obtain the paired TOA estimation results and the estimation accuracy is improved with higher SNR.

Figures 5 and 6, respectively, compare the TOA and DOA estimation accuracy with different number of clusters, where $N = 64$. The simulation results show that the estimation accuracy of both TOA and DOA improves with increased number of clusters.

Figures 7 and 8, respectively, depict the TOA and the DOA estimation performance comparison versus SNR of different algorithms, where $K = 100$ and $N = 64$. It is illustrated clearly that the proposed algorithm can achieve

Table 1: Complexity comparison of different algorithms.

Algorithm	Complexity
Proposed	$O\{2N^2K + 48N^3 - 8N^2(L+2) + 16n_s(N^2+N+1)\}$
2D proposed	$O\{N^2K + 24N^3 - 4N^2(L+2) + 2n_s^2N(2N+1)\}$
Successive PM [24]	$(6K+4L+1)N^2 + 3L^2N + (3L^3+4L+2)(N-1) + 3L^3$ $+2(2N-L)^3 + 4N(2N-L)^2 + 2n_s(2N+1)(2N-L)$
2D-PM [14]	$(6K+4L+1)N^2 + 2L^2N + L^3 + 2(2N-L)^3$ $+4N(2N-L)^2 + n_s^2(2N+1)(2N-L)$
Matrix pencil [19]	$(2K+1)N^2 + (6KL^2+2K)N - 2KL^3$

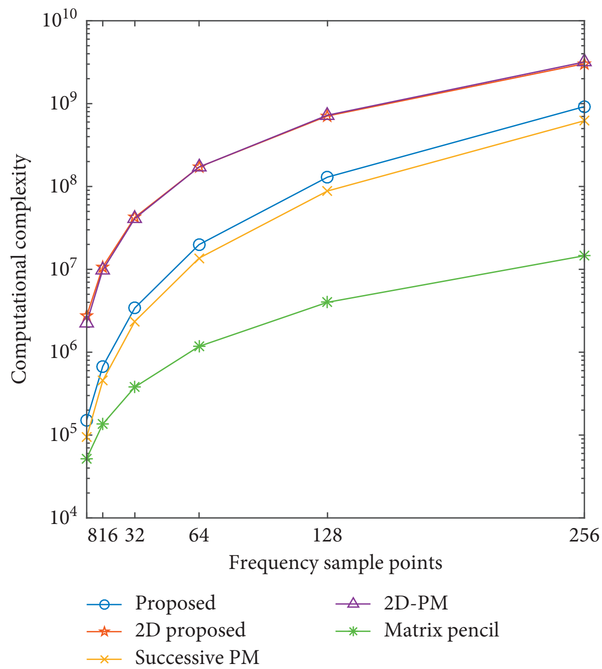

Figure 2: Complexity comparison of different algorithms, where $K = 100$, $L = 3$, and $n_s = 100$.

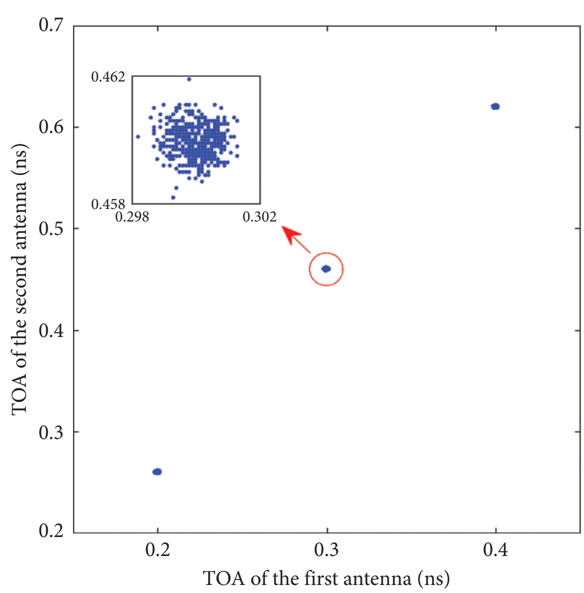

Figure 3: Estimation results of the proposed algorithm, where SNR = −10 dB, $K = 100$, and $N = 64$.

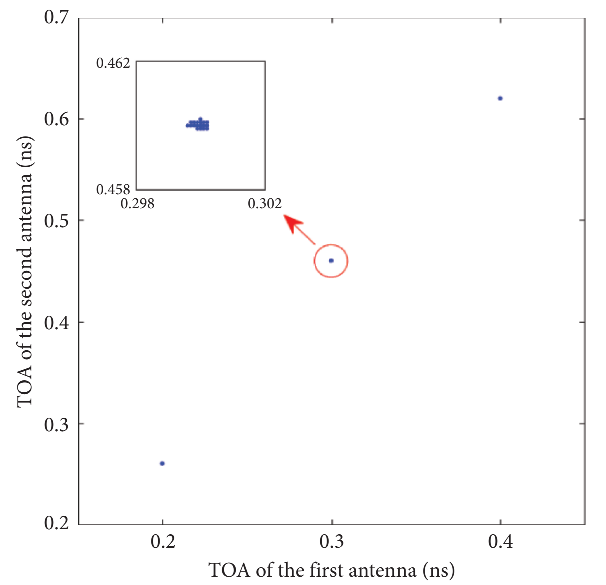

Figure 4: Estimation results of the proposed algorithm, where SNR = 10 dB, $K = 100$, and $N = 64$.

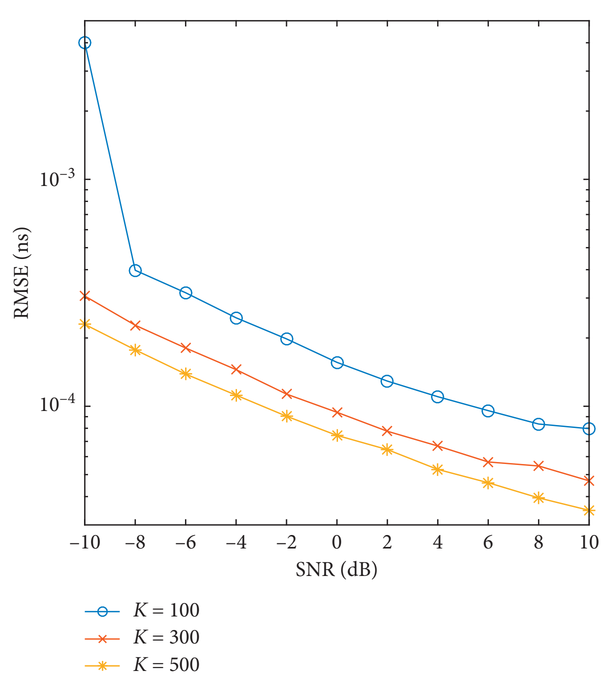

Figure 5: TOA estimation performance of the proposed algorithm in different number of clusters, where $N = 64$.

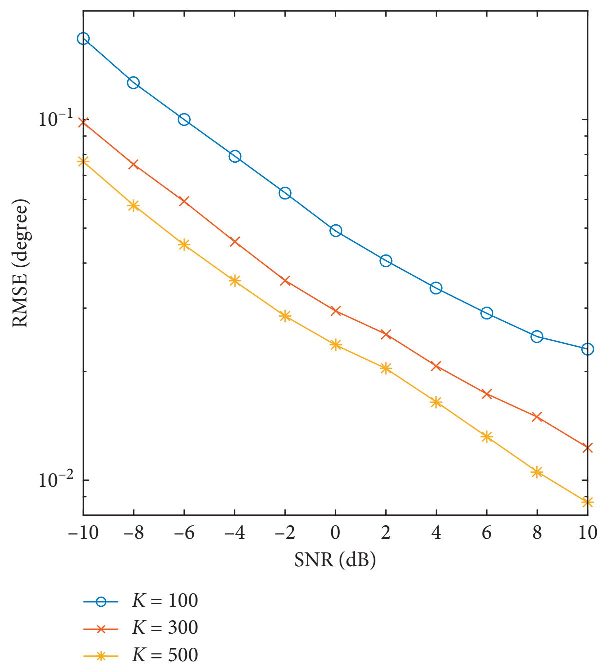

Figure 6: DOA estimation performance of the proposed algorithm in different number of clusters, where $N = 64$.

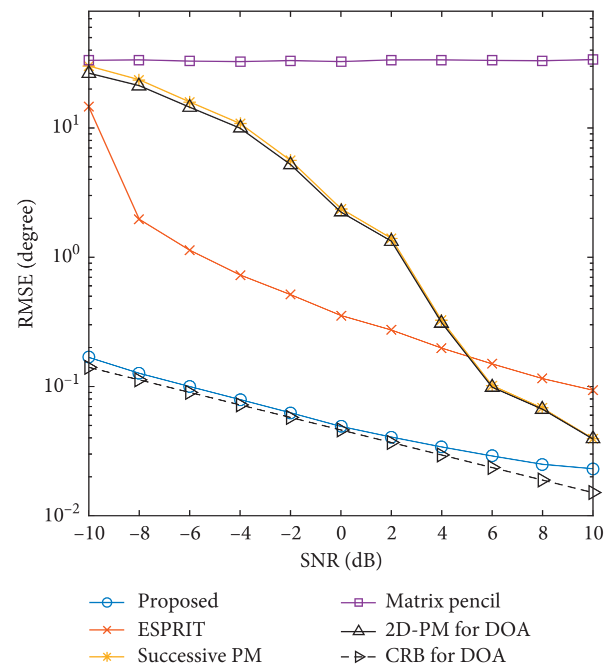

Figure 8: DOA estimation performance comparison of different algorithms, where $K = 100$ and $N = 64$.

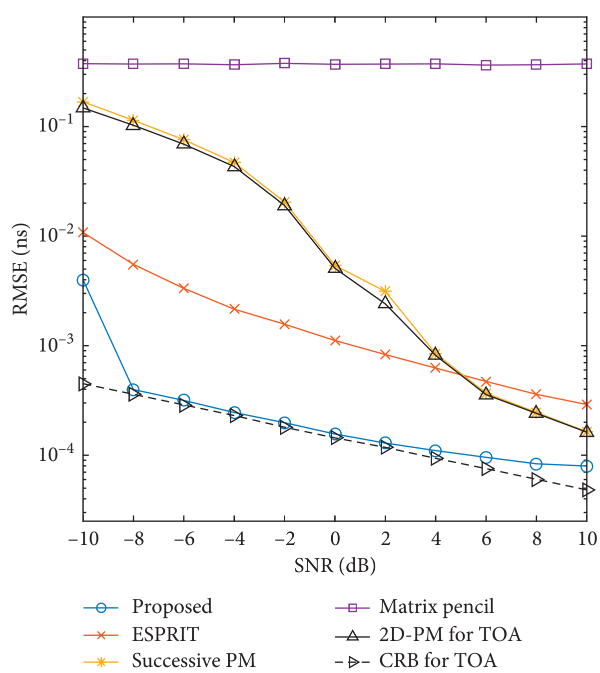

Figure 7: TOA estimation performance comparison of different algorithms, where $K = 100$ and $N = 64$.

better estimation performance in both TOA and DOA domains compared with the ESPRIT algorithm [16], the successive PM [24], the matrix pencil algorithm [19], and the 2D-PM [14].

6. Conclusion

In this paper, we investigate the problem of joint TOA and DOA estimation in UWB systems and propose a computationally efficient algorithm with doubled frequency sample points and extended number of clusters. The proposed algorithm utilizes the conjugate symmetry characteristic of the delay matrices to extend the sample points as well as the number of clusters and then transforms the 2D spectral search into twice 1D search in order to reduce the computational complexity. Simulations testify that the proposed algorithm can obtain high estimation accuracy and large number of identifiable signals with low complexity.

Data Availability

The data used to support the findings of this study are included within the article.

Conflicts of Interest

The authors declare that they have no conflicts of interest.

Acknowledgments

This work was supported by Application of Beidou and Ultra Wideband High Precision Positioning Technology in Ubiquitous Power Internet of Things (51230N19000T).

References

[1] H. Soganci and S. Gezici, "Accurate positioning in ultra-wideband systems," *IEEE Wireless Communications*, vol. 18, no. 2, pp. 19–27, 2011.

[2] J. Rovnakova and D. Kocur, "Short range tracking of moving persons by UWB sensor network," in *Proceedings of the 2011 European Radar Conference (EuRAD)*, pp. 321–324, Manchester, UK, May 2011.

[3] T. Sakamoto and T. Sato, "A target tracking method with a single antenna using time-reversal UWB radar imaging in a multi-path environment," in *Proceedings of the 2010 IEEE International Geoscience and Remote Sensing Symposium (IGARSS)*, pp. 3319–3322, Honolulu, HI, USA, June 2010.

[4] Y. Luo and C. L. Law, "Indoor positioning using UWB-IR signals in the presence of dense multipath with path overlapping," *IEEE Transactions on Wireless Communications*, vol. 11, no. 10, pp. 3734–3743.

[5] M. R. Mahfouz and M. J. Kuhn, "UWB channel measurements and modeling for positioning and communications systems in the operating room," in *Proceedings of the 2011 IEEE Topical Conference on Biomedical Wireless Technologies, Networks, and Sensing Systems (BioWireleSS)*, pp. 47–50, Phoenix, AZ, USA, November 2011.

[6] L. Joon-Yong and R. A. Scholtz, "Ranging in a dense multipath environment using an UWB radio link," *IEEE Journal on Selected Areas in Communications*, vol. 20, no. 9, pp. 1677–1683, 2002.

[7] A. F. Molisch, K. Balakrishnan, C. Chong, et al., IEEE 802.15.4a Channel Model-Final Report, http://www.ieee802.org/15/pub/TG4a.html.

[8] S. Wu, Q. Zhang, R. Fan et al., "Match-filtering based TOA estimation for IR-UWB ranging systems," in *Proceedings of the 2008 International Wireless Communications and Mobile Computing Conference (IWCMA '08)*, pp. 1099–1105, Crete, Greece, August 2008.

[9] I. Guvenc, Z. Sahinoglu, and P. V. Orlik, "TOA estimation for IR-UWB systems with different transceiver types," *IEEE Transactions on Microwave Theory and Techniques*, vol. 54, no. 4, pp. 1876–1886, 2006.

[10] A. A. D'Amico, U. Mengali, and L. Taponecco, "Energy-based TOA estimation," *IEEE Transactions on Wireless Communications*, vol. 7, no. 3, pp. 838–847, 2008.

[11] I. Guvenc and Z. Sahinoglu, "Threshold selection for UWB TOA estimation based on kurtosis analysis," *IEEE Communications Letters*, vol. 9, no. 12, pp. 1025–1027, 2005.

[12] K. Pahlavan, X. Li, and J. P. Makela, "Indoor geolocation science and technology," *IEEE Communications Magazine, Vo.*vol. 40, no. 2, pp. 112–118, 2002.

[13] X. Li and K. Pahlavan, "Super-resolution TOA estimation with diversity for indoor geolocation," *IEEE Transactions on Wireless Communications*, vol. 3, no. 1, pp. 224–234, 2004.

[14] J. Hong, F. Cao, and D. Rui, "Propagator method-based TOA estimation for UWB indoor environment in the presence of correlated fading amplitudes," in *Proceedings of the 2008 4th IEEE International Conference on Circuits and Systems for Communications (ICCSC)*, pp. 535–538, Shanghai, China, May 2008.

[15] F. Zhao, W. Yao, C. C. Logothetis et al., "Comparison of super-resolution algorithms for TOA estimation in indoor IEEE 802.11 wireless LANs," in *Proceedings of the 2006 International Conference on Wireless Communications, Networking and Mobile Computing (WiCOM)*, pp. 1–5, Wuhan, China, October 2006.

[16] H. Saarnisaari, "TLS-ESPRIT in a time delay estimation," in *Proceedings of the IEEE 47th Vehicular Technology Conference*, pp. 1619–1623, Phoenix, Arizona, USA, May 1997.

[17] D. G. Oh, S. H. Jang, J. W. Chong et al., "High resolution TOA estimation algorithm using IEEE 802.15.4a CSS signal," in *Proceedings of the 2008 4th International Conference on Wireless Communications, Networking and Mobile Computing (WiCOM'08)*, pp. 1–3, Dalian, China, October 2008.

[18] D. Rui, Z. Qian, and H. Jiang, "TOA estimation for IR-UWB systems using matrix pencil," *World Congress on Computer Science and Information Engineering*, vol. 1, pp. 461–464, 2009.

[19] D. Rui, Z. Qian, and W. Xue, "Joint TOA and DOA estimation of IR-UWB system based on matrix pencil," *International Forum on Information Technology and Applications (IFITA'09)*, vol. 1, pp. 544–547, 2009.

[20] M. Navarro and M. Najar, "Frequency domain joint TOA and DOA estimation in IR-UWB," *IEEE Transactions on Wireless Communications*, vol. 10, no. 10, pp. 1–11, 2011.

[21] F. Wen, J. Shi, and Z. Zhang, "Closed-form estimation algorithm for EMVS-MIMO radar with arbitrary sensor geometry," *Signal Processing*, vol. 186, pp. 1–9, 2021.

[22] H. Bo and N. C. Beaulieum, "Accurate performance evaluation of time-hopping and direct-sequence UWB systems in multi-user interference," *IEEE Transactions on Communications*, vol. 53, no. 6, pp. 1053–1062, 2005.

[23] A. A. M. Saleh and R. A. Valenzuela, "A statistical model for indoor multipath propagation," *IEEE Journal on Selected Areas in Communications*, vol. 5, no. 2, pp. 128–137, 1987.

[24] F. Wang, X. Zhang, C. Wang et al., "Joint estimation of TOA and DOA if IR-UWB system using a successive propagator method," *International Journal of Electronics*, vol. 102, no. 10, pp. 1765–1788, 2015.

Hindawi
Mathematical Problems in Engineering
Volume 2021, Article ID 5525221, 14 pages
https://doi.org/10.1155/2021/5525221

Research Article

Electromagnetic Vector Sparse Nested Array: Array Structure Design, Off-Grid Parameter Estimation Algorithm

Beizuo Zhu[1,2] **Weiyang Chen**[1,2] **and Luo Chen**[1,2,3]

[1]*College of Electronic and Information Engineering, Nanjing University of Aeronautics and Astronautics, Nanjing 211106, China*
[2]*Key Laboratory of Dynamic Cognitive System of Electromagnetic Spectrum Space (Nanjing University of Aeronautics and Astronautics), Ministry of Industry and Information Technology, Nanjing 211106, China*
[3]*The 28th Research Institute of China Electronics Technology Group Corporation, Nanjing 210007, China*

Correspondence should be addressed to Weiyang Chen; chenweiyang2020@126.com

Received 6 January 2021; Revised 15 February 2021; Accepted 15 March 2021; Published 27 March 2021

Academic Editor: Junpeng Shi

In this paper, a new array structure of sparse nested array (SNA) for electromagnetic vector sensor is designed. An electromagnetic vector sensor is composed of six spatially colocated, orthogonally oriented, diversely polarized antennas, which can measure three-dimensional electric and magnetic field components. By introducing sparse factor (SF) between every adjacent sensor, the proposed SNA has flexibility of extending the array aperture and reducing the mutual coupling effect. Meanwhile, a low-complexity multiparameter estimation algorithm is proposed for SNA. First, the vectorization operation for array manifold ensures the large degrees of freedom for multiparameter estimation, where the initial coarse estimates decrease search range. In addition, the improved off-grid orthogonal matching pursuit method obtains joint direction of arrival (DOA) and polarization estimates with a relatively small overcomplete dictionary because this off-grid method achieves high performance even if the estimates do not fall on the grid of the dictionary. Theoretical analysis and simulation results verify the superiority of the proposed array structure and the algorithm.

1. Introduction

Vector sensors, which are able to detect multiple physical components of the signals, have been widely used in array signal processing [1–3]. Compared with scalar sensor arrays, vector sensor arrays show their advantages in estimation accuracy, recognition accuracy, and antijamming capability [4–6]. Moreover, vector sensor arrays can obtain joint estimates of multiple parameters, such as electromagnetic vector sensor array (EVSA). EVSA can measure DOA and polarization information at the same time because vector sensor structure has the reception access of vector signals.

Resultantly, various DOA and polarization estimation algorithms are proposed for EVSAs, where most of them are inspired by the algorithms for scalar arrays. For example, ESPRIT- (Estimating Signal Parameter via Rotational Invariance Techniques-) based algorithm is proposed in [7, 8], estimating both the arrival angles and the polarizations of incoming narrow-band signals with invariance properties of the EVSA. MUSIC (Multiple Signal Classification) algorithm is also transformed for EVSA in [9], where the joint DOA and polarization estimates are measured by peak search. For alleviating the high computational burden in peak search, a reduced-dimensional MUSIC algorithm is put forward [10], where only two-dimensional peak search is necessary for 4 unknown parameters. In addition, [11] proposes a novel rank reduction method for DOA, range, and polarization estimation, but near-field signal hypothesis is limited.

Meanwhile, some other studies concentrate on the improvement of array structures for EVSAs. The researched algorithms are mainly based on half-wavelength interval arrays, where the array aperture is restricted by the number of sensors and mutual coupling effect has an adverse impact on array performance. Moreover, this kind of array structures has the number of degrees of freedom (DOFs) less than the number of physical sensors, which means that algorithms cannot work when signal numbers are more than sensor numbers. To track the problems, sparse arrays are presented in polarization environment to avoid compact placement and increase the number of DOFs [12–18]. A series of vector cross-product-based algorithms are introduced in [12–14]. This kind of algorithms extracts DOA parameters by performing cross-product to Poynting vector in received signal, which first breaks the limitation of half-wavelength intervals for EVSA. Variable separation MUSIC/MODE algorithm [15] achieves the unambiguous search results for direction of arrivals, which is capable for sparse uniform array structures, but polarization estimation is ignored. The study in [16] applies coprime array in polarization sensors, obtaining joint DOA and polarization estimates with compressed sensing reconstruction algorithm. Due to the vectorization operation for array manifold, the number of DOFs is tremendously increased. In [18], sparse representation (SR) idea is taken for three-parallel coprime EVSA. However, all aforementioned papers focus on the specific array structures and computational burden is relatively high, which is not flexible for different actual engineering requirements.

In this paper, we propose a flexible array structure called sparse nested array (SNA), which can be considered as an improvement of traditional nested array (NA). To be specific, every sensor is equipped with six spatially colocated, orthogonally oriented, diversely polarized antennas, where three cocentered orthogonal electric dipoles and magnetic loops are included. The proposed SNA enjoys flexible sensor interval benefitting from sparse factor (SF) $\delta \geq 1$. The subarrays 1 and 2 in SNA are both uniform linear arrays composed of M and N sensors with intervals $\delta\lambda/2$ $(M+1)\delta\lambda/2$, where λ is the wavelength. The interval between the two subarrays is also $(M+1)\delta\lambda/2$. SF is a positive integer to adjust spacing between sensors overall. By the enlargement of the array aperture, estimation performance is improved and mutual coupling effect is alleviated.

Meanwhile, from the perspective of algorithm, cross-product of the Poynting vector is employed as the coarse DOA initialization. In addition, after using the properties of the covariance matrix to eliminate the polarization parameters, vectorization operation is taken to construct virtual uniform array, which brings about large DOFs of $O(MN)$ with $M+N$ sensors. Then we apply the off-grid orthogonal matching pursuit (OGOMP) algorithm to obtain high-precision multiparameter estimation. Computational complexity is tremendously alleviated because the one-dimensional overcomplete dictionary in OGOMP algorithm is established only around initial DOA estimates. Traditional OMP algorithm [19] requires that all target signals must fall on a preset grid. However, in actual engineering applications, no matter how the grid is divided, it is impossible to ensure that all target signals fall exactly on the grid. When the target signal is off-grid, the estimation performance of the system will be greatly reduced. On the other hand, if the grid is divided too finely, it will cause the system to have too much calculation burden. Moreover, there is not any ambiguous or pairing problem disturbing true values because OGOMP is an ambiguity-free autopaired algorithm.

In short, we summarize the innovations of this paper as follows:

(1) We design a new structure of nested array in EVSA, where six-component electromagnetic vector sensors are equipped, extending array aperture as well as reducing mutual coupling effect. By the vectorization operation of the manifold, high DOFs can be obtained.

(2) We add sparse factor (SF) in every interval of NA, constructing a new array structure called sparse nested array (SNA), which enjoys scaled array aperture and adjustable mutual coupling effect. Meanwhile, the proposed array can maintain the uniqueness of parameter estimates, which aims to be suitable for different engineering scenarios.

(3) We propose a low-complexity off-grid OMP (OGOMP) algorithm to measure joint DOA and polarization estimates. Combined with the off-grid idea that the target signals do not need to just fall on the grid, OGOMP algorithm can use much smaller one-dimensional overcomplete dictionary around initial DOA estimates, tremendously alleviating computational burden as well as performing good estimation performance.

Notations. We use lower-case (upper-case) bold character to denote vector (matrix). $(\cdot)^*$, $(\cdot)^T$, and $(\cdot)^H$ are the conjugate, transpose, and conjugate transpose of a matrix or vector, respectively. $(\cdot)^{-1}$ denotes matrix inverse and $(\cdot)^+$ denotes matrix pseudoinverse. $\oplus$ represents *Hadamard* product. $\otimes$ denotes the *Kronecker* product and $\odot$ represents the *Khatri-Rao* product. $\mathrm{diag}(\cdot)$ symbolizes a diagonal matrix that uses the elements of the matrix as its diagonal element. $\mathrm{abs}(\cdot)$ is absolute value operator and $\mathrm{angle}(\cdot)$ is phase operator. $|\cdot||_1$ denotes 1 norm and $||\cdot||_F$ denotes Frobenius norm.

2. Preliminaries

2.1. Data Model. Consider an array with a certain amount of electromagnetic vector sensors and every sensor herein is equipped with three cocentered orthogonal electric dipoles and magnetic loops, which is shown in Figure 1 [20].

Assume that there are K far-field narrow-band signals impinging on the array with P electromagnetic vector sensors distributed at y-axis with $D_p = d_0 d_p$, $p = 1, 2, \ldots, P$, which is demonstrated in Figure 2.

$d_0 = \lambda/2$ is the unit spacing between adjacent sensors, $d_p \in \mathbb{Z}$, and λ symbolizes the wavelength. The K signals are all completely polarized from yoz plane with incidence angles θ_k, $k = 1, 2, \ldots, K$. The three electric components and magnetic components of the k-th signal at x, y, z-axes are received by the loops and dipoles, which can be represented as [21]

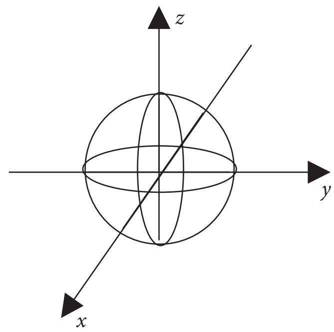

Figure 1: Internal structure of sensor element.

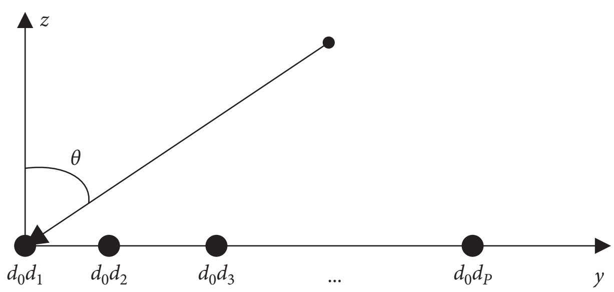

Figure 2: Array model.

$$\mathbf{s}_k = \begin{bmatrix} \mathbf{s}_{ex,k} \\ \mathbf{s}_{ey,k} \\ \mathbf{s}_{ez,k} \\ \mathbf{s}_{hx,k} \\ \mathbf{s}_{hy,k} \\ \mathbf{s}_{hz,k} \end{bmatrix} = \begin{bmatrix} 0 & -1 \\ \cos\theta_k & 0 \\ -\sin\theta_k & 0 \\ -1 & 0 \\ 0 & -\cos\theta_k \\ 0 & \sin\theta_k \end{bmatrix} \begin{bmatrix} \sin\gamma_k e^{j\eta_k} \\ \cos\gamma_k \end{bmatrix} = \mathbf{\Phi}_k \mathbf{\omega}_k, \tag{1}$$

where $\mathbf{s}_{ex,k}, \mathbf{s}_{ey,k}, \mathbf{s}_{ez,k}$ denote the electric components and $\mathbf{s}_{hx,k}, \mathbf{s}_{hy,k}, \mathbf{s}_{hz,k}$ denote the magnetic components of the loops and dipoles. $\mathbf{s}_{e,k} = [\mathbf{s}_{ex,k}, \mathbf{s}_{ey,k}, \mathbf{s}_{ez,k}]$ and $\mathbf{s}_{h,k} = [\mathbf{s}_{hx,k}, \mathbf{s}_{hy,k}, \mathbf{s}_{hz,k}]$ are orthogonal to each other and also to the k-th source's direction of propagation. $\gamma_k \in [0, \pi/2]$ is the auxiliary polarization angle and $\eta_k \in [-\pi, \pi)$ represents the polarization phase difference, respectively. Resultantly, the data model of the received signal at t time can be expressed as [17]

$$\mathbf{x}(t) = (\mathbf{A} \odot \mathbf{S})\mathbf{b}(t) + \mathbf{n}(t) = \mathbf{A}_s \mathbf{b}(t) + \mathbf{n}(t), \tag{2}$$

where $\mathbf{A} = [\mathbf{a}_1, \mathbf{a}_2, \ldots, \mathbf{a}_K]$ is the directional matrix and $\mathrm{a}_k = [e^{jD_1 2\pi \sin\theta_k/\lambda}, \ldots, e^{jD_P 2\pi \sin\theta_k/\lambda}]$ denotes the directional vector for $k-$th signal containing DOA information. $\mathbf{S}_k = [\mathbf{s}_1, \mathbf{s}_2, \ldots, \mathbf{s}_K]$ is the polarization vector matrix, $\mathbf{b}(t) \in C^{J\times 1}$ symbolizes the signal vector, and $\mathbf{n}(t)$ denotes the additive white Gaussian noise complex vector. $\odot$ represents the Khatri–Rao product.

Construct the covariance matrix:

$$\mathbf{R}_s = E\left[\mathbf{x}(t)\mathbf{x}^H(t)\right] = \mathbf{A} \odot \mathbf{S}\left[\mathrm{diag}\left(\sigma_1^2, \sigma_2^2, \ldots, \sigma_K^2\right)\right](\mathbf{A} \odot \mathbf{S})^H, \tag{3}$$

where $E[\cdot]$ denotes the expectation operation. In practice, snapshots J received are finite and they can be approximately calculated by

$$\mathbf{R}_s \approx \frac{1}{J}\sum_{j=1}^{J} \mathbf{x}(t)\mathbf{x}^H(t). \tag{4}$$

Meanwhile, it is also recognized that we can reconstruct the covariance matrix separately according to the six-component received electric and magnetic signals.

$$\begin{aligned} &\begin{cases} \mathbf{R}_{ex} = \mathbf{A}\mathrm{diag}\left(\sigma_1^2 \mathbf{s}_{ex,1}\mathbf{s}_{ex,1}^*, \sigma_2^2 \mathbf{s}_{ex,2}\mathbf{s}_{ex,2}^*, \ldots, \sigma_K^2 \mathbf{s}_{ex,K}\mathbf{s}_{ex,K}^*\right)\mathbf{A}^H \\ \mathbf{R}_{ey} = \mathbf{A}\mathrm{diag}\left(\sigma_1^2 \mathbf{s}_{ey,1}\mathbf{s}_{ey,1}^*, \sigma_2^2 \mathbf{s}_{ey,2}\mathbf{s}_{ey,2}^*, \ldots, \sigma_K^2 \mathbf{s}_{ey,K}\mathbf{s}_{ey,K}^*\right)\mathbf{A}^H, \\ \mathbf{R}_{ez} = \mathbf{A}\mathrm{diag}\left(\sigma_1^2 \mathbf{s}_{ez,1}\mathbf{s}_{ez,1}^*, \sigma_2^2 \mathbf{s}_{ez,2}\mathbf{s}_{ez,2}^*, \ldots, \sigma_K^2 \mathbf{s}_{ez,K}\mathbf{s}_{ez,K}^*\right)\mathbf{A}^H \end{cases} \\ &\begin{cases} \mathbf{R}_{hx} = \mathbf{A}\mathrm{diag}\left(\sigma_1^2 \mathbf{s}_{hx,1}\mathbf{s}_{hx,1}^*, \sigma_2^2 \mathbf{s}_{hx,2}\mathbf{s}_{hx,2}^*, \ldots, \sigma_K^2 \mathbf{s}_{hx,K}\mathbf{s}_{hx,K}^*\right)\mathbf{A}^H \\ \mathbf{R}_{hy} = \mathbf{A}\mathrm{diag}\left(\sigma_1^2 \mathbf{s}_{hy,1}\mathbf{s}_{hy,1}^*, \sigma_2^2 \mathbf{s}_{hy,2}\mathbf{s}_{hy,2}^*, \ldots, \sigma_K^2 \mathbf{s}_{hy,K}\mathbf{s}_{hy,K}^*\right)\mathbf{A}^H, \\ \mathbf{R}_{hz} = \mathbf{A}\mathrm{diag}\left(\sigma_1^2 \mathbf{s}_{hz,1}\mathbf{s}_{hz,1}^*, \sigma_2^2 \mathbf{s}_{hz,2}\mathbf{s}_{hz,2}^*, \ldots, \sigma_K^2 \mathbf{s}_{hz,K}\mathbf{s}_{hz,K}^*\right)\mathbf{A}^H \end{cases} \end{aligned} \tag{5}$$

where $\sigma_k^2, k = 1, 2, \ldots, K$ denotes the power of the k-th signal. By splitting $\mathbf{S}$ and calculating the covariance matrix individually for the six components, we put the polarization information into diag function. Note that

$$\mathbf{s}_{ex,k}\mathbf{s}_{ex,k}^* + \mathbf{s}_{ey,k}\mathbf{s}_{ey,k}^* + \mathbf{s}_{ez,k}\mathbf{s}_{ez,k}^* = 1, \tag{6}$$

$$\mathbf{s}_{hx,k}\mathbf{s}_{hx,k}^* + \mathbf{s}_{hy,k}\mathbf{s}_{hy,k}^* + \mathbf{s}_{hz,k}\mathbf{s}_{hz,k}^* = 1. \tag{7}$$

Consequently, the covariance matrix without polarization information can be obtained.

$$\begin{aligned} \mathbf{R} &= \mathbf{R}_{ex} + \mathbf{R}_{ey} + \mathbf{R}_{ez} = \mathbf{R}_{hx} + \mathbf{R}_{hy} + \mathbf{R}_{hz}, \\ &= \mathbf{A}\mathrm{diag}\left(\sigma_1^2, \cdots, \sigma_K^2\right)\mathbf{A}^H. \end{aligned} \tag{8}$$

2.2. Mutual Coupling. The data model established in Section 2.1 is in the case of free mutual coupling. In actual engineering, there might be serious mutual coupling effect between sensors, especially in adjacent sensors close to each other. The data model considering the influence of mutual coupling is expressed as [22]

$$\mathbf{Y} = [(\mathbf{CA}) \odot \mathbf{S}]\mathbf{B}^T + \mathbf{N}, \tag{9}$$

where $\mathbf{C}$ is a $P \times P$ matrix reflecting interelement coupling (IEC), which is determined by the array manifold. $\mathbf{C}$ can be established according to different criteria. In this paper, B-banded mutual coupling model is employed based on Toeplitz property. Resultantly, mutual coupling matrix $\mathbf{C}$ is defined as

$$\mathbf{C}(i,j)=\begin{cases}0 & \left|d_i-d_j\right|>B\\ c_{\left|d_i-d_j\right|} & \left|d_i-d_j\right|\le B\end{cases},\tag{10}$$

where $c_n = c_1 e^{-j(n-1)\pi/8}/n$, $(2\le n\le B)$ and c_1 is the basic mutual coupling strength with sensor intervals $d_0=\lambda/2$. d_i, d_j, $(1\le i\le P, 1\le j\le P)$ denote the position of the sensor elements. B represents the maximum distance in which mutual coupling takes effect among sensors. Due to the introduction of mutual coupling matrix, a standard of coupling leakage (Γ) can be set for judging the strength of mutual coupling.

$$\Gamma=\frac{\|\mathbf{C}-\mathrm{diag}(\mathbf{C})\|_F}{\|\mathbf{C}\|_F},\tag{11}$$

where $|\cdot\|_F$ denotes Frobenius norm.

Remark 1. Because three orthogonal electric dipoles and magnetic loops in an electromagnetic sensor are designed as a whole part, the interpolarization coupling (IPC) can be measured in application. In this case, we eliminate the influence of IPC in received signal model and only consider the effect of IEC.

3. Array Structure Design

3.1. Sparse Nested Array. The structure of sparse nested array (SNA) is presented in Figure 3. The first subarray, which is marked by black circles, is a uniform linear array with M sensors. The internal spacing between adjacent sensors is δd_0, where $\delta\in\mathbb{N}^+$ is named as sparse factor. The second subarray marked with white squares contains N sensors, which is also a uniform linear array whose interval between sensors is $(M+1)\delta d_0$. The total numbers of sensors are $M+N=P$. Both subarray 1 and subarray 2 lie on y-axis and the M-th sensor in subarray 1 and the first sensor in subarray 2 have the δd_0 interval.

Compared with traditional NA [23], the proposed SNA is developed by the sparse factor δ to unfold sensor interval. It is indicated in Figure 3 that when $\delta=1$, NA is a special case of SNA.

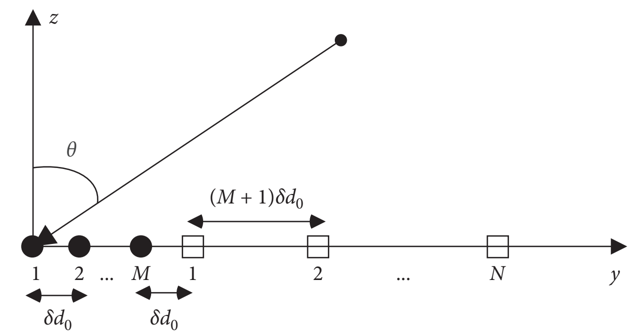

Figure 3: Structure of sparse nested array.

3.2. Interpolation for Virtual Array. According to the basic knowledge of array signal processing, P sensors can achieve $P-1$ degrees of freedom (DOFs). Nevertheless, some sparse arrays can further enlarge DOFs by their equivalent virtual arrays and perform estimation algorithm with the reconstructed virtual signals. In this paper, difference coarray is employed to obtain virtual array of SNA. According to (8), reconstructed covariance matrix $\mathbf{R}$ is a $P\times P$ matrix with DOA information received by the array. By vectorizing the covariance matrix, the equivalent virtual array signals are expressed as [24]

$$\mathbf{z}=\mathrm{vec}(\mathbf{R})=\left(\mathbf{A}^*\odot\mathbf{A}\right)\mathbf{b}_s^T,\tag{12}$$

where $\mathbf{A}^*\odot\mathbf{A}=[\mathbf{a}_1^*\otimes\mathbf{a}_1,\mathbf{a}_2^*\otimes\mathbf{a}_2,\ldots,\mathbf{a}_K^*\otimes\mathbf{a}_\mathbf{K}]\in\mathbb{C}^{P^2\times K}$ denotes the virtual directional matrix. $\mathbf{b}_s=[\sigma_1^2,\ldots,\sigma_K^2]$ is the equivalent one-snapshot signal vector. We can find that the position of virtual sensor element is located at $D\delta$, where

$$D=\left\{d_0\left(d_i-d_j\right)\mid\quad i,j=1,2,\ldots,P\right\}.\tag{13}$$

Obviously, there exist repeated elements in set D. By removing these elements, a unique subset D_u is established. The virtual location of the received signal after vectorization is modeled as

$$D_u=\{d_0d_u\mid-[N\times(M+1)-1]\le d_u\le[N\times(M+1)-1],\ d_u\in\mathbb{Z}\}.\tag{14}$$

Consequently, only the data of $|D_u|=2(N\times(M+1)-1)+1$ rows is necessary for DOA estimation. By selecting the corresponding rows in $\mathbf{z}$, the reconstructed virtual received signals are built using the full DOFs.

$$\mathbf{z}_u=\mathbf{A}_u\mathbf{b}_s^T,\tag{15}$$

where $\mathbf{A}_u=[\mathbf{a}_u(\theta_1),\mathbf{a}_u(\theta_2),\ldots\mathbf{a}_u(\theta_K)]\in\mathbb{C}^{|D_u|\times K}$ is the equivalent virtual array located at $D_u\delta$, which is a uniform linear array, and every adjacent virtual sensor has the interval of δd_0.

3.3. Discussion

3.3.1. Virtual Array Configuration. Compared with coprime array, nested array is a kind of completely augmented array whose virtual array is continuous without holes. Define unit length as half wavelength $\lambda/2$. In order to give an intuitive understanding, we demonstrate the virtual sensor elements of typical coprime array $M=5, N=4$ and nested array $M=N=4$, where $\delta=1$.Both NA and CA have 8 physical sensors because there is a shared sensor for CA. Black circles and white squares denote the physical sensors belonging to the first and second subarrays, respectively. The black crosses represent the virtual sensor elements. From the comparison of Figures 4 and 5, NA has 39 virtual sensor elements and all of them are continuous without holes. Meanwhile, CA only has 27 virtual sensor elements and there are 6 missing elements in $\{-14,-13,-9,9,13,14\}$, which are marked by red crosses. As a result, CA is unable to make full use of information on the whole virtual array, acquiring fewer DOFs and smaller array aperture than NA.

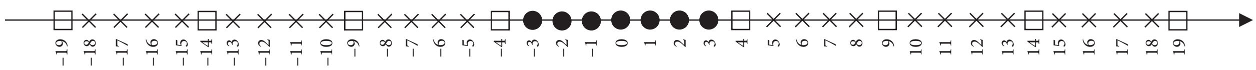

FIGURE 4: Virtual sensor elements of NA. $M = N = 4$.

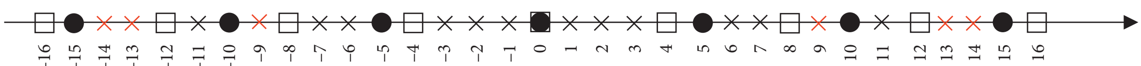

FIGURE 5: Virtual sensor elements of CA. $M = 5$, $N = 4$.

Definition 1 (array aperture). Array aperture is defined as the length of the total linear array, which is one of the criteria evaluating array performance.

3.3.2. Engineering Problems of Sparse Array. According to Section 2, mutual coupling effect decreases exponentially along with the sensor interval. Resultantly, small intervals should be prevented possibly. Sparse arrays, due to the inherent merits of loose array structure, have much lower mutual coupling effect than traditional arrays with half-wavelength intervals. The proposed SNA in this paper solves the problems of compact array structure of NA in the first subarray, as well as providing a relatively flexible array configuration. Moreover, with the increase of sparse factor δ, mutual coupling effect can be further alleviated.

Notation. Although sparse factor provides many gains in array performance, it is not an unlimited number in practice. The three main factors limiting sparse factor are array decorrelation, far-field hypothesis, and grid misidentification. The first two factors are due to actual engineering and the third is due to algorithm limitation. We discuss the factors, respectively, in the following part.

Array decorrelation: suppose that a narrow-band signal is expressed as

$$s(t) = a(t)e^{j[\omega_0 t+\phi(t)]}, \tag{16}$$

where $a(t)$ denotes the slowly varying amplitude modulation function, which is considered abiding during signal reception time, $\omega_0 = 2\pi f_0$ is the carrier frequency, and $\phi(t)$ represents the phase modulation function. Mark the received signal on the array as $[s(t_1), s(t_2), \ldots, s(t_P)]$. The amplitude modulation function must guarantee

$$[\max|a(t)| - \min|a(t)|]/\max|a(t)| < q, \tag{17}$$

where $t \in [t_1, t_2, \ldots, t_P]$ and $0 < q < 1$ depends on actual needs. With the increase of sparse factor, array decorrelation occurs, which will tremendously affect estimation performance.

Far-field hypothesis: we assume that all signals are all from the far field, which satisfy the condition that

$$Z \geq \frac{2\varsigma^2}{\lambda}, \tag{18}$$

where Z denotes the minimum distance from any signal to the array. ς represents the array aperture.

Grid misidentification: this problem often occurs in low signal-to-noise ratio (SNR) environments because the noise generates a much larger phase shift in directional matrix, which may undermine the orthogonality of search algorithms [25]. On the other hand, ESPRIT-based algorithms need ambiguity elimination operations. Arrays with large sparse factor have small grids, which leads to closer ambiguous values. In low SNR, it is easy to mismatch with wrong estimates.

3.4. Performance Analysis. For intuitive comparison, Table 1 lists the DOFs after vectorization operation, array aperture, and mutual coupling effect for SNA, SCA, and traditional uniform linear array (TULA) [26] with all 8 physical sensors. For simplicity, label $\lfloor a, b, c, d, e \rfloor$ is utilized to indicate that subarray 1 has a sensors with $b\delta d_0$ intervals and subarray 2 has c sensors with $d\delta\ d_0$ intervals and e denotes the number of sparse factors δ.

It is revealed in Table 1 that both nested array and coprime array outperform traditional uniform linear array. By enlarging sparse factor or increasing the number of physical sensors, SNA and SCA achieve larger array aperture and lower mutual coupling. Meanwhile, NA has more DOFs and extended array aperture than CA with the same physical sensors.

4. DOA and Polarization Estimation Algorithm

Orthogonal matching pursuit (OMP) algorithm is considered as a typical compressed sensing method to obtain DOA estimates. However, an overcomplete dictionary is necessary for orthogonal verification, which takes relatively high computational complexity. Moreover, orthogonal verification is essentially a searching process, where grid density affects both estimation accuracy and computational burden. The two indexes check and balance with each other. Off-grid orthogonal matching pursuit (OGOMP) solves off-grid problem and guarantees good performance. Based on the scalar OGOMP algorithm [27], we propose a low-complexity DOA and polarization estimation algorithm for SNA, which mainly includes DOA initialization and accurate DOA and polarization estimation.

4.1. Initial DOA Estimation. According to the covariance matrix $\mathbf{R}_s$, eigendecomposition can be performed to obtain signal subspace $\mathbf{E}_s \in \mathbb{C}^{6(M+N)\times K}$. On the other hand, the first to $(M-1)$-th sensors have rotation invariance with the second to M-th sensors in subarray 1 and the first to $(N-1)$-th sensors have rotation invariance with the second to N-th sensors in subarray 2. Therefore, we can decompose the signal subspace $\mathbf{E}_s$.

Table 1: Performance for different arrays.

	SNA $\lfloor 3, 1, 5, 4, 1 \rfloor$	SNA $\lfloor 3, 1, 5, 4, 2 \rfloor$	SNA $\lfloor 3, 1, 5, 4, 3 \rfloor$	SNA $\lfloor 3, 1, 3, 4, 2 \rfloor$	SCA $\lfloor 4, 5, 5, 4, 2 \rfloor$	SCA $\lfloor 4, 5, 5, 4, 3 \rfloor$	SCA $\lfloor 4, 3, 3, 4, 2 \rfloor$	TULA
DOFs	38	38	38	22	16	16	12	7
Array aperture	38	76	114	44	64	96	36	7
Γ	0.2880	0.1465	0.0946	0.1660	0.1349	0.0904	0.1513	0.4197

$$\begin{aligned}
\mathbf{E}_{s1} &= \mathbf{E}_s[1:\ 6(M-1)],\\
\mathbf{E}_{s2} &= \mathbf{E}_s[7:\ 6M],\\
\mathbf{E}_{s3} &= \mathbf{E}_s[6M+1:\ 6(M+N-1)],\\
\mathbf{E}_{s4} &= \mathbf{E}_s[6M+7:\ 6(M+N)],
\end{aligned} \tag{19}$$

where $\mathbf{E}_s[a\colon b]$ represents the line a to b of $\mathbf{E}_s$. By eigendecomposition of $\mathbf{E}_{s1}{}^{+}\mathbf{E}_{s2}$ and $\mathbf{E}_{s3}{}^{+}\mathbf{E}_{s4}$, eigenvectors $\mathbf{T}_{12}, \mathbf{T}_{34}$ and eigenvalues $\mathbf{v}_{12} = [e^{j\delta d_0 2\pi \sin\theta_1/\lambda}, \ldots, e^{j\delta d_0 2\pi \sin\theta_K/\lambda}]$ and $\mathbf{v}_{34} = [e^{j(M+1)\delta d_0 2\pi \sin\theta_1/\lambda}, \ldots, e^{j(M+1)\delta d_0 2\pi \sin\theta_K/\lambda}]$ can be calculated, where the eigenvectors are nonsingular $K\times K$ matrices with full rank. We employ a vital characteristic in array signal processing [7].

$$\mathbf{E}_s = \mathbf{A}_s\mathbf{T}. \tag{20}$$

Thus, the estimate $\mathbf{A}_s$ is measured by

$$\mathbf{A}_s = \left\{\begin{matrix} \mathbf{E}_s[1:\ 6M]\mathbf{T}_{12}^{-1} \\ \mathbf{E}_s[6M+1:\ 6(M+N)]\mathrm{T}_{34}^{-1} \end{matrix}\right\}. \tag{21}$$

The next step is extracting the DOA parameters from $\mathbf{A}_s = [\mathbf{a}_1\otimes\mathbf{s}_1, \mathbf{a}_2\otimes\mathbf{s}_2, \ldots, \mathbf{a}_K\otimes_K]$ as the initial estimation results. Here, we eliminate the directional matrix $\mathbf{A} = [\mathbf{a}_1, \mathbf{a}_2, \ldots, \mathbf{a}_K]$ by $\mathbf{v}_{12}, \mathbf{v}_{34}$ to estimate the polarization vector matrix $\widehat{S} = [\mathbf{s}_1, \mathbf{s}_2, \ldots, \mathbf{s}_K]$, which is expressed as

$$\begin{aligned}
\mathbf{s}_k = {}& \frac{1}{2M}\sum_{i=1}^{M}\frac{\mathbf{A}_{s,k}[6(i-1)+1:\ 6i]}{\|\mathbf{A}_{s,k}[6(i-1)+1:\ 6i\|_1}\left(\mathbf{v}_{12}^{[k]}\right)^{-j(i-1)}\\
&+\frac{1}{2N}\sum_{i=1}^{N}\frac{\mathbf{A}_{s,k}[6M+6(i-1)+1:\ 6M+6i]}{\|\mathbf{A}_{s,k}[6M+6(i-1)+1:\ 6M+6i\|_1}\left(\mathbf{v}_{34}^{[k]}\right)^{-j(i-1)},
\end{aligned} \tag{22}$$

where $\mathbf{A}_{s,k}$ denotes the k – th row of $\mathbf{A}_{s,k}$ and $\mathbf{v}^{[k]}$ is the k-th element of $\mathbf{v}$. As is revealed in (22), each term on the right side of the equation is an estimate of $\mathbf{s}_k$, which uses up the full information of $\mathbf{A}_s$ to get more precise results.

According to (1), the normalized Poynting vector $\mathbf{P}_k$ can be estimated with vector cross-product estimator, which is expressed as [15]

$$\mathbf{P}_k = \begin{bmatrix}\mathbf{P}_{x,k}\\ \mathbf{P}_{y,k}\\ \mathbf{P}_{z,k}\end{bmatrix} = \mathbf{s}_{e,k}\times\mathbf{s}_{h,k} = \begin{bmatrix}0\\ \sin\theta\\ \cos\theta\end{bmatrix}, \tag{23}$$

where only DOA information is involved in $\mathbf{P}_k$. Based on the analysis above, we can obtain the coarse initial DOA estimates.

$$\widehat{\theta}_{k,ini} = \frac{1}{2}\left[\arcsin\mathbf{P}_k^{[2]} + \arccos\mathbf{P}_k^{[3]}\right], \tag{24}$$

where $\mathbf{P}^{[i]}$ denotes the i-th element of $\mathbf{P}$.

4.2. Precise DOA Estimation with Low Complexity. In this part, we propose an off-grid OMP (OGOMP) algorithm, which can obtain accurate joint DOA and polarization estimates.

First, we can establish an overcomplete dictionary partly taken from $\mathbf{A}_u$:

$$\mathbf{Q}(\theta) = \left[\mathbf{a}_u(\theta_1), \mathbf{a}_u(\theta_2), \ldots, \mathbf{a}_u(\theta_Q)\right] \in \mathbb{C}^{|D_u|\times Q},\ Q\gg K, \tag{25}$$

where the angular interval is $r = \theta_{i+1}-\theta_i$, $1\le i\le Q-1$ and θ_i is near the initial DOA estimates. Define a deviation vector $\xi\in\mathbb{R}^{Q\times 1}$ and every element $-r/2\le\xi_q\le r/2$, $q=1,2,\ldots,Q$ refers to the deviation with grid. The directional vector after grid division will be close to the directional vector of the actual target signal with the first-order Taylor expansion principle, which can be expressed as

$$\mathbf{a}_{ut}(\theta_i+\xi_i) \approx \mathbf{a}_u(\theta_i) + \frac{\partial\mathbf{a}_u(\theta_i)}{\partial\theta_i}\xi_i, \quad i=1,2,\ldots,Q, \tag{26}$$

where $\mathbf{a}_u(\theta_i)$ denotes the directional vector of θ_i in overcomplete dictionary corresponding to virtual array manifold after vectorization and $\partial(\cdot)$ represents the partial derivative. Therefore,
$\mathbf{Q}_t = [\mathbf{a}_{ut}(\theta_1+\xi_1), \mathbf{a}_{ut}(\theta_2+\xi_2), \ldots, \mathbf{a}_{ut}(\theta_Q+\xi_Q)]$ can be regarded as the sum of two matrices.

$$\mathbf{Q}_t = \mathbf{Q} + \mathbf{\Theta}\mathbf{\Lambda}, \tag{27}$$

where $\Theta(\theta) = [\partial\mathbf{a}_u(\theta_1)/\partial\theta_1, \partial\mathbf{a}_u(\theta_2)/\partial\theta_2, \ldots, \partial\mathbf{a}_u(\theta_Q)/\partial\theta_Q]$ and $\Lambda = \mathrm{diag}(\xi)$.

Since the vectorized received signal $\mathbf{z}_u$ is only associated with DOA information, we construct the following function to verify the orthogonality:

$$P = \max\sqrt{\left|\mathbf{Q}(\theta_i)\mathbf{z}_u\right|^2 + \left|\mathbf{\Theta}(\theta_i)\mathbf{z}_u\right|^2}, \quad i=1,2,\ldots,Q. \tag{28}$$

When $\theta_i+\xi_i$ approaches the true incident angle, (28) achieves a peak value. Compared with (27), (28) still has orthogonality without Λ because the vectorized received signal can also be represented as

$$\mathbf{z}_u = (\mathbf{Q}+\mathbf{\Theta}\mathrm{diag}(\boldsymbol{\xi}))\mathbf{H}_s^T = \mathbf{Q}\mathbf{H}_s^T + \mathbf{\Theta}\left(\boldsymbol{\xi}\oplus\mathbf{H}_s^T\right), \tag{29}$$

where $\mathbf{H}_s^T$ denotes sparse signal vector with k nonzero values. It can be indicated from (29) that if Θ is orthogonal to the q – th element $\mathbf{H}_s^{T\,[q]}$, it is also orthogonal to $(\Lambda\mathbf{H}_s^T)^{[q]}$, $q=1,2,\ldots,Q$.

After the first search around initial DOA estimates, we construct $\widetilde{A} = [\mathbf{a}_u(\theta_{m_1}), \partial\mathbf{a}_u(\theta_{m_1})/\partial\theta_{m_1}]$ from $\mathbf{Q}$ and Θ corresponding to $\max(P)$. Thus, according to (29), least-squares criterion is employed to estimate $\mathbf{H}_s^{T\,[m_1]}$ and $(\Lambda\mathbf{H}_s^T)^{[m_1]}$, which is expressed as

$$\begin{bmatrix}\mathbf{H}_s^{T\,[m_1]}\\ \left(\mathbf{\Lambda}\mathbf{H}_s^T\right)^{[m_1]}\end{bmatrix} = \left(\widetilde{A}\widetilde{A}^H\widetilde{A}\widetilde{A}\right)^{-1}\widetilde{A}\widetilde{A}^H\mathbf{z}_u. \tag{30}$$

The other $K-1$ signals are also measured by (28). In particular, the rows in $\mathbf{z}_u$ corresponding to $\theta_{m_1}, \theta_{m_2}, \cdots, \theta_{m_k}$ which have been estimated should be removed. Hence, the virtual received signal $\mathbf{z}_u$ is updated:

$$\mathbf{z}_u = \mathbf{z}_u - \sum_{i=1}^{k}\left[\mathbf{a}_u(\theta_{m_i}), \frac{\partial \mathbf{a}_u(\theta_{m_i})}{\partial \theta_{m_i}}\right]\left[\begin{array}{c}\mathbf{H}_s^{T\ [m_i]} \\ \left(\mathbf{\Lambda}\mathbf{H}_s^T\right)^{[m_i]}\end{array}\right]. \tag{31}$$

The maximum value in each search corresponds to an incident angle. Eliminating sparse signal vector $\mathbf{H}_s^{T\ [m_k]}$, ξ_{m_k}, $k = 1, 2, \ldots, K$ can be computed by (30). The accurate and ambiguity-free DOA estimates are obtained with K iterations.

$$\widehat{\theta}_{k,est} = \theta_{mk} + \xi_{m_k},\ k = 1, 2, \ldots, K. \tag{32}$$

4.3. Polarization Estimation. Inspired from (5), we can also construct a cross-correlation covariance matrix among the 6 electric and magnetic components. We focus on two combinations: electric components of the x-axis and z-axis and magnetic components of the x-axis and z-axis.

$$\mathbf{R}_{ex,ez} = \mathbf{A}\mathrm{diag}\left(\sigma_1^2 \mathbf{s}_{ex,1}\mathbf{s}_{ez,1}^*, \sigma_2^2 \mathbf{s}_{ex,2}\mathbf{s}_{ez,2}^*, \ldots, \sigma_K^2 \mathbf{s}_{ex,K}\mathbf{s}_{ez,K}^*\right)\mathbf{A}^H, \tag{33}$$

$$\mathbf{R}_{hx,ez} = \mathbf{A}\mathrm{diag}\left(\sigma_1^2 \mathbf{s}_{hx,1}\mathbf{s}_{ez,1}^*, \sigma_2^2 \mathbf{s}_{hx,2}\mathbf{s}_{ez,2}^*, \ldots, \sigma_K^2 \mathbf{s}_{hx,K}\mathbf{s}_{ez,K}^*\right)\mathbf{A}^H. \tag{34}$$

Performing vectorization operation similar to Section 3.2, (33) and (34) are transformed to

$$\begin{aligned}\mathbf{r}_{ex,ez} &= \mathbf{A}^* \odot \mathbf{A}\left[\sigma_1^2 \mathbf{s}_{ex,1}\mathbf{s}_{ez,1}^*, \sigma_2^2 \mathbf{s}_{ex,2}\mathbf{s}_{ez,2}^*, \ldots, \sigma_K^2 \mathbf{s}_{ex,K}\mathbf{s}_{ez,K}^*\right]^T \\ &= \mathbf{A}^* \odot \mathbf{A}\mathbf{S}_{ex,ez}, \\ \mathbf{r}_{hx,ez} &= \mathbf{A}^* \odot \mathbf{A}\left[\sigma_1^2 \mathbf{s}_{hx,1}\mathbf{s}_{ez,1}^*, \sigma_2^2 \mathbf{s}_{hx,2}\mathbf{s}_{ez,2}^*, \ldots, \sigma_K^2 \mathbf{s}_{hx,K}\mathbf{s}_{ez,K}^*\right]^T \\ &= \mathbf{A}^* \odot \mathbf{A}\mathbf{S}_{hx,ez},\end{aligned} \tag{35}$$

where $\mathbf{A}$ can be computed by DOA estimates. $\mathbf{S}_{ex,ez} = [\sigma_1^2 \mathbf{s}_{ex,1}\mathbf{s}_{ez,1}^*, \sigma_2^2 \mathbf{s}_{ex,2}\mathbf{s}_{ez,2}^*, \ldots, \sigma_K^2 \mathbf{s}_{ex,K}\mathbf{s}_{ez,K}^*]^T$ and $\mathbf{S}_{hx,ez} = [\sigma_1^2 \mathbf{s}_{hx,1}\mathbf{s}_{ez,1}^*, \sigma_2^2 \mathbf{s}_{hx,2}\mathbf{s}_{ez,2}^*, \ldots, \sigma_K^2 \mathbf{s}_{hx,K}\mathbf{s}_{ez,K}^*]^T$. The cross-correlation covariance matrices after vectorization operation still contain polarization information, which provides a basis for polarization estimation. Least-squares criterion is utilized as

$$\begin{aligned}\mathbf{S}_{ex,ez} &= \left(\mathbf{A}^H\mathbf{A}\right)^+ \mathbf{A}^H \mathbf{r}_{ex,ez}, \\ \mathbf{S}_{hx,ez} &= \left(\mathbf{A}^H\mathbf{A}\right)^+ \mathbf{A}^H \mathbf{r}_{hx,ez}.\end{aligned} \tag{36}$$

According to the definition in (1), auxiliary polarization angle and polarization phase difference estimates are obtained by eliminating the power of signals.

$$\begin{aligned}\widehat{\gamma}_{k,est} &= \arctan\left[\mathrm{abs}\left(\frac{\mathbf{S}_{hx,ez}^{[k]}}{\mathbf{S}_{ex,ez}^{[k]}}\right)\right], \\ \widehat{\eta}_{k,est} &= -\mathrm{angle}\left(\frac{\mathbf{S}_{ex,ez}^{[k]}}{\mathbf{S}_{hx,ez}^{[k]}}\right),\end{aligned} \tag{37}$$

where $k = 1, 2, \ldots, K$.

4.4. Discussion. The proposed algorithm aims to jointly estimate DOA and polarization parameters with low complexity. There are mainly two steps where computational burden is effectively reduced. The first is the DOA initialization during which only eigendecomposition approach is used. Thus, coarse initial DOA estimates are obtained. Benefitting from that, we require no global overcomplete dictionary for orthogonal verification. The second step is reducing the dimensions of overcomplete dictionary from three to one because the two polarization parameters are both eliminated by the construction of the new covariance matrix $\mathbf{R}$ and the process of OGOMP algorithm is only related to DOA. In addition, benefitting from OGOMP algorithm, not only is the accuracy guaranteed but also the search interval is not strictly required. When the incident angle is not involved in the dictionary, estimation performance can also be guaranteed.

The process of the DOA and polarization estimation is summarized as follows:

Step 1: compute the estimates of $\mathbf{A}_s$ by eigendecomposition of $\mathbf{R}_s$

Step 2: eliminate polarization information from $\mathbf{A}_s$ with vector cross-product estimator

Step 3: obtain coarse DOA initial estimates in normalized Poynting vector

Step 4: search in partly overcomplete dictionary with OGOMP algorithm for accurate DOA estimates

Step 5: construct cross-correlation covariance matrix, perform vectorization operation, and obtain polarization estimates by least-square criterion

The main complexity of the proposed algorithm is discussed as follows.

Constructing the covariance matrix requires $O\{J(6P)^2 + 8JP^2\}$. The computational burden of DOA initialization involves the eigendecomposition which takes $O\{(6P)^3 + 2K^3\}$. OGOMP algorithm is composed of the search over the one-dimensional dictionary for K iterations, which mainly requires $O\{K2Q|D_u|\}$. In summary, the proposed algorithm approximately needs the complexity of only $O\{J(6P)^2 + 8JP^2 + (6P)^3 + 2K^3 + K2Q|D_u|\}$. However, the traditional search-based algorithms cannot avoid three-dimensional search for three unknown parameters and the search range is relatively large compared with the proposed algorithm, which is exhaustive and infeasible.

5. Simulation Results

We perform some simulations in order to confirm the superior performance of the proposed SNA and the OGOMP-based algorithm. This section is divided into 4 parts. Part A verifies the large DOFs of SNA by scatter plot. Part B demonstrates the effectiveness of SF versus SNR and snapshots. We also compare the proposed algorithm with OMP, ESPRIT, and PM algorithms to outstand the prominent performance of the proposed algorithm in part C. Moreover, considering the different coupling leakage in different arrays, part D simulates the performance for

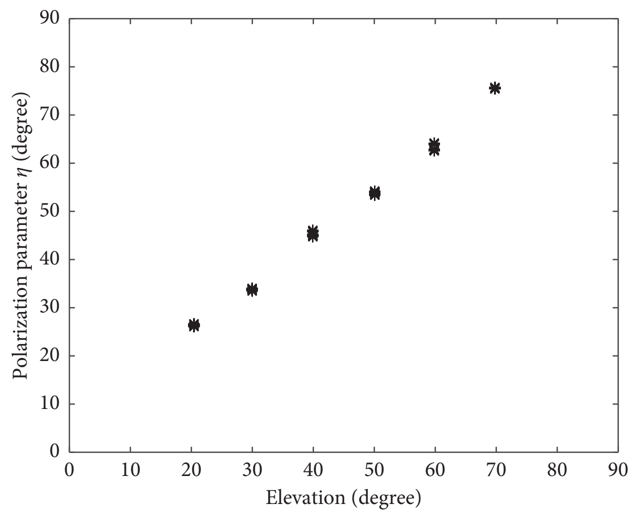

Figure 6: Scatter plot of θ and η estimation results.

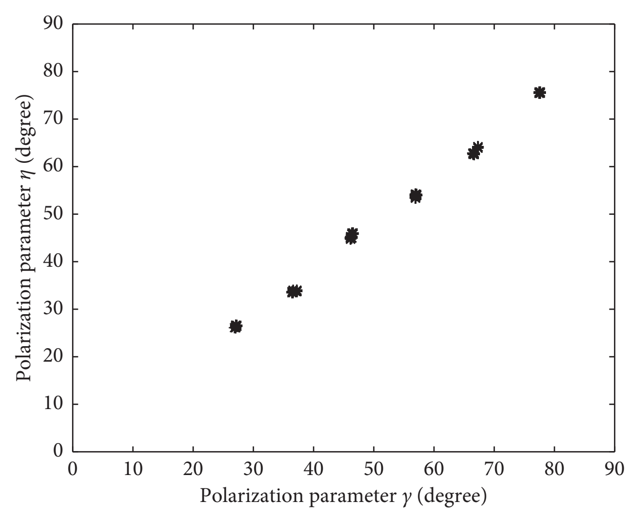

Figure 7: Scatter plot of γ and η estimation results.

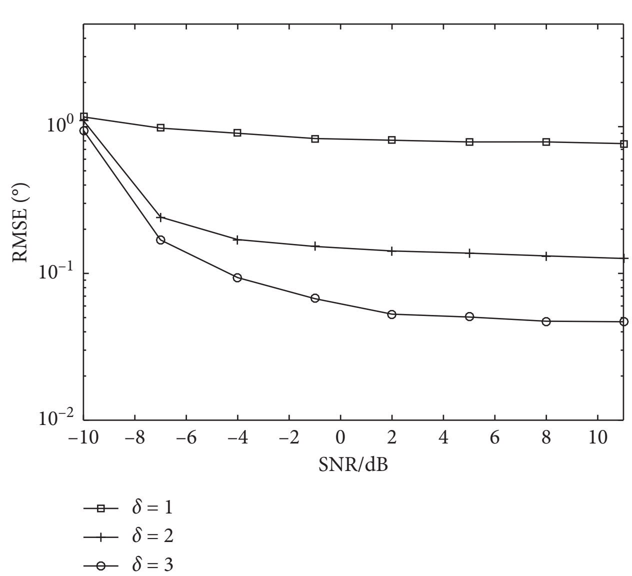

Figure 8: DOA estimation performance versus SF (SNR).

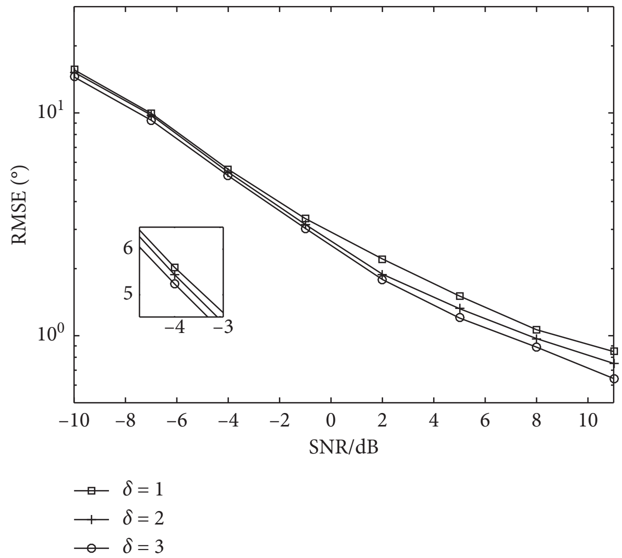

FIGURE 9: γ estimation performance versus SF (SNR).

different array structures with mutual coupling effect. During the above simulations, root mean square error (RMSE) is employed to evaluate the performance, which is defined as

$$\mathrm{RMSE}_a = \frac{1}{K}\sum_{k=1}^{K}\sqrt{\frac{1}{I}\sum_{i=1}^{I}\left[\left(\widehat{\theta}_{k,i}-\theta_k\right)^2\right]},$$
$$\mathrm{RMSE}_\gamma = \frac{1}{K}\sum_{k=1}^{K}\sqrt{\frac{1}{I}\sum_{i=1}^{I}\left[\left(\widehat{\gamma}_{k,i}-\gamma_k\right)^2\right]}, \tag{38}$$
$$\mathrm{RMSE}_\eta = \frac{1}{K}\sum_{k=1}^{K}\sqrt{\frac{1}{I}\sum_{i=1}^{I}\left[\left(\widehat{\eta}_{k,i}-\eta_k\right)^2\right]},$$

where $\widehat{\theta}_{k,i}$, $\widehat{\gamma}_{k,i}$, and $\widehat{\eta}_{k,i}$ are the estimated values of θ_k, γ_k, and η_k during the $i-$th simulation, and I is the number of independent simulations. In this paper, we assume that signal number K has been estimated and there are 3 signals impinging on the array in simulation parts B, C, and D with DOA and polarization parameters $(\theta_1,\gamma_1,\eta_1)=(20°, 27°, 25°)$, $(\theta_2,\gamma_2,\eta_2)=(30°,37°,35°)$, and $(\theta_3,\gamma_3,\eta_3)=(40°,57°,55°)$.

5.1. Independent DOA and Polarization Estimation. As is analyzed in Section 3, the proposed algorithm can estimate signals equal to or more than physical sensor elements benefitting from the SNA array structure and the vectorization operation. Figures 6 and 7 exhibit the scatter plot of the estimate pairs with 100 independent experiments. The physical sensor elements are 5 with array structure SNA $\lfloor 2,1,3,3,2\rfloor$, whereas there are 6 signals with DOA and polarization parameters $(\theta_1,\gamma_1,\eta_1)=(20°,27°,25°)$, $(\theta_2,\gamma_2,\eta_2)=(30°,37°,35°)$, $(\theta_3,\gamma_3,\eta_3)=(40°,47°,45°)$, $(\theta_4,\gamma_4,\eta_4)=(50°,57°,55°)$, $(\theta_5,\gamma_5,\eta_5)=(60°,67°,65°)$, and $(\theta_6,\gamma_6,\eta_6)=(60°,77°,75°)$, where $J=1000$ and SNR $=20\ dB$. As is depicted in the figures, all 6 signals are estimated accurately without any missing or error signal, which verifies advantages of large DOFs. Besides, the DOA and the two polarization parameters are autopaired, indicating that no extra pairing operation is needed.

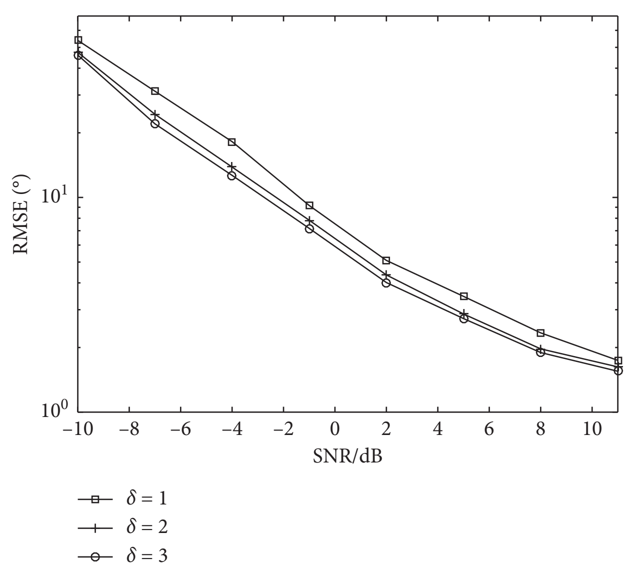

FIGURE 10: η estimation performance versus SF (SNR).

5.2. Parameter Estimation Performance Comparison versus SF. In this part, we perform the SF simulation for SNA $\lfloor 3,1,3,4,\delta\rfloor$ with the proposed algorithm. Figures 8–10 demonstrate the RMSE performance for DOA and polarization parameters along with SNR, where $J=200$, and Figures 11–13 depict the RMSE performance based on different snapshots, where SNR $=0\ dB$. As is revealed in the

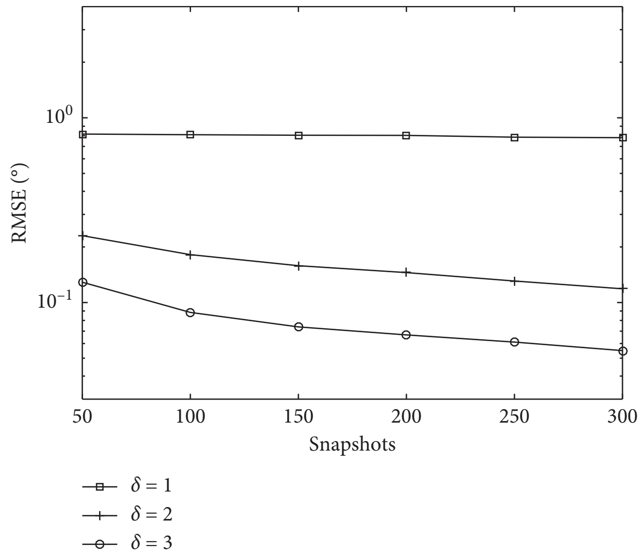

FIGURE 11: DOA estimation performance versus SF (snapshots).

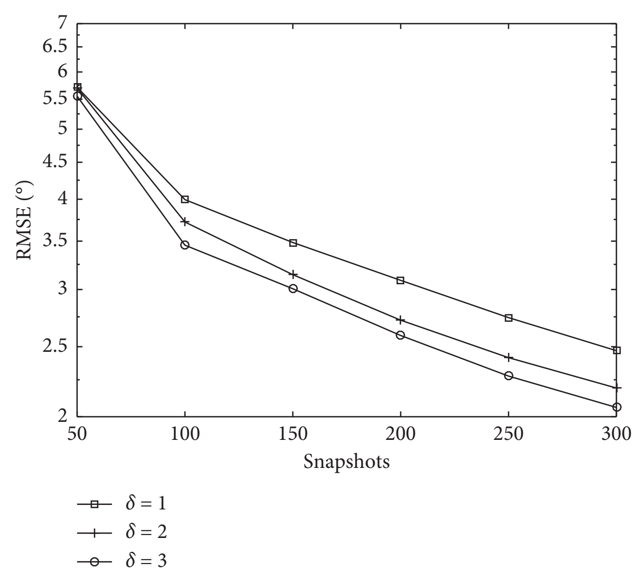

FIGURE 12: γ estimation performance versus SF (snapshots).

figures, RMSE decreases not only with the improvement of SNR and snapshots but also accompanied by the enlargement of SF. From the overall perspective, the RMSE of DOA is much lower than the two polarization parameters.

5.3. Parameter Estimation Performance Comparison for Algorithms. Figures 14–16 compare the proposed algorithm with OMP, Propagator Method (PM) [28], and Estimating Signal Parameter via Rotational Invariance Techniques (ESPRIT), where snapshots $J = 200$ and SNR $= [-10, 11]dB$. In addition, Cramér-Rao Bound (CRB) [29] is presented as the standard.

The array structure is SNA $\lfloor 3, 1, 3, 4, 2 \rfloor$. The dictionary intervals are all 0.1° for OGOMP, OMP, and PM algorithms.

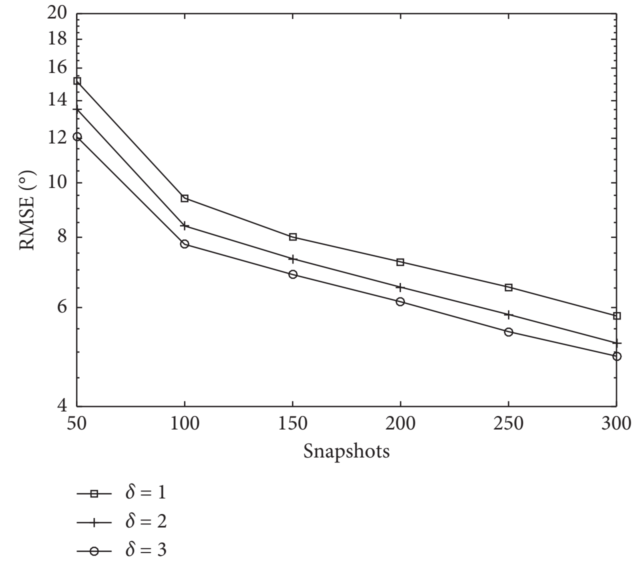

FIGURE 13: η estimation performance versus SF (snapshots).

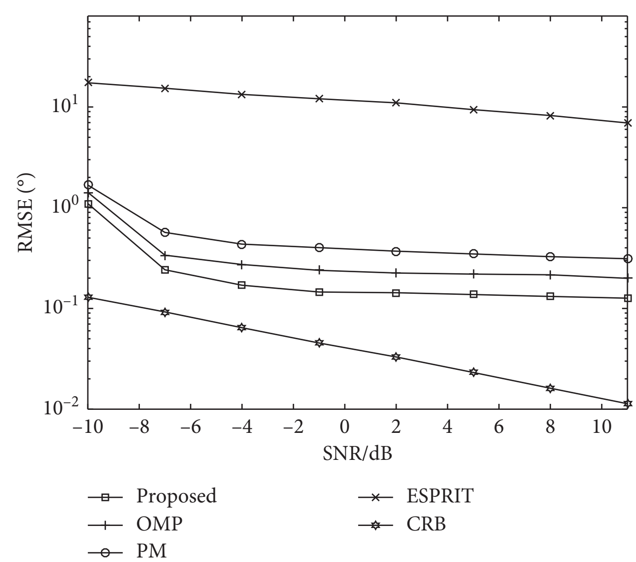

FIGURE 14: DOA estimation performance under different algorithms.

As revealed in the figures, the proposed algorithm outperforms the other three algorithms. Specifically, OMP algorithm ignores any possible incident angle outside the dictionary, which degrades the performance. PM requires no eigendecomposition but employs the search function with poor orthogonality. ESPRIT performs the worst because there are not enough sensors so that signal subspace matrix has insufficient information for DOA estimates. Simultaneously, the polarization estimates are also affected.

5.4. Parameter Estimation Performance Comparison for Array Structures. Since mutual coupling effect is varying for different array structures, we consider the coupling leakage in

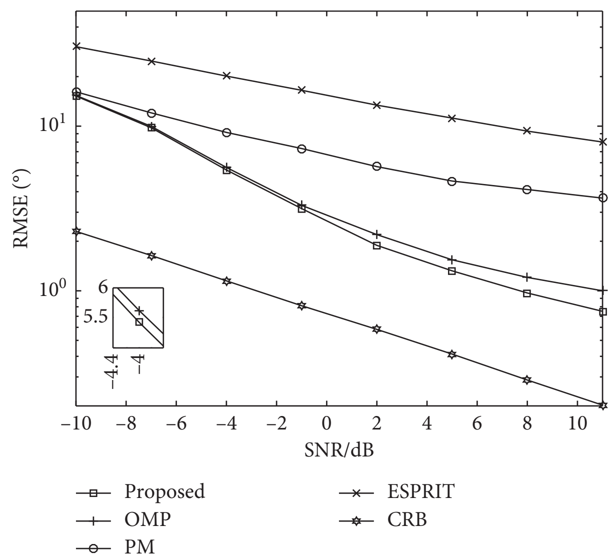

Figure 15: γ estimation performance under different algorithms.

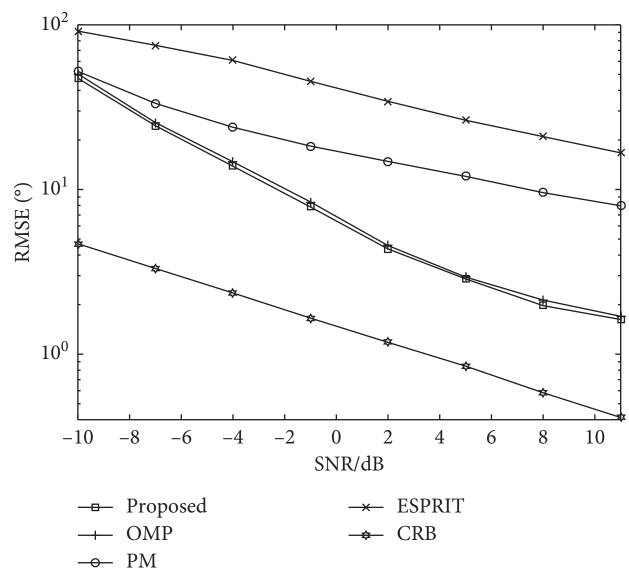

Figure 16: η estimation performance under different algorithms.

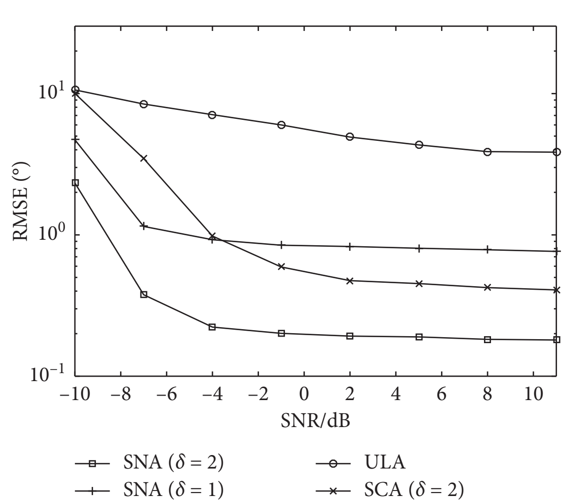

Figure 17: DOA estimation performance with different array structures.

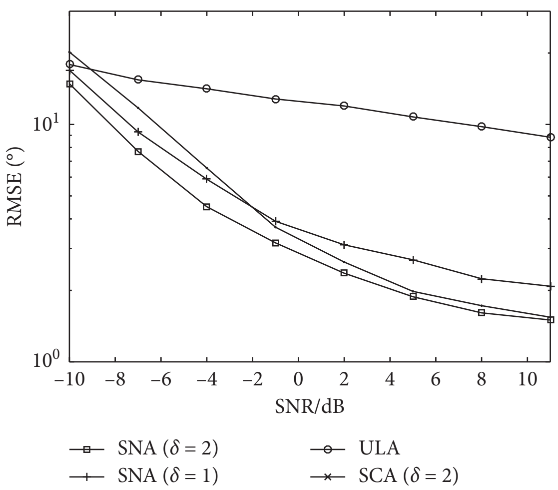

Figure 18: γ estimation performance with different array structures.

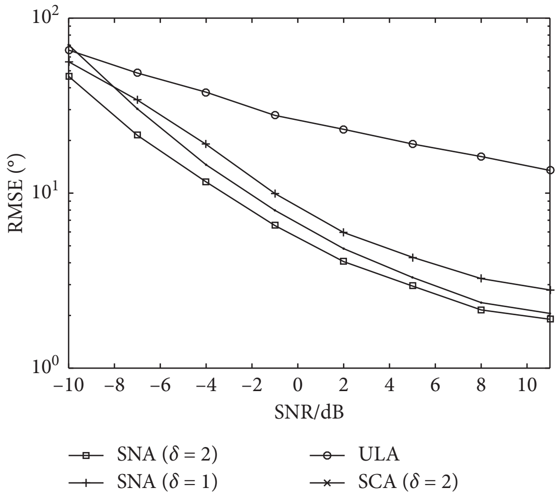

Figure 19: η estimation performance with different array structures.

the simulation of array structure performance. The proposed algorithm is tested where $J = 200$ and $\mathrm{SNR} = [-10, 11]dB$. The 4 array structures all have 6 sensors: SNA $\lfloor 3, 1, 3, 4, 1 \rfloor$, SNA $\lfloor 3, 1, 3, 4, 2 \rfloor$, ULA ($d = \lambda/2$), and SCA $\lfloor 4, 3, 3, 4, 2 \rfloor$.

As Figures 17–19 reveal, SNA $\lfloor 3, 1, 3, 4, 2 \rfloor$ acts best due to its large DOFs and array aperture. Although SCA $\lfloor 4, 3, 3, 4, 2 \rfloor$ is a sparse array, the missing elements in virtual array are the main cause of performance deterioration.

6. Conclusion

In this paper, a new array structure of sparse nested array is constructed, and a low-complexity off-grid orthogonal matching pursuit (OGOMP) algorithm is designed based on the proposed array structure to obtain DOA and polarization estimates. By introducing the sparse factor in EVSA, the proposed array structure has low mutual coupling, flexible array aperture, and high achievable degrees of freedom. Benefitting from the DOA initialization and polarization parameter elimination, the overcomplete dictionary is compact to tremendously reduce computational complexity. Meanwhile, the proposed OGOMP algorithm searches for the unambiguous high-precise DOA estimates and solves the problem of poor performance for off-grid signals in OMP algorithm. Finally, polarization estimates are measured by cross-correlation covariance matrix and estimated directional matrix based on least-square criterion.

Data Availability

The data used to support the findings of this study are available from the corresponding author upon reasonable request.

Conflicts of Interest

The authors declare that they have no conflicts of interest.

Acknowledgments

This work was supported by China NSF (Grants 61971217, 61971218, and 61631020), Jiangsu NSF (Grant BK20200444), the fund of Sonar Technology Key Laboratory (research on the theory and algorithm of signal processing for two-dimensional underwater acoustics coprime array), the fund of Sonar Technology Key Laboratory (range estimation and location technology of passive target via multiple array combination), and Jiangsu Key Research and Development Project (BE2020101).

References

[1] A. Abdi and H. H. Guo, "Signal correlation modeling in acoustic vector sensor arrays," *IEEE Transactions on Signal Processing*, vol. 57, no. 3, pp. 892–903, 2009.

[2] X. Zhang, W. Liu, Y. Xu, and Z. Liu, "Quaternion-valued robust adaptive beamformer for electromagnetic vector-sensor arrays with worst-case constraint," *Signal Processing*, vol. 104, pp. 274–283, 2014.

[3] B. Li and Y. X. Zou, "Improved DOA estimation with acoustic vector sensor arrays using spatial sparsity and subarray manifold," in *Proceedings of the IEEE International Conference on Acoustics. IEEE*, pp. 2557–3560, Kyoto, Japan, March 2012.

[4] G. Zheng, "Two-dimensional DOA estimation for polarization sensitive array consisted of spatially spread crossed-dipole," *IEEE Sensors Journal*, vol. 18, no. 12, pp. 5014–5023, 2018.

[5] K. T. Wong, Y. Song, C. J. Fulton, S. Khan, and W.-Y. Tam, "Electrically "long" dipoles in a collocated/orthogonal triad-for direction finding and polarization estimation," *IEEE Transactions on Antennas and Propagation*, vol. 65, no. 11, pp. 6057–6067, 2017.

[6] W. Si, P. Zhao, Z. Qu, and L. Wang, "Computationally efficient angle and polarization estimation in the presence of multipath propagation using dual-polarization vector sensor array," *International Journal of Antennas and Propagation*, vol. 2016, Article ID 7537160, 15 pages, 2016.

[7] J. Li and R. T. Compton, "Angle and polarization estimation using ESPRIT with a polarization sensitive array," *IEEE Transactions on Antennas and Propagation*, vol. 39, no. 9, pp. 1376–1383, 1991.

[8] J. Li and R. T. Compton, "Two-dimensional angle and polarization estimation using the ESPRIT algorithm," *IEEE Transactions on Antennas and Propagation*, vol. 40, no. 5, pp. 550–555, 1992.

[9] Q. W. Yuan, Q. Chen, and K. Sawaya, "MUSIC based DOA finding and polarization estimation using USV with polarization sensitive array antenna," in *Proceedings of IEEE Radio and Wireless Symposium*, pp. 339–342, San Diego, CF, USA, October 2006.

[10] L. Wang, L. Yang, G. Wang, Z. Chen, and M. Zou, "Uni-vector-sensor dimensionality reduction MUSIC algorithm for DOA and polarization estimation," *Mathematical Problems in Engineering*, vol. 2014, Article ID 682472, 9 pages, 2014.

[11] H. Chen, W. Wang, and W. Liu, "Joint DOA, range, and polarization estimation for rectilinear sources with a COLD array," *IEEE Wireless Communications Letters*, vol. 8, no. 5, pp. 1398–1401, 2019.

[12] K. T. Wong and M. D. Zoltowski, "High accuracy 2D angle estimation with extended aperture vector sensor arrays," in *Proceedings of the IEEE International Conference on Acoustics*, Atlanta, GA, USA, May 1996.

[13] K. T. Wong and M. D. Zoltowski, "Uni-vector-sensor ESPRIT for multisource azimuth, elevation, and polarization estimation," *IEEE Transactions on Antennas and Propagation*, vol. 45, no. 10, pp. 1467–1474, 1997.

[14] K. T. Wong and M. D. Zoltowski, "Closed-form direction finding and polarization estimation with arbitrarily spaced electromagnetic vector-sensors at unknown locations," *IEEE Transactions on Antennas and Propagation*, vol. 48, no. 5, pp. 671–681, 2000.

[15] M. D. Zoltowski and K. T. Wong, "Closed-form eigenstructure-based direction finding using arbitrary but identical subarrays on a sparse uniform cartesian array grid," *IEEE Transactions on Signal Processing*, vol. 48, no. 8, pp. 2205–2210, 2000.

[16] C. Hou, C. Fang, Z. Deng, Y. Wang, and W. Si, "Two-dimensional direction-of-arrival and polarization parameter estimation using parallel co-prime polarization sensitive array," *IEEE Access*, vol. 8, no. 8, pp. 6566–6574, 2020.

[17] Y. Yang, X. Mao, G. Jiang, and Y. Wang, "Spatially separated nested vector-sensor array with reduced mutual coupling," *IEEE Sensors Journal*, vol. 19, no. 14, pp. 5801–5817, 2019.

[18] W. Si, Y. Wang, and C. Zhang, "Three-parallel co-prime polarization sensitive array for 2-D DOA and polarization estimation via sparse representation," *IEEE Access*, vol. 7, pp. 15404–15413, 2019.

[19] N. Rashmi and M. Sarvagya, "Sparse channel estimation using orthogonal matching Pursuit algorithm for SCM-OFDM system," *International Conference on Advances in Computing*, pp. 1224–1227, 2016.

[20] G. A. Deschamps, "Techniques for handling elliptically polarized waves with special reference to antennas: part II-geometrical representation of the polarization of a plane electromagnetic wave," *Proceedings of the IRE*, vol. 39, no. 5, pp. 540–544, 1951.

[21] K. T. Wong, L. S. Linshan Li, and M. D. Zoltowski, "Root-MUSIC-based direction-finding and polarization estimation using diversely polarized possibly collocated antennas," *IEEE Antennas and Wireless Propagation Letters*, vol. 3, no. 1, pp. 129–132, 2004.

[22] W. Zheng, X. Zhang, Y. Wang, M. Zhou, and Q. Wu, "Extended coprime array configuration generating large-scale antenna co-array in massive MIMO system," *IEEE Transactions on Vehicular Technology*, vol. 68, no. 8, pp. 7841–7853, 2019.

[23] P. Pal and P. P. Vaidyanathan, "Nested Arrays: a novel approach to array processing with enhanced degrees of freedom," *IEEE Transactions on Signal Processing*, vol. 58, no. 8, pp. 4167–4181, 2010.

[24] C. Zhou, Y. Gu, X. Fan, Z. Shi, G. Mao, and Y. D. Zhang, "Direction-of-arrival estimation for coprime array via virtual array interpolation," *IEEE Transactions on Signal Processing*, vol. 66, no. 22, pp. 5956–5971, 2018.

[25] M. D. Zoltowski and K. T. Wong, "ESPRIT-based 2-D direction finding with a sparse uniform array of electromagnetic vector sensors," *IEEE Transactions on Signal Processing*, vol. 48, no. 8, pp. 2195–2204, 2000.

[26] L. Zhang, W. Liu, and J. L. Richard, "A minimum variance beamformer with linear and quadratic constraints based on uniform linear antenna arrays," in *Proceedings of the IEEE Antennas and Propagation Conference*, pp. 585–588, Charleston, Soouth Carolina, June 2009.

[27] J. Li, Y. Li, and X. Zhang, "Two-dimensional off-grid DOA estimation using unfolded parallel coprime array," *IEEE Communications Letters*, vol. 22, no. 12, pp. 2495–2498, 2018.

[28] N. Tayem and H. M. Kwon, "L-shape 2-dimensional arrival angle estimation with propagator method," *IEEE Transactions on Antennas and Propagation*, vol. 53, no. 5, pp. 1622–1630, 2005.

[29] P. Stoica and A. Nehorai, "Performance study of conditional and unconditional direction-of-arrival estimation," *IEEE Transactions on Acoustics, Speech, and Signal Processing*, vol. 38, no. 10, pp. 1783–1795, 1990.

Hindawi
Mathematical Problems in Engineering
Volume 2021, Article ID 6622154, 9 pages
https://doi.org/10.1155/2021/6622154

Research Article

DOA Estimation of a Novel Generalized Nested MIMO Radar with High Degrees of Freedom and Hole-Free Difference Coarray

Yule Zhang,[1,2] Guoping Hu,[2] Hao Zhou,[2] Mingming Zhu,[1,2] and Fei Zhang[1,3]

[1] *Graduate College, Air Force Engineering University, Xi'an 710051, China*
[2] *Air and Missile Defense College, Air Force Engineering University, Xi'an 710051, China*
[3] *Aeronautics Engineering College, Air Force Engineering University, Xi'an 710051, China*

Correspondence should be addressed to Yule Zhang; yule_zhang0921@163.com

Received 26 December 2020; Revised 8 January 2021; Accepted 12 January 2021; Published 27 January 2021

Academic Editor: Wang Zheng

A novel generalized nested multiple-input multiple-output (MIMO) radar for direction of arrival (DOA) estimation is proposed in this paper. The proposed structure utilizes the extended two-level nested array (ENA) as transmitter and receiver and adjusts the interelement spacing of the receiver with an expanding factor. By optimizing the array element configuration, we can obtain the best number of elements of the transmitter and receiver and the attainable degrees of freedom (DOF). Compared with the existing nested MIMO radar, the proposed MIMO array configuration not only has closed-form expressions for sensors' positions and the number of maximum DOF, but also significantly improves the array aperture. It is verified that the sum-difference coarray (SDCA) of the proposed nested MIMO radar can get higher DOF without holes. MUSIC algorithm based on Toeplitz matrix reconstruction is employed to prove the rationality and superiority of the proposed MIMO structure.

1. Introduction

Multiple-input multiple-output (MIMO) radar [1–3], with good space, frequency, and waveform diversity characteristics, is widely used in array signal processing [4–6] in the last few years. Compared with phased array radar, it has significant advantages in signal detection, parameter estimation [7], direction finding accuracy, spatial resolution [6], and antijamming capabilities, etc. However, the traditional MIMO radar usually adopts a uniform linear array (ULA) as transmitter and receiver, whose interelement spacing is equal to and no more than half wavelength. Hence, there are some problems in the direction of arrival (DOA) estimation for MIMO radar, such as mutual coupling of array elements [8] and limited aperture of virtual array elements [9].

In order to enhance the upper limit of degrees of freedom (DOF) and the flexibility of layout as well as reducing mutual coupling of physical sensors, sparse arrays such as the minimum redundancy array (MRA) [10, 11], coprime array (CPA) [12], and nested array (NA) [13–17] have been explored for DOA estimation and joint multiparameter estimation. In addition, sparse arrays combined with MIMO radar can further increase DOF through the sum-difference coarray (SDCA) [18], so as to improve the accuracy of direction finding and angle resolution ability.

For the purpose of improving sensor utilization, the minimum redundancy MIMO radar [19] designs the optimal array spacing by optimizing the number of virtual array elements, whereas it requires complex computational search and lacks closed-form expressions of DOF. The coprime MIMO radar generally uses part [20] or whole CPA [21] as the transmitting array and the receiving array. Li et al. [20] combined it with the real-value ESPRIT algorithm to DOA estimation, but did not consider the virtual array expansion of the echo signal model. Therefore, its DOF is limited by the number of physical sensors. Shi et al. [22] defined the generalized sum-difference coarray (GSDC) and simultaneously derived the closed-form expressions of the total number of virtual array elements of the generalized two-level coprime MIMO radar, which can obtain $O(M^2N^2)$ DOF by $O(M+N)$ physical sensors. The obtained DOF are much higher than that in [20, 21] with $O(MN)$ DOF. Unfortunately, there are holes in the SDCA of the abovementioned coprime MIMO radars, so multiple signal classification (MUSIC) [23] and estimation of signal parameters via rotational invariance technique (ESPRIT) algorithms [24] cannot be firsthand applied to these array structures.

Nested MIMO radar [25, 26] has closed-form expressions of positions and the number of virtual array elements and overcomes the defects of the minimum redundancy MIMO radar and coprime MIMO radar. Qin et al. [25] exploited nested subarrays as transmitting and receiving arrays to DOA estimation of mixed coherent and uncorrelated targets. Zheng et al. [26] adopted traditional two-level nested MIMO array to joint direction of departure (DOD) and direction of arrival (DOA) estimation with closed-form DOF. They can provide $O(M^2)$ DOF with $O(M)$ sensors. Yang et al. [27, 28] designed a hole-free generalized nested MIMO configuration on the concept of the conventional two-level nested array, which improves DOF and angle estimation performance while effectively reducing the mutual coupling between the transmitting sensors. Specifically, it can provide $O(M^4)$ DOF with $O(M)$ elements.

To further enhance DOF, this paper adopts the extended two-level nested array (ENA) [15] to construct a new generalized nested MIMO radar. Firstly, the whole ENA is used as the transmitting array and receiving array of MIMO radar. Next, an expanding factor is employed to increase the receiving array spacing, and closed-form expressions of DOF and the best physical array element configuration are derived. Afterwards, Toeplitz matrix reconstruction [29] based on the MUSIC algorithm is employed to exploit the superiority of the proposed array configuration.

To be more specific, the main contributions of this paper are as follows:

(a) The optimal array element configuration structure of ENA is deduced and higher degrees of freedom are obtained. Besides, the difference coarray (DCA) is a ULA without holes.

(b) A new generalized nested MIMO radar based on ENA is constructed, and the optimal sensors' positions and the maximum DOF are derived, which can obtain $O(G^4)$ DOF with $O(G)$ sensors. Meanwhile, the SDCA is a ULA without holes. Its DOF is much higher than the existing nested MIMO radars in [25–28].

2. Echo Signal Model

A monostatic sparse array MIMO radar consists of a transmitter with $M = M_1 + M_2$ arrays and a receiver with $N = N_1 + N_2$ arrays. The positions of the transmitting array are located at $\mathbf{P}_t = \{p_{tm} | m = 1, 2, \ldots, M\}$ and the positions of the receiving array are located at $\mathbf{P}_r = \{p_{rn} | n = 1, 2, \ldots, N\}$, respectively. The unit array element spacing d of the sensor is equal to $\lambda/2$, where λ stands for the signal wavelength. Suppose that there are K far-field uncorrelated narrowband sources from angles $\theta = \{\theta_k | k = 1, 2, \ldots, K\}$, and the reflection coefficient of the k-th source is β_k. Then, the echo signal model can be expressed as follows:

$$\mathbf{x}(t) = \sum_{k=1}^{K} \boldsymbol{\alpha}_r(\theta_k)\beta_k \boldsymbol{\alpha}_t^T(\theta_k)\mathbf{b}(t) + \mathbf{w}(t), \tag{1}$$

where $\mathbf{b}(t) = [b_0(t), b_1(t), \ldots, b_{M-1}(t)]^T$ denotes the transmit signal; $\mathbf{w}(t)$ is an additive white Gaussian noise; and $\alpha_t(\theta_k)$ and $\alpha_r(\theta_k)$ are the transmit steering vectors and receive steering vectors of the k-th source, respectively, which can be expressed as

$$\begin{aligned} \boldsymbol{\alpha}_t(\theta_k) &= \left[1, e^{\left(-j2\pi p_{t2}\sin\theta_k/\lambda\right)}, \ldots, e^{\left(-j2\pi p_{tM}\sin\theta_k/\lambda\right)}\right]^T, \\ \boldsymbol{\alpha}_r(\theta_k) &= \left[1, e^{\left(-j2\pi p_{r2}\sin\theta_k/\lambda\right)}, \ldots, e^{\left(-j2\pi p_{rN}\sin\theta_k/\lambda\right)}\right]^T, \end{aligned} \tag{2}$$

where $p_{tm} \in \mathbf{P}_t$ and $p_{rn} \in \mathbf{P}_r$ represent the sensor positions in the transmitter and receiver, respectively, and $p_{t1} = p_{r1} = 0$.

Since the transmitting waveforms of MIMO radar are orthogonal to each other, i.e., $\mathbf{R}_b = E[\mathbf{b}(t)\mathbf{b}(t)^H] = \mathbf{I}_{M\times N}$, the output of the generalized matched filters for the echo signal can be expressed as follows:

$$\begin{aligned} x(t) &= \sum_{k=1}^{K} \beta_k (\boldsymbol{\alpha}_t(\theta_k) \otimes \boldsymbol{\alpha}_r(\theta_k)) + \mathbf{n}(t) \\ &= [\boldsymbol{\alpha}_t(\theta_1) \otimes \boldsymbol{\alpha}_r(\theta_1), \ldots, \boldsymbol{\alpha}_t(\theta_K) \otimes \boldsymbol{\alpha}_r(\theta_K)]\mathbf{s}(t) + \mathbf{n}(t) \\ &= (\mathbf{A}_t \odot \mathbf{A}_r)\mathbf{s}(t) + \mathbf{n}(t). \end{aligned} \tag{3}$$

where$\mathbf{A}_t = [\mathbf{a}_t(\theta_1), \mathbf{a}_t(\theta_2), \ldots, \mathbf{a}_t(\theta_K)]$; $\mathbf{A}_r = [\mathbf{a}_r(\theta_1), \mathbf{a}_r(\theta_2), \ldots, \mathbf{a}_r(\theta_K)]$; $\mathbf{n}(t)$ is an additive white Gaussian noise vector; $\mathbf{s}(t) = [\beta_1, \beta_2, \ldots, \beta_K]^T$; $\otimes$ and $\odot$ denote Kronecker product and Khatri–Rao product, respectively.

The covariance matrix of the echo signal can be obtained by

$$\begin{aligned} \mathbf{R} &= E\left[\mathbf{x}(t)\mathbf{x}(t)^H\right] = (\mathbf{A}_t \odot \mathbf{A}_r)\mathbf{R}_s(\mathbf{A}_t \odot \mathbf{A}_r)^H + \sigma_n^2 \mathbf{I}_{M_t N_r} \\ &= \mathbf{A}\mathbf{R}_s\mathbf{A}^H + \sigma_n^2 \mathbf{I}_{M_t N_r}, \end{aligned} \tag{4}$$

where $\mathbf{R}_s = E[s(t)s(t)^H] = \mathrm{diag}[\sigma_1^2, \sigma_2^2, \ldots, \sigma_k^2]$ is the target covariance matrix, σ_k^2 denotes the signal energy of the k-th target, $\mathbf{A}= \mathbf{A}_t \odot \mathbf{A}_r$, and σ_n^2 is the noise variance.

The observing vector can be obtained by vectorizing $\mathbf{R}$:

$$\begin{aligned} r &= \mathrm{vec}(\mathbf{R}) = (\mathbf{A}^* \odot \mathbf{A})p + \sigma_n^2 \mathrm{vec}\left(\mathbf{I}_{M_t N_r}\right) \\ &= (\mathbf{A}^* \odot \mathbf{A})p + \sigma_n^2 \mathrm{vec}\left(\mathbf{I}_{M_t N_r}\right) = \mathbf{B}p + \sigma_n^2 \mathrm{vec}\left(\mathbf{I}_{M_t N_r}\right), \end{aligned} \tag{5}$$

where $\mathrm{vec}(\cdot)$ represents vectorized operation; $\mathbf{p} = [\sigma_1^2, \sigma_2^2, \ldots, \sigma_k^2]^T$; $(\cdot)$ implies the complex conjugation of the matrix.

$$\mathbf{B}=\mathbf{A}^*\odot\mathbf{A}=\left[\mathbf{a}_t^*(\theta_1)\otimes\mathbf{a}_r^*(\theta_1)\otimes\mathbf{a}_t(\theta_1)\otimes\mathbf{a}_r(\theta_1),\ldots,\mathbf{a}_t^*(\theta_k)\right.$$
$$\left.\otimes\mathbf{a}_r^*(\theta_k)\otimes\mathbf{a}_t(\theta_k)\otimes\mathbf{a}_r(\theta_k)\right]. \tag{6}$$

3. Extended Two-level Nested Array

In this section, the configuration of the extended two-level nested array (ENA) is formulated first. Then the optimal configuration structure of the physical array elements and the closed-form expressions of its DOF are derived.

3.1. ENA Configuration. As shown in Figure 1, the ENA configuration maintains the basic structure of the nested array, except for increasing the first two sensors of the sparse ULA by d intervals. And the total number of sensors is equal to $M = M_1 + M_2$.

Therefore, the extended two-level nested array sensor location can be expressed as

$$\mathbf{P}_{\mathrm{ENA}}=\{0,1,\ldots,M_1-1,M,2(M_1+1),3(M_1+1),\ldots,M_2(M_1+1)\}. \tag{7}$$

Then, the difference coarray of ENA can be defined as

$$\mathbf{S}_{\mathrm{ENA}}=\{s-\tilde{s},s,\tilde{s}\in\mathbf{P}_{\mathrm{ENA}}\}=\{-M_2(M_1+1),\ldots,0,\ldots,M_2(M_1+1)\}. \tag{8}$$

3.2. Attainable DOF of ENA. According to equation (8), the DOF of ENA is

$$\mathrm{DOF}=2M_2(M_1+1)+1. \tag{9}$$

When the total number of sensors is fixed to $M = M_1 + M_2$, the array element optimal configuration structure can be optimized to have attainable DOF, as shown in Table 1.

4. Proposed Generalized Nested MIMO Radar

In this section, the entire ENA is adopted as the transmitter and receiver to construct an extended nested MIMO radar (ENA-TR). Furthermore, a generalized extended two-level nested MIMO radar (GENA-TR) based on ENA-TR is proposed and the closed-form expressions for attainable DOF are deduced.

4.1. ENA-TR. From equation (7), the position of the transmitter with M sensors and receiver with N sensors is given by

$$\mathbf{P}_T=\{0,1,\ldots,M_1-1,M_1,2(M_1+1),3(M_1+1),\ldots,M_2(M_1+1)\}, \tag{10}$$

$$\mathbf{P}_R=\{0,1,\ldots,N_1-1,N_1,2(N_1+1),3(N_1+1),\ldots,N_2(N_1+1)\}. \tag{11}$$

According to equation (8), the difference coarray of the transmitter and receiver are both consecutive ULAs with $2M_2(M_1+1)+1$ and $2N_2(N_1+1)+1$ virtual array elements, which are located at

$$\mathbf{S}_T=\left\{s_t-s_{\tilde{t}},s_t,s_{\tilde{t}}\in\mathbf{P}_T\right\}=\{-M_2(M_1+1),\ldots,0,\ldots M_2(M_1+1)\}, \tag{12}$$

$$\mathbf{S}_R=\{s_r-s_{\tilde{r}},s_r,s_{\tilde{r}}\in\mathbf{P}_R\}=\{-N_2(N_1+1),\ldots,0,\ldots N_2(N_1+1)\}. \tag{13}$$

It can be known from equation (6) that the virtual element positions of $\mathbf{B}=\mathbf{A}^*\odot\mathbf{A}$ are composed of sum-difference coarray of physical sensor positions.

$$\begin{aligned}\mathbf{S}_{\mathrm{SDCA}}^{\mathrm{ENA-TR}}&=\left\{(s_t+s_r)-\left(s_{\tilde{t}}+s_{\tilde{r}}\right)|s_t,s_{\tilde{t}}\in\mathbf{P}_T,s_r,s_{\tilde{r}}\in\mathbf{P}_R\right\}\\&=\left\{\left(s_t+s_{\tilde{t}}\right)-\left(s_r+s_{\tilde{r}}\right)|s_t,s_{\tilde{t}}\in\mathbf{P}_T,s_r,s_{\tilde{r}}\in\mathbf{P}_R\right\}\\&=\{l_t+l_r|l_t\in\mathbf{S}_T,l_r\in\mathbf{S}_R\}.\end{aligned} \tag{14}$$

Therefore, the sum-difference coarray of ENA-TR is essentially the sum coarray of two difference coarrays.

4.2. GENA-TR. The ENA-TR configuration fails to make full use of the virtual aperture expansion effect of the sum-difference coarray. By introducing the interelement spacing expansion factor, a generalized ENA-TR (GENA-TR) is established to increase DOF, as shown in Figure 2.

The interelement spacing of the receiver is enlarged with an expansion factor α, so the receiver sensor positions are located at

$$\mathbf{P}_R^\alpha=\alpha\mathbf{P}_R=\alpha\{0,1,\ldots,N_1-1,N_1,2(N_1+1),3(N_1+1),\ldots,N_2(N_1+1)\}. \tag{15}$$

It can be seen from set (15) that the difference coarray of the receiver is a filled ULA with interelement spacing enlarged by factor α. And the difference coarray set is given by

$$\mathbf{S}_R^\alpha=\left\{s_r^\alpha-s_{\tilde{r}}^\alpha,s_r^\alpha,s_{\tilde{r}}^\alpha\in\mathbf{P}_r^\alpha\right\}=\alpha\{-N_2(N_1+1),\ldots,0,\ldots,N_2(N_1+1)\}. \tag{16}$$

According to equations (10) and (15), we can get the sum-difference coarray set of GENA-TR:

$$\begin{aligned}\mathbf{S}_{\mathrm{SDCA}}^{\mathrm{GENA-TR}}&=\left\{(s_t+s_r^\alpha)-\left(s_{\tilde{t}}+s_{\tilde{r}}^\alpha\right),s_t,s_{\tilde{t}}\in\mathbf{P}_T,s_r^\alpha,s_{\tilde{r}}^\alpha\in\mathbf{P}_R^\alpha\right\}\\&=\left\{\left(s_t+s_{\tilde{t}}\right)-\left(s_r^\alpha+s_{\tilde{r}}^\alpha\right),s_t,s_{\tilde{t}}\in\mathbf{P}_T,s_r^\alpha,s_{\tilde{r}}^\alpha\in\mathbf{P}_R^\alpha\right\}\\&=\{l_t+l_r^\alpha,l_t\in\mathbf{S}_T,l_r^\alpha,\in\mathbf{S}_R^\alpha\}.\end{aligned} \tag{17}$$

Proposition 1. *The sum-difference coarray of GENA-TR has the following properties:*

(a) *The range of the expansion factor α is* $1\leq\alpha\leq 2M_2(M_1+1)+1$

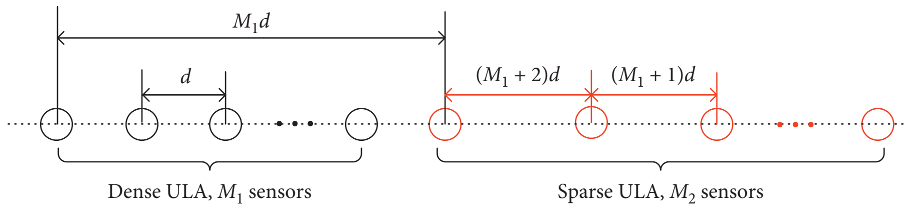

FIGURE 1: ENA configuration.

TABLE 1: Optimal configuration structure for ENA.

M	Optimal M_1, M_2	DOF
Odd	$M_1 = (M-1)/2, M_2 = (M+1)/2$	$(M^2+3)/2+M$
Even	$M_1 = M_2 = M/2$	$(M^2+2)/2+M$

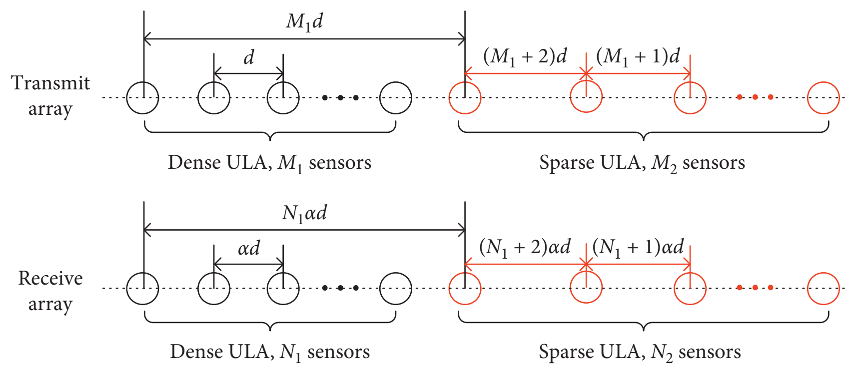

FIGURE 2: GENA-TR structure.

(b) $\mathbf{S}_{SDCA}^{GENA-TR}$ contains all the consecutive integers in the range $[-V, V]$, where $V = M_2(M_1+1) + \alpha N_2(N_1+1)$

(c) The sum-difference coarray of GENA-TR contains $2[M_2(M_1+1) + 2\alpha N_2(N_1+1)] + 1$ unique lags of virtual array elements without holes

Proof.

(a) It can be known from equations (12) and (16) that $\mathbf{S}_T$ and $\mathbf{S}_R^\alpha$ are symmetrical sets, so $l_t + l_r^\alpha = l_t - l_r^\alpha$. Therefore, the sum-difference coarray of GENA-TR is essentially a difference coarray of two subarrays. When $1 \le \alpha \le 2M_2(M_1+1)+1$, $\mathbf{S}_{\mathrm{SDCA}}^{\mathrm{GENA-TR}}$ can get consecutive virtual array elements with certain positions [13].

(b) According to equations (12) and (16), the margins of $\mathbf{S}_{\mathrm{SDCA}}^{\mathrm{GENA-TR}}$ can be obtained.

For the left margin,

$$-V = -M_2(M_1+1) + [-\alpha N_2(N_1+1)]. \tag{18}$$

For the right margin,

$$V = M_2(M_1+1) + [\alpha N_2(N_1+1)]. \tag{19}$$

In addition, $\mathbf{S}_T$ and $\mathbf{S}_R^\alpha$ are both consecutive integers, so $\mathbf{S}_{\mathrm{SDCA}}^{\mathrm{GENA-TR}}$ is a hole-free ULA.

(c) According to proposition (b), the maximum number of $\mathbf{S}_{\mathrm{SDCA}}^{\mathrm{GENA-TR}}$ is $2V+1 = 2[M_2(M_1+1) + 2\alpha N_2(N_1+1)+1]$.

The sum-difference coarray of GENA-TR can attain the maximum number of DOF, where $\alpha = 2M_2(M_1+1)+1$. When the total number of physical array elements is determined to be G, the array construction problem turns to an optimization problem about the maximum number of DOF

$$\begin{aligned} &\max [2M_2(M_1+1)+1][2N_2(N_1+1)+1] \\ &\text{s.t.} \quad G = M_1 + M_2 + N_1 + N_2. \end{aligned} \tag{20}$$

The Lagrange function of equation (20) can be expressed as

$$\begin{aligned} f &= [2M_2(M_1+1)+1][2N_2(N_1+1)] \\ &\quad + \eta(M_1+M_2+N_1+N_2-G). \end{aligned} \tag{21}$$

where η represents the Lagrange multiplier.

Taking the partial of f with respect to M_1, M_2, N_1, N_2, η, the following system of equations can be expressed:

Table 2: Optimal configuration structure for GENA-TR.

G	Optimal M_1, M_2, N_1, N_2	DOF
$G = 4k$	$M_1 = M_2 = N_1 = N_2 = G/4$	$(G^4 + 8G^3 + 32G^2 + 64G + 64)/64$
$G = 4k + 1$	$M_1 = N_1 = N_2 = (G-1)/4$, $M_2 = (G+3)/4$ or $M_1 = M_2 = N_1 = (G-1)/4, N_2 = (G+3)/4$	$(G^4 + 8G^3 + 34G^2 + 64G + 85)/64$
$G = 4k + 2$	$M_1 = N_1 = (G-2)/4$, $M_2 = N_2 = (G+2)/4$	$(G^4 + 8G^3 + 40G^2 + 96G + 114)/64$
$G = 4k + 3$	$M_1 = M_2 = N_2 = (G+1)/4$, $N_2 = (G-3)/4$ or $M_1 = (G-3)/4$, $M_2 = N_1 = N_2 = (G+1)/4$	$(G^4 + 8G^3 + 34G^2 + 80G + 117)/64$

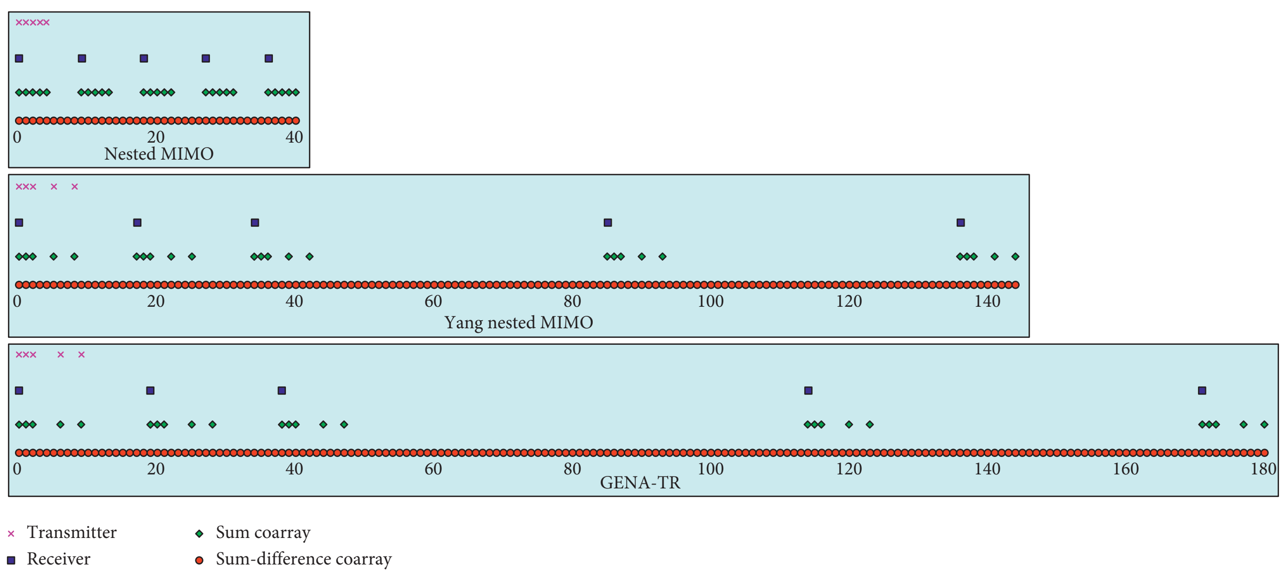

Figure 3: An example of different MIMO radars with fiver transmitter and fiver receiver.

$$\left\{\begin{array}{c} 2M_2\left[2N_2\left(N_1+1\right)+1\right]+\beta=0, \\ 2\left(M_1+1\right)\left[2N_2\left(N_1+1\right)+1\right]+\beta=0, \\ 2N_2\left[2M_2\left(M_1+1\right)+1\right]+\beta=0, \\ 2\left(N_1+1\right)\left[2M_2\left(M_1+1\right)+1\right]+\beta=0, \\ M_1+M_2+N_1+N_2\_G=0 \end{array}\right\}. \tag{22}$$

By solving equation (22), the optimization results can be obtained, including the total number of physical sensors, the specific situation of the optimal array element configuration, and maximum DOF with the sum-difference coarray of generalized extended two-level nested MIMO radar, as shown in Table 2.

To illustrate the distribution characteristics of the virtual array elements given by the proposition clearly, an example is shown in Figure 3, where $M_1 = N_1 = 2, M_2 = N_2 = 3$, $\alpha = 2M_2(M_1 + 1) + 1 = 19$, and only the positive part is demonstrated due to the symmetry of SDCA. Moreover, nested MIMO [25] and Yang nested MIMO [27] are also given for comparison. It can be found that the consecutive lags of GENA-TR are $[0, 180]$ in this example, which is higher than nested MIMO and Yang nested MIMO, and SDCA does not have holes.

Table 3 shows the consecutive lags and DOF of different MIMO geometries with a given total number of physical elements. It can be clearly seen that the GENA-TR not only retains the original advantages of the existing sparse array MIMO radar, whose sum-difference coarray is a hole-free ULA, but also significantly enhances DOF. Next, the redundant virtual array elements formed by sum-difference coarray can be averaged [30] and combined with the MUSIC algorithm based on Toeplitz matrix reconstruction for DOA estimation. □

5. Simulation Results

In this section, several numerical simulations are presented to verify the rationality and superiority of the proposed nested MIMO radar (GENA-TR) and compare with other sparse array MIMO radars, including nested MIMO [25], NA-TR [26], Yang nested MIMO [27], Zheng nested MIMO [28], and ENA-TR. The total number of physical sensors is set as $G = 10$.

Table 3: Consecutive lags and DOF of different MIMO radars.

	Nested MIMO		Yang nested MIMO		GENA-TR	
Number of sensors	Consecutive lags	DOF	Consecutive lags	DOF	Consecutive lags	DOF
10	[−40, 40]	81	[−144, 144]	289	[−180, 180]	361
13	[−71, 71]	143	[−356, 356]	713	[−412, 412]	825
17	[−127, 127]	255	[−955, 955]	1911	[−1045, 1045]	2091
22	[−220, 220]	441	[−2520, 2520]	5041	[−2664, 2664]	5329

5.1. DOF Comparison. In this numerical simulation, we compare the maximum DOF of GENA-TR with other nested MIMO geometries, where we change the total number of physical sensors from 10 to 20. It can be seen from Figure 4 that the maximum DOF of various nested MIMO radars increase with the number of physical array elements, and the proposed nested MIMO radar has the most obvious growth trend. In addition, it should be noted that when the number of physical elements is the same, the DOF of ENA-TR is only 4 higher than that of NA-TR, whereas GENA-TR can obtain a higher DOF than other MIMO radars.

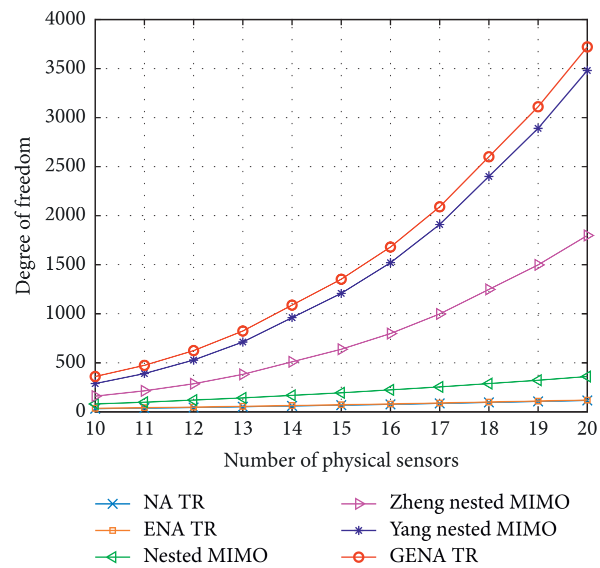

Figure 4: The maximum DOF of different nested MIMO versus the number of physical sensors.

5.2. Spatial Spectrum. In this numerical simulation, the Toeplitz matrix reconstruction based on the MUSIC algorithm is adopted to validate the spatial spectrum performance of GENA-TR and Yang nested MIMO radar [27], as shown in Figures 5 and 6. Suppose that there are $K = 101$ far-field uncorrelated narrowband targets uniformly distributed from -60° to 60° at an angular interval of 1.2°, where the signal-to-noise ratio (SNR) is equal to 10 dB, the number of snapshots $L = 1000$ and the search angel range is $[-90^\circ: 0.01^\circ: 90^\circ]$. It is obvious that GENA-TR can obtain better peaks and accurately estimate the DOA of all targets, whereas Yang nested MIMO radar has false peaks. Moreover, it is worth noting that the reason why NA-TR, ENA-TR, nested MIMO, and Zheng nested MIMO cannot estimate 101 targets is that MUSIC algorithm based on Toeplitz matrix reconstruction causes their DOF to be reduced by half, becoming 17, 19, 41, and 81, respectively.

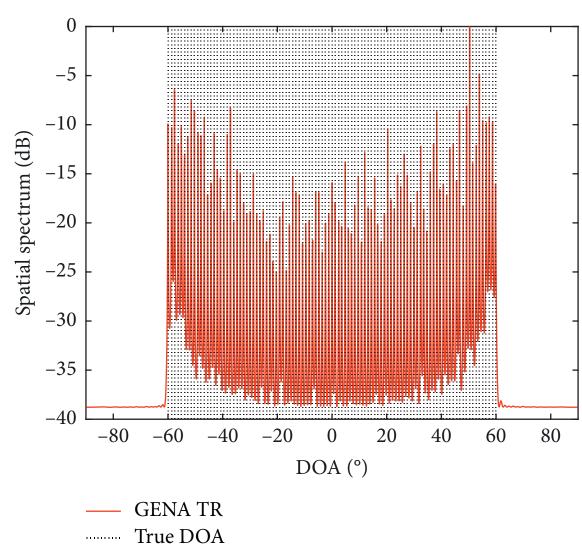

Figure 5: Spatial spectrum of GENA-TR.

5.3. Root Mean Square Error. In this numerical simulation, the root mean square error (RMSE) of DOA estimation for GENA-TR and other nested MIMO radars is compared via Monte Carlo experiments. It is assumed that there are $K = 13$ far-field uncorrelated narrowband targets evenly distributed in $[-60^\circ: 10^\circ: 60^\circ]$. Figure 7 depicts the RMSE of different nested MIMO radars versus SNR, where the number of snapshots is $L = 500$. Figure 8 shows the RMSE of different nested MIMO radars versus the number of snapshots, where SNR = 0 dB. The RMSE of DOA estimation can be calculated as

$$\mathrm{RMSE} = \sqrt{\frac{1}{\mathrm{TK}} \sum_{i=1}^{T} \sum_{k=1}^{k} \left(\widehat{\theta}_k^i - \theta_k \right)^2}, \tag{23}$$

where $T = 200$ represents the number of total Monte Carlo simulations, θ_k denotes the true DOA, and $\widehat{\theta}_k^i$ implies the estimated DOA of the i-th trials.

It can be clearly seen from Figures 7 and 8 that as SNR and the number of snapshots increase, the DOA estimation accuracy of each MIMO radar has been improved, and simultaneously the DOA estimation performance of GENA-

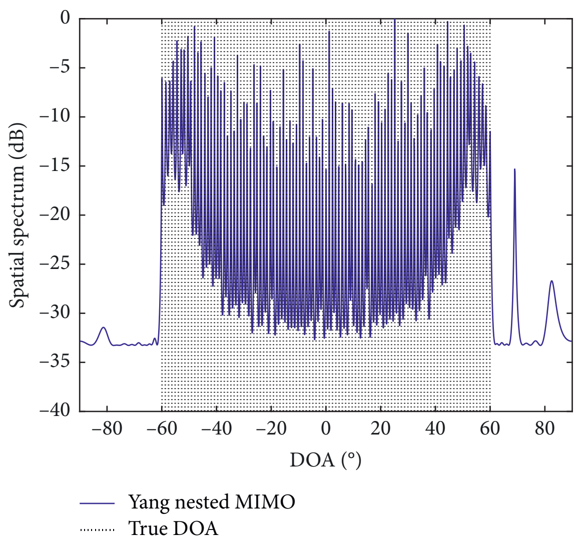

Figure 6: Spatial spectrum of Yang nested MIMO.

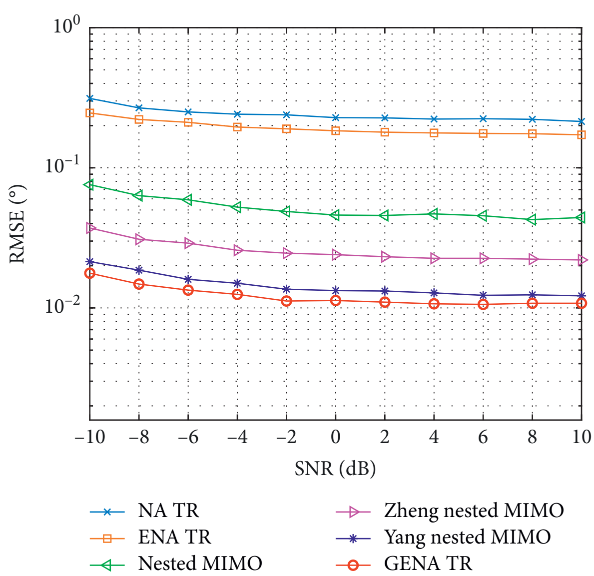

Figure 7: RMSE of different nested MIMO versus SNR.

TR is better than that of other MIMO radars. This is because the proposed GENA-TR can obtain a lager virtual element aperture when the number of physical sensors is the same.

5.4. Probability of Detection. In this numerical simulation, the probability of detection (PD) performance of DOA estimation with GENA-TR and other nested MIMO radars are compared via 200 Monte Carlo experiments. It is assumed that there are $K = 13$ far-field uncorrelated narrowband targets evenly distributed in $[-60^{\circ}: 10^{\circ}: 60^{\circ}]$. Figure 9 shows the PD of different nested MIMO radars versus SNR, where the number of snapshots is $L = 200$. Figure 10 shows the PD of different nested MIMO radars versus the number of snapshots, where SNR = −10 dB. Here, PD is defined as the ratio of the number of numerical

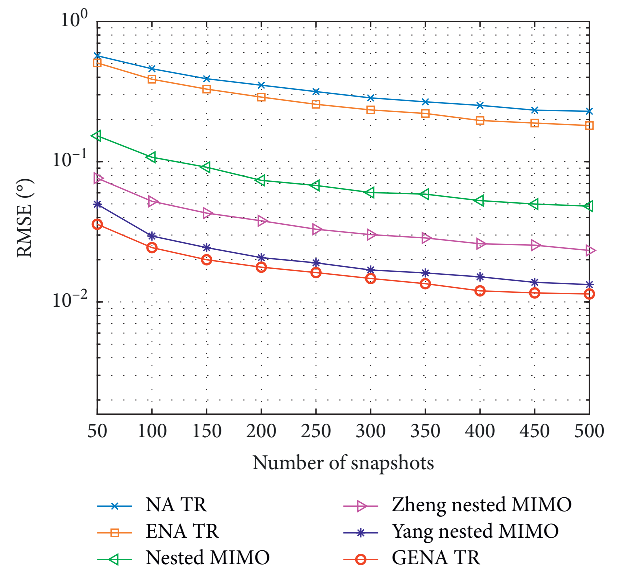

Figure 8: RMSE of different nested MIMO versus the number of snapshots.

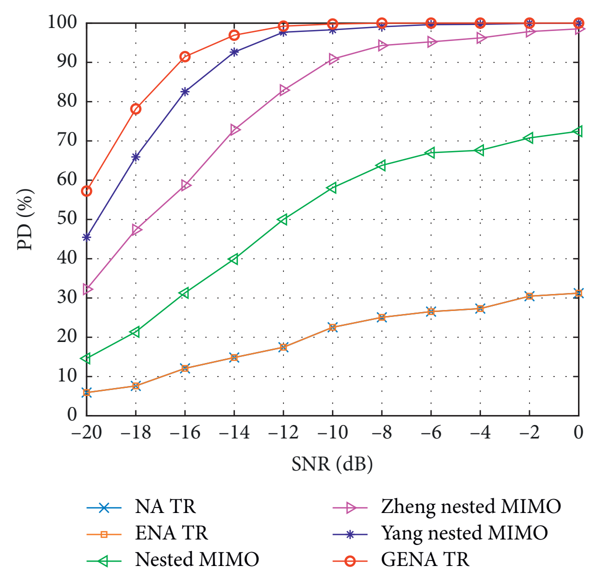

Figure 9: PD of different nested MIMO versus SNR.

simulations with the DOA estimation error within $\pm 0.01^{\circ}$ in the total experiments.

As shown in Figures 9 and 10, the PD of each nested MIMO radar has been improved as SNR and the number of snapshots increase. In addition, under the same SNR or the same number of snapshots, GENA-TR has a higher PD. Especially under the conditions of low SNR and low snapshots, the PD of the proposed nested MIMO radar is significantly better than that of other nested MIMO radars.

5.5. Resolution Performance. In this numerical simulation, the resolution performance of DOA estimation with GENA-TR and other nested MIMO radars is compared. Here,

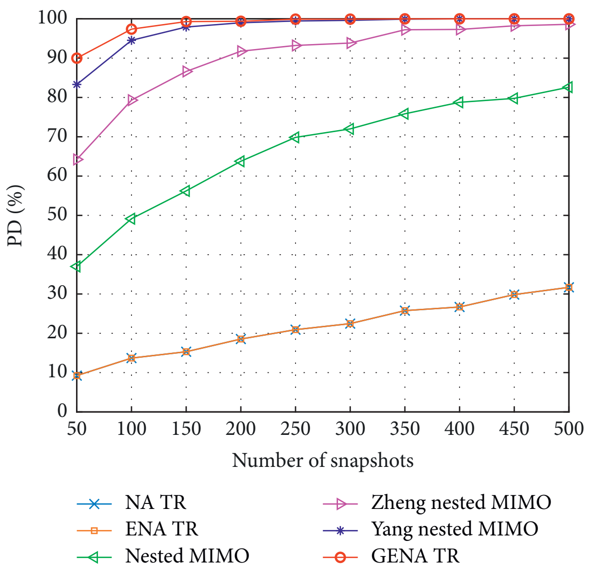

FIGURE 10: PD of different nested MIMO versus the number of snapshots.

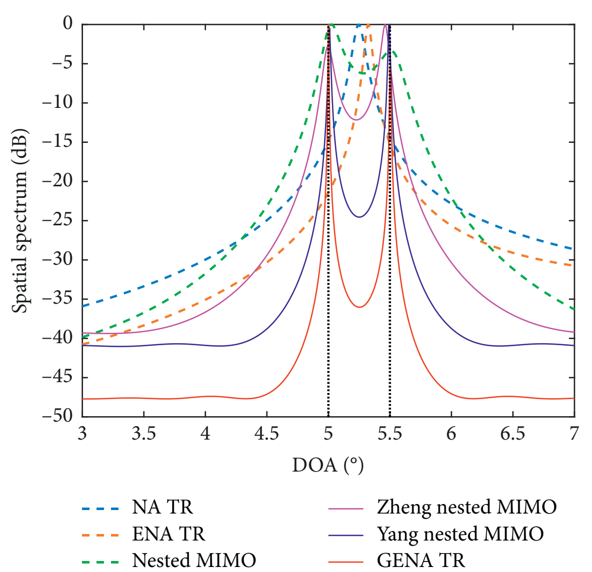

FIGURE 11: Spatial spectrum with two uncorrelated closely located targets.

resolution is defined as both the deviation between the true DOA and the estimated DOA of two closely targets which are less than one-half of the difference between the true angles of them [28]. Assume that there are $K = 2$ far-field uncorrelated narrowband targets located at $[5^{\circ}, 5.5^{\circ}]$. Figure 11 demonstrates the spatial spectrum of the different nested MIMO radars, where $\mathrm{SNR} = -10\,\mathrm{dB}$ and the number of snapshots $L = 200$.

It can be clearly seen from Figure 11 that NA-TR and ENA-TR cannot distinguish the above two targets, while other nested MIMO radars can distinguish the above two targets. Furthermore, GENA-TR has higher resolution and sharper peaks due to its higher degrees of freedom.

6. Conclusions

In this paper, a generalized extended two-level nested MIMO radar array configuration using extended two-level nested array is proposed, which can significantly improve the virtual array apertures and degrees of freedom, and the sum-difference coarray is a ULA without holes. In addition, the closed-form expressions of the maximum DOF are derived for a given number of physical sensors. At last, some numerical simulations are conducted to illustrate the advantages of the proposed GENA-TR in DOF, the estimation accuracy and the angle resolution.

Data Availability

The data supporting the conclusion of the article are shown in the research paper.

Conflicts of Interest

The authors declare that there are no conflicts of interest regarding the publication of this paper.

Acknowledgments

The authors would appreciate Chenghong Zhan and Zixin Zhang of Air and Missile Defense College, Air Force Engineering University, for their theoretical guidance and text correction. This work was supported by the Foundation of National Natural Science Foundation of China under Grant 61871395.

References

[1] E. Fishier, A. Haimovich, R. S. Blum et al., "MIMO radar: an idea whose time has come," in *Proceedings of the IEEE Radar Conference*, pp. 71–78, Philadelphia, PA, USA, April 2004.

[2] E. Jornson, L. Sanguinetti, H. Wymeersch et al., "Massive MIMO is a reality-what is next," *Digital Signal Processing*, vol. 94, pp. 3–20, 2019.

[3] P. Bezousek, P. Ezouske, and S. Karamazov, "MIMO radar signals with better correlation characteristics," *Journal of Electrical Engineering*, vol. 71, no. 3, pp. 210–216, 2020.

[4] T. Chen, J. Yang, and M. Guo, "A MIMO radar-based DOA estimation structure using compressive measurements," *Sensors*, vol. 19, no. 21, pp. 4706–4719, 2019.

[5] B. Liu, E. E. Kuruoglu, J. Zhang, F. Gini, T. Xue, and W. Lei, "Angle estimation in MIMO radar using a new sparse representation approach," *International Journal of Electronics*, vol. 106, no. 11, pp. 1694–1709, 2019.

[6] J. Du, M. Han, L. Jin, Y. Hua, and S. Li, "Target localization methods based on iterative super-resolution for bistatic MIMO radar," *Electronics*, vol. 9, no. 2, pp. 341–359, 2020.

[7] W. Zhang, W. Liu, J. Wang, and S. Wu, "Joint transmission and reception diversity smoothing for direction finding of coherent targets in MIMO radar," *IEEE Journal of Selected Topics in Signal Processing*, vol. 8, no. 1, pp. 115–124, 2014.

[8] E. Boudaher, F. Ahmad, M. G. Amin, and A. Hoorfar, "Mutual coupling effect and compensation in non-uniform arrays for direction-of-arrival estimation," *Digital Signal Processing*, vol. 61, pp. 3–14, 2017.

[9] J. Konishi, H. Yamada, and Y. Yamaguchi, "Optimum element arrangements in MIMO radar using Khatri-Rao product virtual array processing," *IEICE Communications Express*, vol. 7, no. 11, pp. 407–414, 2018.
[10] A. Moffet, "Minimum-redundancy linear arrays," *IEEE Transactions on Antennas and Propagation*, vol. 16, no. 2, pp. 172–175, 1968.
[11] C. S. Ruf, "Numerical annealing of low-redundancy linear arrays," *IEEE Transactions on Antennas and Propagation*, vol. 41, no. 1, pp. 85–90, 1993.
[12] P. P. Vaidyanathan and P. Pal, "Sparse sensing with co-prime samplers and arrays," *IEEE Transactions on Signal Processing*, vol. 59, no. 2, pp. 573–586, 2011.
[13] P. Pal and P. P. Vaidyanathan, "Nested arrays: a novel approach to array processing with enhanced degrees of freedom," *IEEE Transactions on Signal Processing*, vol. 58, no. 8, pp. 4167–4181, 2010.
[14] M. Yang, L. Sun, X. Yuan, and B. Chen, "Improved nested array with hole-free DCA and more degrees of freedom," *Electronics Letters*, vol. 52, no. 25, pp. 2068–2070, 2016.
[15] Y. Iizuka and K. Ichige, "Extension of two-level nested array with larger aperture and more degrees of freedom," *International Symposium on Antennas and Propagation*, vol. 32, pp. 442-443, 2017.
[16] J. Liu, Y. Zhang, Y. Lu, S. Ren, and S. Cao, "Augmented nested arrays with enhanced DOF and reduced mutual coupling," *IEEE Transactions on Signal Processing*, vol. 65, no. 21, pp. 5549–5563, 2017.
[17] H. Huang, B. Liao, X. Wang, X. Guo, and J. Huang, "A new nested array configuration with increased degrees of freedom," *IEEE Access*, vol. 6, pp. 1490–1497, 2018.
[18] Y. Huang, G. Liao, J. Li, J. Li, and H. Wang, "Sum and difference coarray based MIMO radar array optimization with its application for DOA estimation," *Multidimensional Systems and Signal Processing*, vol. 28, no. 4, pp. 1183–1202, 2017.
[19] C. Chen and P. P. Vaidyanathan, "Minimum redundancy MIMO radars," *Proceedings of the IEEE International Symposium on Circuits Systems (ISCAS)*, vol. 34, pp. 45–48, 2008.
[20] J. Li, D. Jiang, and X. Zhang, "DOA estimation based on combined unitary ESPRIT for coprime MIMO radar," *IEEE Communications Letters*, vol. 21, no. 1, pp. 96–99, 2017.
[21] E. Boudaher, F. Ahmad, and M. G. Amin, "Sparsity-based direction finding of coherent and uncorrelated targets using active nonuniform arrays," *IEEE Signal Processing Letters*, vol. 22, no. 10, pp. 1628–1632, 2015.
[22] J. Shi, G. Hu, X. F. Sun, W. Zheng, and Y. Xiao, "Generalized Co-prime MIMO radar for DOA estimation with enhanced degrees of freedom," *IEEE Sensors Journal*, vol. 18, no. 3, pp. 1203–1212, 2018.
[23] R. Zhang, "Multiple emitter location and signal parameter estimation," *IEEE Transactions on Antennas and Propagation*, vol. 34, no. 3, pp. 276–280, 1986.
[24] R. Roy and T. Kailath, "ESPRIT-estimation of signal parameters via rotational invariance techniques," *IEEE Transactions on Acoustics, Speech, and Signal Processing*, vol. 37, no. 7, pp. 984–995, 1989.
[25] S. Qin, Y. D. Zhang, and M. G. Amin, "DOA estimation of mixed coherent and uncorrelated signals exploiting a nested MIMO radar," *Proceedings of the of IEEE Benjamin Franklin Symposium on Microwave and Antenna Sub-systems for Radar*, vol. 81, 2016.
[26] G. Zheng and J. Tang, "DOD and DOA estimation in bistatic MIMO radar for nested and coprime array with closed-form DOF," *International Journal of Electronics*, vol. 104, no. 5, pp. 885–897, 2016.
[27] M. Yang, L. Sun, X. Yuan, and B. Chen, "A new nested MIMO array with increased degrees of freedom and hole-free difference coarray," *IEEE Signal Processing Letters*, vol. 25, no. 1, pp. 40–44, 2018.
[28] W. Zheng, X. Zhang, and J. Shi, "Sparse extension array geometry for DOA estimation with nested MIMO radar," *IEEE Access*, vol. 5, pp. 9580–9586, 2017.
[29] W. He, X. Yang, and Y. D. Wang, "A high-resolution and low-complexity DOA estimation method with unfolded coprime linear arrays," *Sensors*, vol. 20, no. 1, pp. 218, 2020.
[30] C. H. Zhan, G. P. Hu, Z. X. Zhang et al., "Increasing utilization of redundant virtual array for DOA estimation based on coprime array," *Mathematical Problems in Engineering*, vol. 12, 2020.